Chem

CellPress

Article

# Engineering couplings for exciton transport using synthetic DNA scaffolds

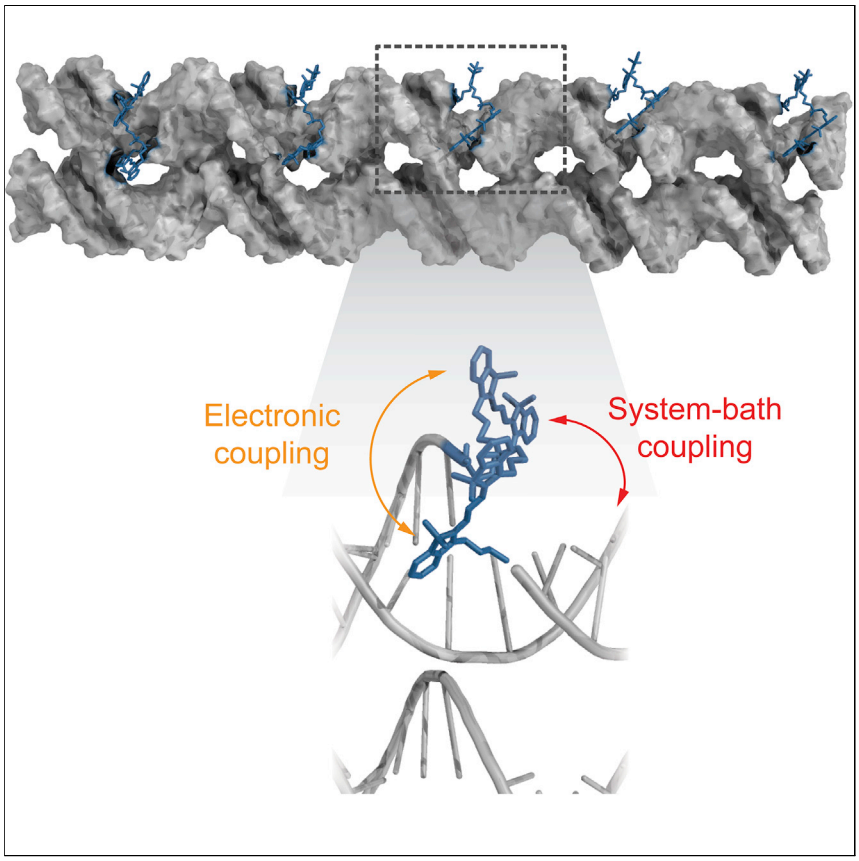


Excitonic systems in the condensed phase are controlled by electrodynamic couplings between the chromophores and between the chromophores and the surrounding environment. Here, we develop a DNA-based platform for excitonic systems with tunable couplings that we characterize using ultrafast multidimensional spectroscopy, single-molecule spectroscopy, and molecular dynamics simulations. Leveraging the tunability of this platform, we explore the role of the electrodynamic couplings in exciton transport.

Stephanie M. Hart, Wei Jia Chen, James L. Banal, ..., Robert Häner, Mark Bathe, Gabriela S. Schlau-Cohen

gssc@mit.edu

HIGHLIGHTS

Developed a tunable chromophore-DNA platform for coupled molecular excitons

Demonstrated control over both electronic coupling and system-bath coupling

Enhanced the efficiency of energy transfer using the DNA scaffold

Hart et al., Chem 7, 752–773
March 11, 2021 © 2020 Elsevier Inc.
https://doi.org/10.1016/j.chempr.2020.12.020

CellPress

Chem

Article

# Engineering couplings for exciton transport using synthetic DNA scaffolds

Stephanie M. Hart,[1,5] Wei Jia Chen,[1,5] James L. Banal,[2,5] William P. Bricker,[2,4] Amro Dodin,[2] Larysa Markova,[3] Yuliia Vyborna,[3] Adam P. Willard,[1] Robert Häner,[3] Mark Bathe,[2] and Gabriela S. Schlau-Cohen[1,6,*]

## SUMMARY

**Control over excitons enables electronic energy to be harnessed and transported for light harvesting and molecular electronics. Such control requires nanoscale precision over the molecular components. Natural light-harvesting systems achieve this precision through sophisticated protein machinery, which is challenging to replicate synthetically. Here, we introduce a DNA-based platform that spatially organizes cyanine chromophores to construct tunable excitonic systems. We synthesized DNA-chromophore nanostructures and characterized them with ensemble ultrafast and single-molecule spectroscopy and structure-based modeling. This synthetic approach facilitated independent control over the coupling among the chromophores and between the chromophores and the environment. We demonstrated that the coupling between the chromophores and the environment could enhance exciton transport efficiency, highlighting the key role of the environment in driving exciton dynamics. Control over excitons, as reported here, offers a path toward the development of designer nanophotonic devices.**

## INTRODUCTION

The ability of natural systems to harness and control the flow of electronic energy is essential for nearly all life on Earth.[1–4] Photosynthetic light-harvesting systems have evolved specifically to exert this control using networks of electronically coupled chromophores positioned with nanoscale precision.[5–10] The organization of these chromophore networks effectively guides the dynamics of excitons, i.e., bound electron-hole pairs created upon optical excitation. Measurements of excitons within these networks have revealed complex dynamical properties that are not captured by simple models,[11] which has led to active debates about the fundamental mechanism of exciton transport.[9,12–19] Understanding these mechanisms has been challenging because they depend on the interplay of multiple electrodynamic couplings, which are not easily disentangled. This limited understanding has, in turn, limited the design of molecular systems for energy harvesting, transport, and quantum information processing.

The photosynthetic light-harvesting machinery achieves nanoscale precision over chromophore positioning via the structure of protein assemblies. The chromophores are embedded within proteins at specific distances and relative orientations, which determine the electrodynamic couplings both among the chromophores (electronic coupling) and also between the chromophores and their surrounding environment

## The bigger picture

Excitons are the molecular scale currency of electronic energy. Control over excitons and their dynamics enables energy to be harnessed and directed for applications such as light harvesting and molecular electronics. The properties of the excitonic systems depend on intermolecular electrodynamic interactions within the material. In natural light harvesting these interactions are controlled through the precision of protein machinery, which is challenging to replicate synthetically. In this work, we design, build, and characterize synthetic excitonic systems composed of multiple chromophores scaffolded within DNA. By leveraging the nanoscale structural precision of DNA, we control multiple intermolecular interactions and demonstrate the ability of these interactions to enhance the efficiency of exciton transport.

(system-bath coupling). The properties of these couplings, including the strength and topology of the electronic coupling network and the relative magnitude of the system-bath coupling, determine the dynamics of the excitons. Subtle variations in chromophore positioning can dramatically alter how excitons evolve, for example, by changing their tendency to delocalize or shifting the balance between coherent and incoherent modes of transport. Precise nanoscale control over the molecular architecture is required to enable systematic examination of electronic and system-bath couplings and, therefore, of exciton dynamics.

Nanoscale control over chromophore position is challenging in proteins due to their structural complexity and limitations in mutagenesis.[20–22] Instead, synthetic model systems that position chromophores have been developed, including metal-organic frameworks,[8,23] viral proteins,[24–26] self-assembled molecular aggregates,[27–30] and conjugated polymers.[31] However, these systems lack a synthetic handle for electronic coupling. Covalently linked, small-molecule dimers are more tractable alternatives through which electronic coupling has been systematically varied.[32,33] In the regime of strong electronic coupling, however, the influence of nuclear motion has been more challenging to vary, and thus system-bath coupling has only been studied to a limited extent.[34,35] Furthermore, small-molecule dimers have a fixed spatial relationship due to the rigid organic linkers that connect them, limiting the ability to control the number of chromophores and to integrate these systems to form higher-order excitonic assemblies.

DNA-templated chromophores have recently emerged as designer materials that support coupled chromophores with programmable excitonic states and spatial organization that can be integrated into complex structures.[36–46] The high fidelity of base pairing ensures that a given DNA design will form predictable nanoscale architectures, and sequence-specific conjugation of chromophores allows for precise positioning within the structure.[40–43,47–50] DNA-based approaches have been extensively used to produce and characterize chromophore dimers. The electronic structure of these dimers has been well established,[38,39,51] and even used to investigate the properties of the DNA itself.[37,52] They have also been used as a tool to investigate electronic coherence[53] and vibronic coherence and its role in the dynamics of excitons within the dimer.[54] While insightful, these studies were limited to single dimers. More recently, a self-assembled chromophore-DNA platform with longer aggregates was developed and used to build higher-order structures, which enabled the investigation of long-distance exciton transport.[42,43] However, in this platform, the chromophores were not covalently bound and so lacked discrete control over the aggregate length. Furthermore, none of the previous approaches investigated system-bath coupling and its role in exciton transport.

Here, we report the development of chromophore-DNA constructs with control over both electronic coupling and system-bath coupling. We synthesized DNA strands with covalently attached, sequential indocarbocyanine Cy3 chromophores that we used to fabricate DNA duplexes and higher-order structures with chromophores positioned at desired spatial locations. We characterized the chromophore-DNA constructs with two-dimensional (2D) electronic spectroscopy, single-molecule spectroscopy, and computational modeling. With these constructs, we demonstrated both systematic variation in electronic coupling and aggregate lengths and also scaffold-dependent system-bath coupling. Upon increasing the rigidity of the DNA scaffold, the efficiency of energy transfer to an acceptor chromophore decreased, experimentally demonstrating the way in which the bath can tune the steps underlying long-distance exciton transport. The ability of our chromophore-

[1]Department of Chemistry, Massachusetts Institute of Technology, Cambridge, MA 02139, USA

[2]Department of Biological Engineering, Massachusetts Institute of Technology, Cambridge, MA 02139, USA

[3]Department of Chemistry and Biochemistry, University of Bern, 3012 Bern, Switzerland

[4]Department of Chemical and Biological Engineering, University of New Mexico, Albuquerque, NM 87131, USA

[5]These authors contributed equally

[6]Lead contact

*Correspondence: gssc@mit.edu

https://doi.org/10.1016/j.chempr.2020.12.020

DNA constructs to simultaneously yet independently change electronic coupling and system-bath coupling offers a platform for the design of excitonic systems. These bespoke excitonic systems and their integration into higher-order DNA nanostructures lay the groundwork for an emerging material with applications ranging from artificial photosynthesis to quantum sensing and computing.

## RESULTS AND DISCUSSION

### Controlling exciton formation in DNA scaffolds

Excitons supported by chromophore monomers, dimers, or trimers are positioned at desired spatial locations within the DNA scaffold. We inserted one, two, or three consecutive Cy3 units into the same single-stranded DNA (ssDNA) backbone using solid-phase phosphoramidite chemistry and then hybridized the modified strands with complementary single-stranded canonical DNA (Figure 1A). In previous DNA-based excitonic systems, chromophore dimers were formed upon annealing of the DNA strands.[36–38,55] Our synthetic approach of inserting chromophore aggregates into single strands offers three major advantages over other chromophore-DNA systems. First, the aggregate length can be extended beyond dimers in a discrete and controllable fashion, as illustrated here for trimers. Second, the aggregate, or even multiple aggregates, can be modularly positioned within both DNA duplexes and higher-order DNA nanostructures without additional chemical modifications on the complementary strands. It is this ability that enables these constructs to support long-distance exciton transport. Third, there is no monomer contamination due to unannealed ssDNA, which can be present at up to 10% in previous DNA-based excitonic systems.[54] For initial characterization, we focus on chromophore aggregates within duplexes (Table S1).

The steady-state absorbance spectra of the chromophore-DNA constructs indicate the formation of aggregates (Figure 1B). The linear absorption spectrum of the monomer features a peak at 18,150 $cm^{-1}$ and a pronounced vibronic progression from the strong coupling between the $S_0 \rightarrow S_1$ electronic transition and a C–C stretching mode.[56] The linear absorption spectra of the dimer and trimer show markedly different spectral features from the monomer, including a hypsochromic shift of the 0–0 vibronic peak from 18,150 $cm^{-1}$ for the monomer to 18,350 $cm^{-1}$ for the dimer and the trimer. The hypsochromic shift is consistent with strong electronic coupling between chromophores stacked co-facially, a so-called H-like organization.[57] The oscillator strength also redistributes from the 0–0 vibronic band to higher energy vibronic sidebands, namely 0–1 and 0–2. Finally, the trimer featured a further reduction in the overall oscillator strength of the 0–0 vibronic band and 0–1 vibronic band. Further spectral analysis is shown in Section S1.4. The linear absorption spectra were simulated using a vibronic exciton model (Sections S6.6 and S6.7). In order to reproduce the experimentally measured spectra, a multi-state model was required for the dimer and trimer constructs, suggesting heterogeneity in the aggregate structures (Sections S5.1, S5.4, and S6.7).

Fluorescence quantum yields and excited-state lifetimes are known to differ for chromophore aggregates compared to the monomer, providing additional photophysical quantities to establish aggregate formation.[57] The fluorescence quantum yield of the Cy3-DNA duplex constructs decreased with an increasing number of Cy3 subunits starting from 24% $\pm$ 1.6% (mean $\pm$ SD, n = 3) for the monomer to 8.9% $\pm$ 0.3% for the dimer and 3.4% $\pm$ 0.2% for the trimer. The average fluorescence lifetime of the Cy3-DNA constructs decreased with aggregate length on the DNA, starting from 1.15 $\pm$ 0.21 ns for the monomer to 0.72 $\pm$ 0.04 ns and 0.67 $\pm$ 0.01 ns for the dimer

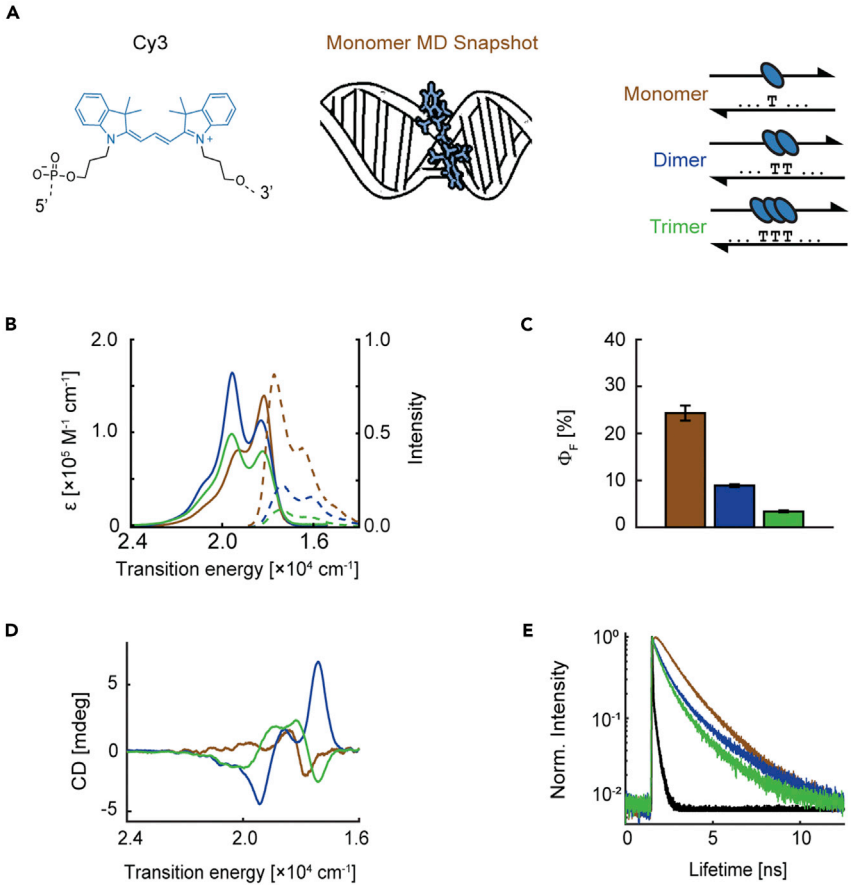


**Figure 1. A chemical approach to form Cy3 aggregate constructs using DNA scaffolds**

(A) Cy3 (left) is covalently linked to 3′ and 5′ ends of the deoxyribose-phosphate backbone of single-stranded DNA (ssDNA). Cy3-modified DNA nanostructures are formed by hybridizing Cy3-modified ssDNA with canonical complementary ssDNA strands, as shown in a molecular dynamics snapshot of a Cy3 monomer attached to a DNA duplex (center) and in the schematic (right, top) where blue ovals denote Cy3. Cy3 dimers and trimers are formed by linking consecutive Cy3 chromophores into ssDNA and hybridizing with complementary strands (right, middle, and bottom).

(B) Absorbance (solid lines) and quantum yield-normalized fluorescence spectra (dashed lines) of Cy3 monomer (brown), dimer (blue), and trimer (green). [DNA duplex] = 0.5 μM in 40 mM Tris, 20 mM acetate, 2 mM ethylenediaminetetracarboxylic acid (EDTA), and 12 mM $MgCl_2$ (TAE-$MgCl_2$ buffer).

(C) Fluorescence quantum yields ($\Phi_F$) of Cy3 monomer, dimer, and trimer in duplexes. [DNA duplex] = 0.5 μM in 1 × TAE-$MgCl_2$ buffer. Error bars are standard deviations of three independent replicate measurements.

(D) Circular dichroism (CD) spectra of Cy3 monomers, dimers, and trimers.

(E) Fluorescence decay traces of Cy3 monomers, dimers, and trimers. The instrument response function is shown in black.

and trimer, respectively (Section S1.5; Table S3). The decrease in fluorescence lifetimes of the Cy3-DNA duplex constructs may be due to enhanced internal conversion rates, which leads to a decrease in quantum yield. An enhancement of internal conversion rates as the aggregate length increases has been observed in other molecular systems.[58–60]

The fluorescence lifetime data exhibited multi-exponential decay kinetics, which generally reflects heterogeneity due to subpopulations within a measured

ensemble. The fluorescence lifetime data of the monomeric Cy3-DNA duplex constructs required a bi-exponential function, whereas those of the dimeric and trimeric Cy3-DNA duplex constructs required tri-exponential functions for an adequate fit, which further suggest heterogeneity in the electronic structure regardless of aggregate length (Table S3; Figure 1E). The existence of heterogeneity was supported by all-atom molecular dynamics (MD) simulations of the monomer (Figure S30). Specifically, the simulations show that the Cy3 monomer can be bound or unbound from the DNA duplex, which leads to a heterogeneous environment for the chromophore.[61] The simulations of the dimer and trimer revealed co-facial stacking, which is also referred to as an H-like aggregate structure (Sections S5.1 and S5.4; Figures S31 and S32). Similar to the case of the monomer, these simulations revealed two major structural states, a weakly coupled, monomer-like state and a strongly coupled dimer state, which lead to localized and delocalized excited-state wavefunctions, respectively.

### Controlling electronic coupling within Cy3 dimers in DNA duplexes

We systematically vary the electronic coupling within the Cy3 dimer constructs by changing the distance and relative orientation between the two chromophores (Figure 2A; Section S1.7; Table S7). We inserted one to three nucleotide spacers between the Cy3, where each nucleotide spacer introduces a spatial distance of ~0.34 nm and a ~36° twist angle, as shown in snapshots from MD simulations (Figure 2A).[62] The decrease in electronic coupling with the number of inserted nucleotide spacers between the Cy3 dimers is reflected in the steady-state linear absorbance spectra. The hypsochromic shift (190 $cm^{-1}$), consistent with a coupled dimer in an H-like configuration, is observed across the series. As discussed above, the dimer without nucleotide spacers shows a dramatic redistribution of oscillator strength from the 0–0 to the 0–1 band, which is another signature of H-like dimer formation. The redistribution of oscillator strength decreases as the number of nucleotide spacers increases, reflecting the loss of electronic coupling within the dimer due to the increase in intramolecular spacing and changing transition dipole angle (Figure S45). When the Cy3 dimers were separated by three nucleotide spacers, the oscillator strength of the 0–0 band was recovered near the level of the Cy3 monomer. Further, both the fluorescence quantum yield (Figure 2C) and fluorescence lifetime approached the monomer values as the number of nucleotide spacers increased (Figure S10). The spectra of the dimers with varied nucleotide spacing can be reproduced using a multi-configurational model based on all-atom MD simulations (Figures S46–S50). The multi-state configurations identified include strongly coupled, H-like dimers for zero and one nucleotide spacings, while both slip-stacked (known as J-like) and H-like dimers were observed for two nucleotide spacings.[57] Subpopulations of weakly coupled, monomer-like dimers were also observed for these nucleotide spacings (Figure S45). Only monomer-like dimers were observed for three nucleotide spacings. The configurational variation shows that, along with control over the magnitude of electronic coupling, these Cy3-DNA constructs offer the ability to select the nature of the aggregate formed.

To experimentally characterize the intra-dimer electronic coupling, we use 2D electronic spectroscopy. 2D electronic spectroscopy measures the excitation frequency-emission frequency correlation and so the signal intensity at the frequencies of two excitonic states increases with the electronic coupling between them.[63–67] As shown in Figure 2B, the relative coupling between constituent monomer units appears as a cross peak at excitation frequency $\omega_{ex}$ = 18,100 $cm^{-1}$ and emission frequency $\omega_{em}$ = 19,500 $cm^{-1}$, which are the energies of the two excitonic states with the most oscillator strength within the dimer. As shown in Figure 2E, we extracted the upper cross

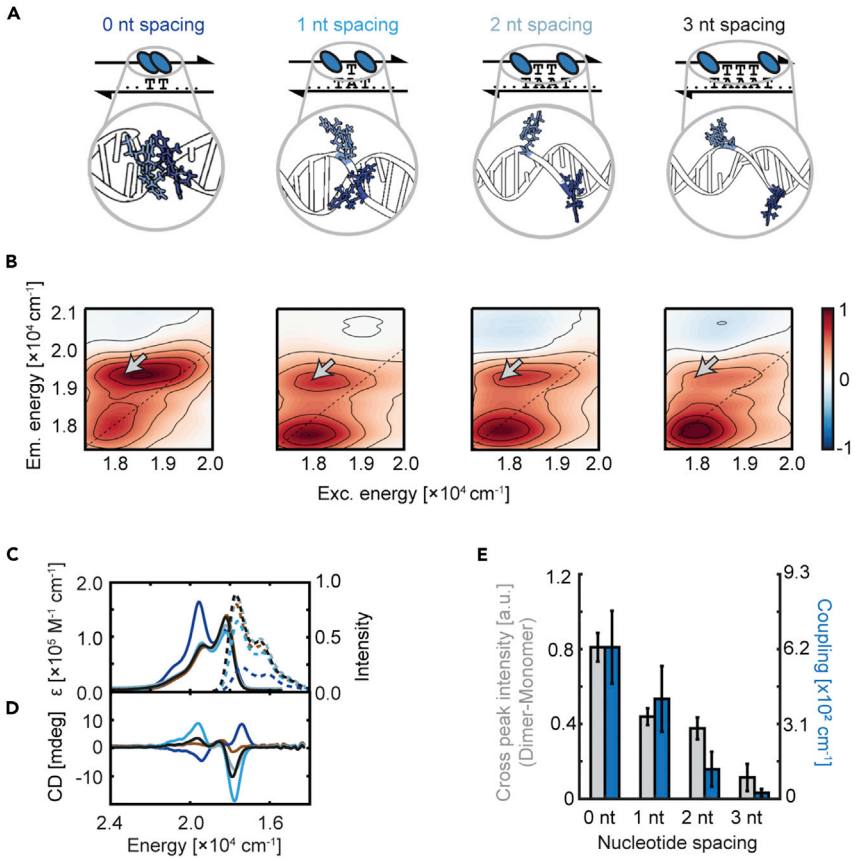


**Figure 2. Engineering electronic coupling within Cy3 dimers in DNA**

(A) The insertion of spacer nucleotides (nt) within dimers increases the distance and changes the relative orientations of the Cy3 (blue ovals).

(B) Representative two-dimensional spectra (250-fs time delay) of each Cy3 dimer for the nt spacing shown above in (A).

(C) Absorbance spectra (solid lines) and quantum yield-normalized fluorescence spectra (dashed lines) of Cy3 dimers with varied nt spacings between each Cy3 molecule on the DNA duplex. Absorbance and emission spectra of monomeric Cy3 in the DNA duplex are re-plotted for comparison (brown). [DNA duplex] = 0.5 μM in 1 × TAE-$MgCl_2$ buffer.

(D) Circular dichroism spectra of nucleotide-spaced dimers (monomer spectrum is also shown in brown).

(E) Comparison of relative upper diagonal cross peak intensity (marked in B with a gray arrow, scaled by the diagonal peak for the 0-0 transition) from two-dimensional spectra and electronic coupling estimated using transition density cube calculations on molecular dynamics structures. Error bars for cross peak intensity are standard deviations of three independent replicate measurements. Error bars for electronic couplings are calculated from Cy3 dimer configurations on DNA duplexes simulated using MD.

peak intensity to compare the relative coupling between the dimers without contamination from population dynamics or excited-state absorption, which contributes to the spectral features at the lower cross peak (further details are given in Section S2.2).[67,68] We computed the magnitudes of the electronic coupling using transition density cube calculations (Sections S5.4 and S6.7). The scaling of the experimental and computational results are in good agreement, including strong coupling within the zero-nucleotide-spaced dimers, and progressively weaker coupling for the 1–3-nucleotide-spaced dimers. However, an underestimation of the relative couplings for the weakly coupled dimers is observed, consistent with the minor discrepancies between the experimental and simulated absorption spectra (Section S5.4), and may

be due to variation in the vibronic coupling for different DNA constructs. Overall, the qualitative agreement highlights that our approach includes computational prediction for the design of electronically coupled constructs.

## Dependence of ultrafast exciton-bath coupling on DNA scaffold

Synthetic DNA enables the facile integration of chromophores into a variety of DNA scaffolds.[69–75] Because of our synthetic strategy, Cy3 chromophores can be readily incorporated into a wide range of nanostructures using the same Cy3-modified ssDNA strands, which permits the investigation of scaffold-dependent properties such as system-bath coupling. The double-crossover (DX) tile motif is an essential building block for DNA nanotechnology. DX tiles are at least twice as rigid as duplexes due to inter-duplex crosslinking that couples bending, twisting, and stretching modes.[76,77] To investigate scaffold-dependent behavior, we first compared the ultrafast system-bath coupling of free Cy3, Cy3 monomer in duplexes, and Cy3 monomer in DX tiles (sequences shown in Section S2.3).

System-bath coupling gives rise to fluctuations in the frequency of a transition, also known as spectral diffusion, on a range of timescales. The frequency-frequency correlation function describes the timescale of the fluctuations. On the ultrafast timescale, the overall decay in the correlation function arises from dephasing due to coupling of the electronic transition to a near-continuum set of modes in the bath, known as overdamped modes. The oscillations in the correlation function arise from coupling to underdamped modes in the bath, generally normal modes of the chromophore. Because 2D spectroscopy probes the excitation frequency-emission frequency correlation, the frequency-frequency correlation function is contained in the temporal dynamics of the spectra. The temporal dynamics are measured by recording a series of 2D spectra as a function of a delay time between excitation and emission events. The frequency-frequency correlation for a given electronic transition is proportional to the center-line slope of its peak in the 2D spectra (Figure 3B).[78–81] The center-line slope for the series of delay times is used to construct the frequency-frequency correlation function.

We compare the dynamics of the frequency-frequency correlation for the lowest energy transition, the 0–0 band, for monomeric Cy3 under all three scaffold conditions (Figure 3C). The correlation function decays rapidly for all samples with average timescales of 290±40 fs, 120±40 fs, and 100±40 fs for the free chromophore, the duplex, and the DX tile, respectively (bi-exponential fit parameters are shown in Section S2.5). The femtosecond decay constant is due to fast spectral diffusion, similar to previously studied chromophores in solution.[82,83] The correlation function oscillates for up to 200 fs for all samples, reflecting the presence of a strongly coupled underdamped vibrational mode. The Fourier transform of the decay-subtracted correlation function for delay times 50–200 fs is shown in Figure 3D. The frequency-domain data have a broad peak centered at 450 $cm^{-1}$, which suggests coupling to approximately the same underdamped modes regardless of the scaffold. In addition, homodyne transient grating measurements show coupling to approximately the same modes through the presence of a peak at the same frequency (Figure S17A).[84] As illustrated in Figure S17B, the broad peak observed in Figure 3D is consistent with rapid dephasing of normal mode vibrations delocalized over Cy3 from 250–750 $cm^{-1}$. The free Cy3 in solution showed larger amplitude oscillations than the DNA-bound Cy3 (Section S2.5). This indicates that covalent attachment to DNA reduces the degree to which the electronic transition dipole couples to the underdamped bath mode or modes. The short timescale decays and amplitude oscillations observed for both the duplex and DX tile reflect their

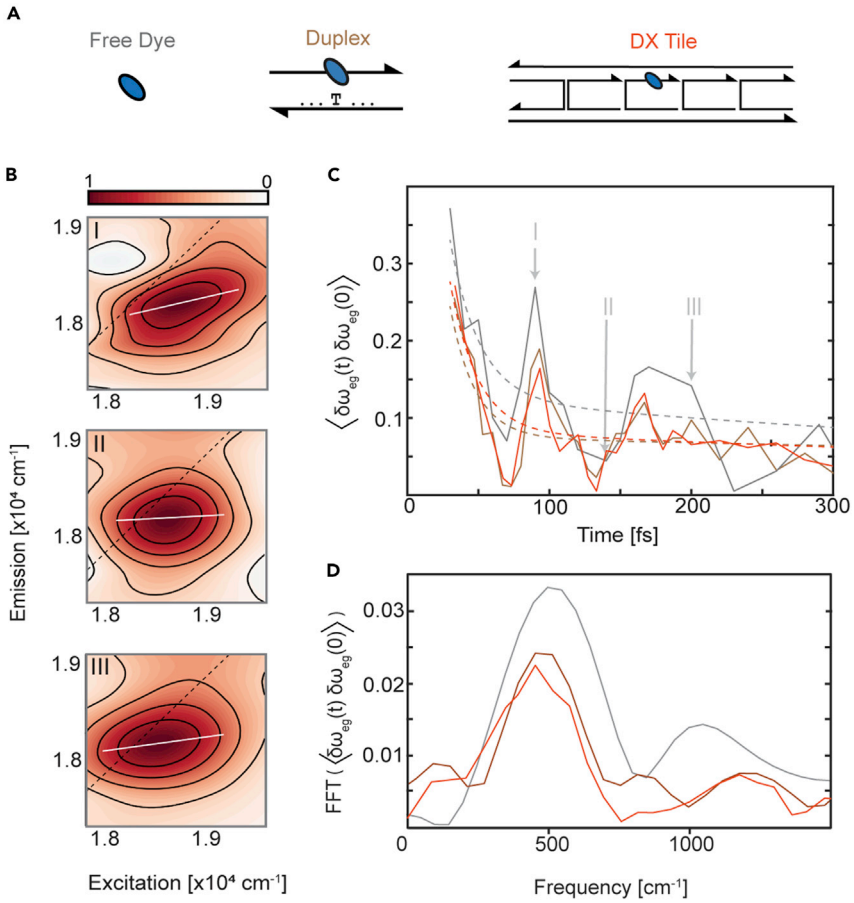


**Figure 3. Ultrafast system-bath coupling for monomeric Cy3**

(A) Schematic of Cy3 (blue oval) as a free chromophore, in a duplex, and in a DX tile.

(B) Selected 2D spectra of the free chromophore at varying waiting times (I, II, and III indicated in C) with center-line slope (CLS) of the 0–0 transition shown in white.

(C) Frequency-frequency correlation function derived from the CLS (solid lines) for Cy3 as a free chromophore (gray), in a duplex (brown), and in a DX tile (red) with fit of exponential decay (dotted lines).

(D) The power spectrum of frequency-frequency correlation function (50–200 fs) for all three samples. All samples were measured in 1 × TAE-$MgCl_2$.

similar local environments on the nanometer length scale, as opposed to the variation in persistence length on the tens of nanometers scale.[77–79] The faster decorrelation may arise due to the charge intrinsic to DNA, including the negatively charged backbone and associated counter ions, which is constant across the varying constructs and could cause even faster charge redistribution upon photoexcitation of the positively charged dye, thus driving rapid fluctuations in the transition energy.

## Impact of DNA scaffold on heterogeneity

Heterogeneity between individual Cy3-DNA constructs, also known as a static disorder, arises from the coupling of slow, anharmonic motions of the DNA scaffold to the electronic transitions. This long timescale system-bath coupling gives rise to differences in the transition frequency and other photophysical parameters of the constructs. To initially investigate the impact of the DNA scaffold on heterogeneity between constructs, the fluorescence lifetimes of Cy3 in duplexes and in DX tiles were compared, as the components of a multi-exponential lifetime decay generally correspond to subpopulations, as discussed above. At the ensemble level, the

measured fluorescence lifetimes were similar for Cy3 in the two scaffolds. Fits to the fluorescence lifetime required a bi-exponential decay for monomers and a tri-exponential decay for dimers and trimers, reflecting at least two and at least three subpopulations, respectively (Section S1.5).

To further investigate heterogeneity between Cy3-DNA constructs, the fluorescence lifetimes of individual constructs were measured using single-molecule fluorescence spectroscopy. Single-molecule measurements were performed on monomeric and dimeric Cy3 in duplexes and Cy3 in DX tiles. Each construct required a bi-exponential decay function for a good fit, indicating the presence of at least two subpopulations in each construct that interconvert on a timescale longer than the nanosecond lifetime but shorter than the tens of milliseconds required to detect sufficient emission to construct a decay curve (Section S4). The shortest component from the ensemble dimer decay was unobserved, likely because it was hidden in the longer instrument response function of the single-molecule apparatus.

To characterize the overall heterogeneity, the average lifetimes of each construct were histogrammed to build a distribution for each sample (Figures 4B and 4C). The average lifetime encompasses the timescales of the subpopulations and their relative weight within single constructs. The distributions of average lifetimes benchmark the heterogeneity of photophysical properties through their widths. All of the distributions showed one primary peak, although the widths varied, indicating different levels of heterogeneity. For Cy3 monomers, the full-width half-maximum in a duplex (0.90 ns) is more than four times broader than the full-width half-maximum in a DX tile (0.20 ns). Consistently, for Cy3 dimers, the full-width half-maximum in a duplex (0.60 ns) is broader than in a DX tile (0.30). These differences in heterogeneity arise from differences in the system-bath coupling due to the properties of the DNA scaffold. The scaffold design is, therefore, a tool to control the system-bath coupling and thereby tune the heterogeneity of the excitons themselves.

To investigate the structural differences responsible for the lifetime differences between the two scaffolds, MD simulations were performed for monomeric and dimeric Cy3 in duplexes and in DX tiles. Solvent accessible surface area (SASA) of Cy3 in each construct was extracted from the simulation data (Figures 4D and 4E). The SASA distributions are broader for both monomeric and dimeric Cy3 in duplexes compared to the DX tile counterparts. The SASA distribution for monomeric Cy3 in duplexes is bimodal, showing two populations centered at 460 and 500 $Å^2$, whereas the distribution for monomeric Cy3 in DX tiles is unimodal and narrow, centered at 510 $Å^2$. Similarly, the SASA distribution of dimeric Cy3 in duplexes is bimodal, with populations centered at 440 and 520 $Å^2$, whereas the distribution for dimer Cy3 in DX tiles is unimodal, centered at 520 $Å^2$. The differences in width and modality likely originate from the differences in rigidity between the two scaffolds (Figure S42). The DX tile rigidity restricts kinking of the structure whereas the duplex flexibility allows kinking (bending), leading to conformations in which the chromophore is embedded in the DNA groove, where the SASA is low.[77,85] The lifetime of Cy3 has been shown to depend strongly on the solvent environment, which affects the rates of excited-state processes such as internal conversion pathways and photoinduced isomerization.[39,86] Therefore, the broader SASA distribution is likely the cause of the broader distribution of lifetimes for the duplex-scaffolded monomer and dimer as compared to the DX-scaffolded chromophores.

While system-bath coupling is often studied in the limiting regimes of static disorder and ultrafast dynamics, fluctuations of the excitonic system occur on many timescales. Motions of the DNA scaffold also gives rise to structural fluctuations of the

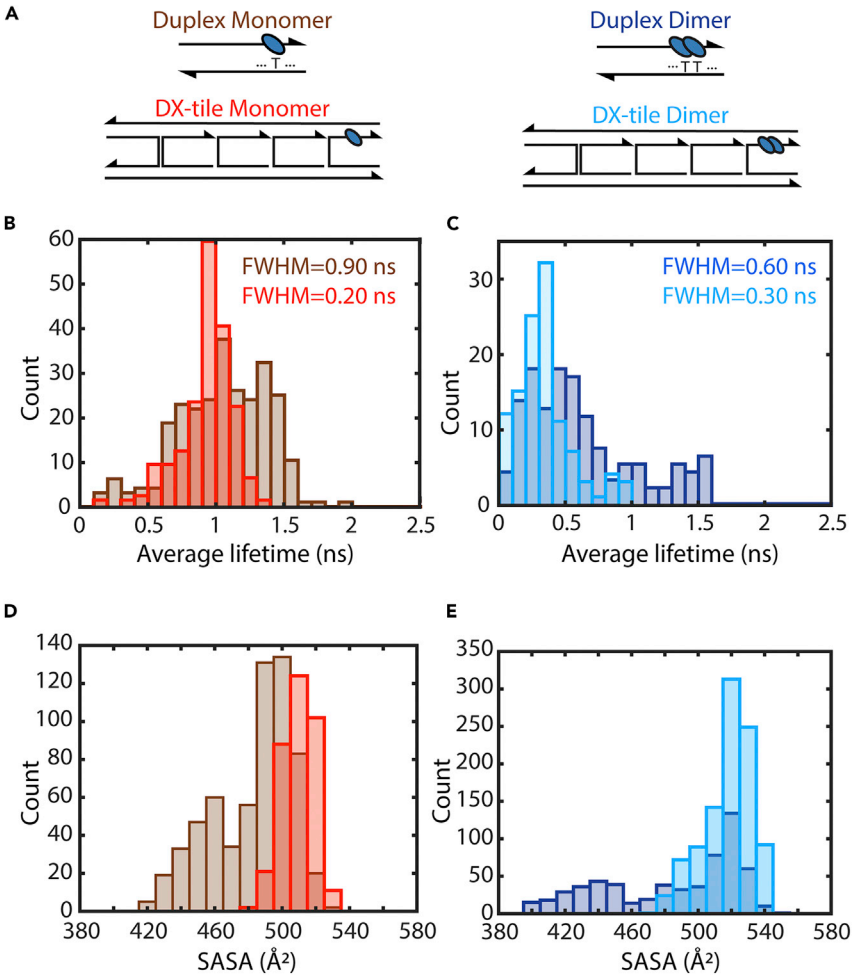


**Figure 4. Heterogeneity of Cy3 in DNA scaffolds**

(A) Schematics of monomeric (left) and dimeric (right) Cy3 in duplexes (top) and DX tiles (bottom).

(B) Histograms constructed from the average lifetimes of individual constructs for monomeric Cy3 in duplexes (brown) and in DX tiles (red) measured with single-molecule spectroscopy.

(C) Histograms constructed from the average lifetimes of individual constructs for dimeric Cy3 in duplexes (dark blue) and in DX tiles (bright blue) measured with single-molecule spectroscopy.

(D) Histograms constructed from the MD trajectory of solvent-exposed surface area (SASA) for monomeric Cy3 in duplexes (brown) and in DX tiles (red).

(E) Histograms of SASA for dimeric Cy3 in duplexes (dark blue) and in DX tiles (bright blue).

Cy3 chromophore on the timescale of energy transfer. For the Cy3 monomer, depolarization of the transition dipole moment is due to the motion of the chromophore and can be measured with ensemble time-resolved fluorescence anisotropy. The anisotropy is calculated from separately detected parallel and perpendicular components of the fluorescence emission and is shown in Figure 5A for monomeric Cy3 in duplexes and in DX tiles. The anisotropy decay curves were fit with a two time-scale model. The short-time constants for the monomer in duplexes and in DX tiles were $0.19 \pm 0.15$ ns and $0.62 \pm 0.14$ ns, respectively, while the long-time constants were $3.45 \pm 0.94$ ns and $22.97 \pm 16.22$ ns, respectively (Table S18). The long-time constant was assigned to the tumbling of the DNA construct, which is faster for the duplex due to its smaller size, and corresponding higher rotational diffusivity, relative to the DX tile. The short-time constant was assigned to local structural fluctuations of the chromophore. The amplitude of the short-time constant can be

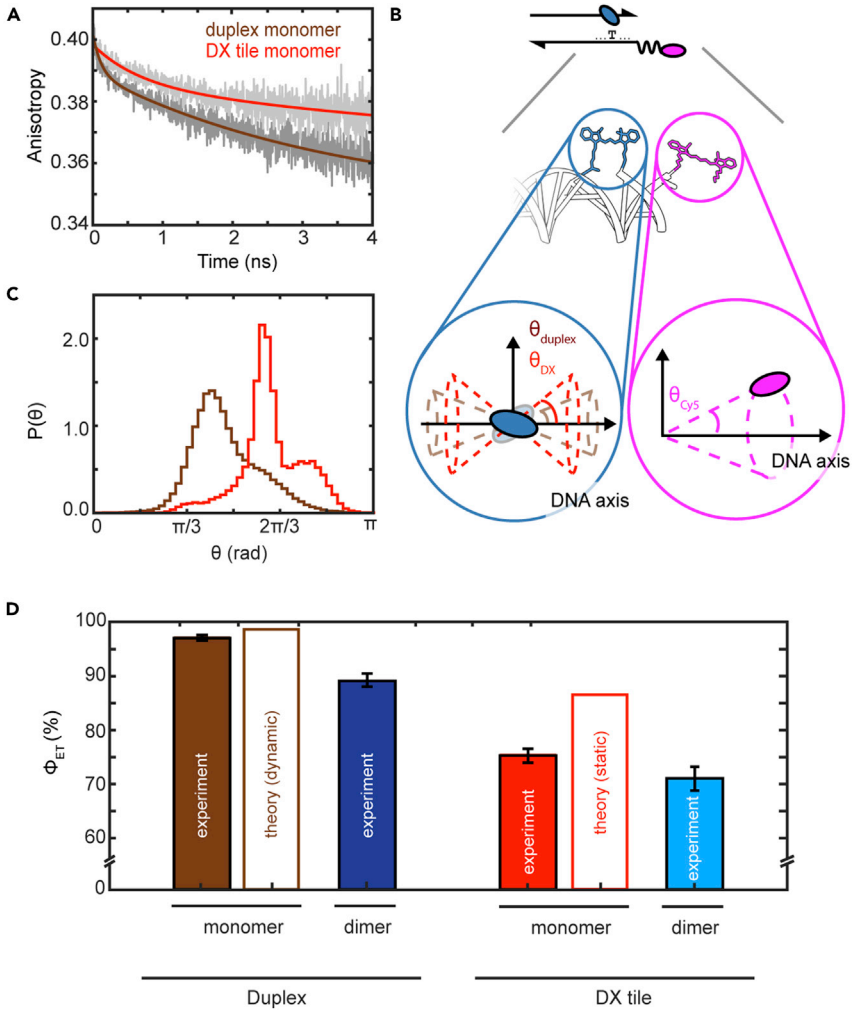


**Figure 5. Effect of DNA scaffold on energy transfer efficiency**

(A) Fluorescence anisotropy decay curves for monomeric Cy3 in duplexes (data, light gray; fit, brown) and DX tiles (data, dark gray; fit, red). Fit parameters are in Table S18.

(B) Schematic of monomeric Cy3 in DNA with acceptor (top). The cone angles extracted from the anisotropy decays and their expected orientation relative to the DNA axis are illustrated for Cy3 in duplexes and DX tiles (bottom left) and for Cy5 (right).

(C) The angle between the transition dipole moment of monomeric Cy3 in duplexes (brown) and DX tiles (red) with respect to the DNA backbone extracted from MD simulations.

(D) Energy-transfer efficiency from ensemble fluorescence experiments and from Monte-Carlo FRET theory. Error bars are standard deviations of three independent replicate measurements.

related to an order parameter from which a cone describing the extent of local fluctuations can be calculated.[87] Using this model, the difference in half-cone angle between Cy3 monomers in duplexes and in DX tiles is $\Delta\theta = 8.8 \pm 4.6^{\circ}$ (Section S3.5), where Cy3 monomers on DX tiles were found to have more local freedom than Cy3 monomers on duplexes. The increase in local freedom is likely due to the difference in kinking, as discussed above. In the MD simulations, the duplex kinks toward the Cy3 (Figure S39), confining the chromophore and restricting its motion.

## Dependence of energy-transfer efficiency on DNA scaffold

To investigate exciton transport with the Cy3-DNA constructs, we attached a Cy5 monomer with a deoxythymidine spacer to the terminal end of the DNA to serve

as an acceptor (Figure 5B). The efficiency of energy transfer from the Cy3 monomer or dimer to the Cy5 acceptor was quantified by ensemble steady-state fluorescence measurements (Figure 5D; Section S3.3). An energy-transfer efficiency of 95% was found for monomeric Cy3 in duplexes while the efficiency decreased to 90% for dimeric Cy3 in duplexes, which can be attributed to the reduced quantum yield of the dimer relative to the monomer (Figure 1C). In contrast, an efficiency of 75% was found for Cy3 monomers in DX tiles and of 70% for Cy3 dimers in DX tiles (Sections S3.1–S3.4). A 20% drop in energy-transfer efficiency was observed for Cy3 in DX tiles compared to in duplexes, even though the number of nucleotides between the donor and acceptor was maintained in both scaffolds.

To understand the molecular origin of the scaffold-dependent efficiency, we individually examine the photophysical quantities involved in energy transfer. The Cy3 monomer or dimer and the Cy5 are ~2.7 nm apart, and at this distance, energy transfer occurs through Förster resonance energy transfer (FRET). The efficiency of FRET depends on the quantum yield of the donor chromophore, the extinction coefficient of the acceptor, the transition energies of the chromophores, the distance between them, and the angle between their transition dipole moments.[88–92] The quantum yields, molar absorption coefficients, and transition energies are the same for both the duplexes and DX tiles (Figure S22). The distances are similar as the same local nucleotide sequence was used (Section S3.1) and the MD simulations show little scaffold-specific displacement of the chromophore (Section S5.2). Therefore, the angle between the transition dipole moments is the likely origin of the difference.

The FRET rate is sensitive to thermal fluctuations in the orientations of the transition dipole moments and thus the ensemble FRET efficiency depends on the angular distribution that these fluctuations generate.[93] Both the timescale of the fluctuations and the shape of the distribution can influence the overall energy-transfer efficiency. In the case where fluctuations are fast relative to energy-transfer time scales (dynamic limit), transition dipoles sample a large number of different configurations between energy-transfer events. In this limit, ensemble FRET efficiency is determined by a single mean energy-transfer rate, given by the average over the angular distribution. In contrast, when fluctuations are slow relative to energy-transfer timescales (static limit), transition dipoles sample very few configurations between energy-transfer events. In this limit, the distribution of rates becomes a distribution of efficiencies, the latter of which is averaged to determine the ensemble FRET efficiency.

The fluctuations in transition dipole orientation are often assumed to be normally distributed with a variance determined experimentally using fluorescence anisotropy. This assumption is valid in the dynamic limit because a normal distribution is sufficient to capture the average behavior. In the chromophore-DNA systems, the normal distribution is visualized as a cone centered along the transition dipole moment of the chromophore, which is at a position and orientation determined by the geometric constraints imposed by the linkers, as illustrated in Figure 5D (Section S3.5).[93,94] The cone angle of Cy5 is $\theta_{Cy5} = 33^\circ \pm 2^\circ$ centered on the axis parallel to the DNA backbone.[94] The cone angle of Cy3 is centered parallel to that of Cy5 and, as discussed above, is narrower for monomeric Cy3 in duplexes than in DX tiles. The efficiencies calculated with the normal distribution model are 98% and 97% for the duplex and DX tile, respectively (Table S19). While the efficiency for the duplex is close to the experimentally measured value, the efficiency for the DX tile is significantly over-estimated (Figure 5D). The anisotropy data revealed

that the fluctuations for Cy3 on duplexes are ~3–4 times faster than for Cy3 on DX tiles, suggesting that the dynamic limit may not be appropriate for the DX tile.

In the static limit, the shape of the angular distribution can have a significant effect on FRET efficiency, so the approximation of a normal distribution is not necessarily reliable. In fact, the efficiencies calculated in the static limit with the normal distribution model are nearly identical to those calculated in the dynamic limit, 98% and 97% for the duplex and DX tile, respectively. To evaluate the validity of the normal distribution, we extracted the distributions from the all-atom MD simulations of Cy3 on both scaffolds, which exhibit a structured profile with differences between the two constructs (Figure 5C). This structure arises due to the constraints of the two-point tether and steric interactions between Cy3 and the DNA scaffold that cause Cy3 to rotate out of alignment with the DNA backbone. For the DX tile distribution, the FRET efficiency is 86% in the static limit, which is closer to the experimental value than the normal model, and illustrates that the profile of the distribution can exert a significant influence on the overall energy-transfer efficiency in the static limit. For the duplex distribution, the FRET efficiency is 83% in the static limit, which underestimates the experimental value. The corresponding efficiency is 98% in the dynamic limit, consistent with the experimental value. These results suggest that the static limit is more appropriate for the DX tile whereas the dynamic limit is more appropriate for the duplex, as expected based on the timescales of the fluctuations from the anisotropy measurements, and that the difference in timescales is the source of the difference in the FRET efficiency.

While the effect of the average angle between the transition dipole moments is well known,[90,95,96] these results demonstrate that the nature and timescales of the fluctuations that shape the distribution of angles ultimately determine the measured FRET efficiencies. Although the efficiency is independent of the timescale for the commonly used normal model, some condensed phase systems can have a structured angular distribution that, in the static limit, restricts the overall FRET efficiency, as observed for the DX tile scaffold. The efficiency can be recovered, however, by rapid fluctuations in the dynamic limit, as observed for the duplex tile scaffold. This picture is in contrast to the typical view of fluctuations as a disruption to a process of interest and provides a mechanism to maintain high efficiency, which may even be playing a role in photosynthetic energy transfer where high quantum efficiency is observed despite the fluctuations of the protein environment.

Our measurements are an experimental demonstration that the properties of the DNA scaffold itself, i.e., the bath, impact the dynamics of excitonic systems, including transport. While the impact of the bath on exciton dynamics had been well established theoretically,[97–99] previous experiments were limited to the impact of the bath on individual excitonic states.[24] Chromophore-DNA constructs open the door to varying the system-bath coupling for chromophore aggregates, and thus achieving the full nanoscale control required to direct exciton dynamics.

## Conclusion

Here, we develop a DNA-based platform for synthetic control over excitonic systems. While the interplay of electronic coupling and system-bath coupling was known to guide exciton transport, previous approaches were unable to simultaneously vary both couplings. We show the importance of this ability by demonstrating bath-dependent energy-transfer efficiency. Characterization and manipulation of electronic coupling and system-bath coupling in individual duplexes and DX tiles, the building block of DNA origami, provides a path toward integration of our

excitonic system into higher-order objects,[71–75] which is not easily accessible with other synthetic methods.[38,39] The production of higher-order structures provides access to novel materials with prescribed properties and geometric structures for broad-ranging applications including light harvesting and information processing.

## EXPERIMENTAL PROCEDURES

### Resource availability

#### *Lead contact*

Further information and requests for resources should be directed to the lead contact, Gabriela S. Schlau-Cohen (gssc@mit.edu).

#### *Materials availability*

Reasonable requests for materials should be directed to the lead contact.

#### *Data and code availability*

Data and codes used in this work are available upon request from the lead contact.

### Synthesis procedure for Cy3-modified strands

Cy3-modified oligonucleotides (sequences are listed in Tables S1, S7, S9, and S13) were prepared via automated oligonucleotide synthesis on a 394-DNA/RNA synthesizer (Applied Biosystems) following previously published procedures.[50] UltraMild CE phosphoramidites, UltraMild supports, and special Cap Mix A (tetrahydrofuran/pyridine/phenoxyacetic anhydride) were used to synthesize the oligomers on support. Cyanine-3 phosphoramidite, UltraMild CE phosphoramidites, and other reagents for the synthesis of the oligonucleotides were purchased from Glen Research (Sterling, VA) or Sigma-Aldrich (Buchs, Switzerland). The coupling time for nucleotide-to-cyanine, cyanine-to-cyanine, and cyanine-to-nucleotide coupling steps was increased to 3 min. For all other nucleotide couplings, the standard coupling time (25 s) was used. Cleavage from the solid support and final deprotection involved treatment with 50 mM potassium carbonate solution in methanol at room temperature for 4 h. The oligonucleotides were purified by ion-pair reversed-phase high-performance liquid chromatography using a Shimadzu LC system equipped with a Shimadzu-block temperature controller (Section S1.2; Figures S1–S3).

### Preparation and purification of DNA constructs

Unmodified single-stranded DNA were obtained from Integrated DNA Technologies (Coralville, IA) and were received as dry pellets. All strands required to form either DNA duplexes or DX tiles were re-constituted into DNase/RNase-free water at 500 μM concentrations and kept at −20°C until further use. Equimolar concentrations (50 μM) of oligonucleotide strands required to form either duplexes or DX tiles were added into nuclease-free water. A volume of 10 × TAE-$MgCl_2$ buffer (400 mM Tris, 100 mM acetate, 20 mM EDTA, 120 mM $MgCl_2$) was added into the mixture to have a final concentration of 1 × TAE-$MgCl_2$ (40 mM Tris, 10 mM acetate, 2 mM EDTA, 12 mM $MgCl_2$). Buffer concentrations for samples used in all experiments were maintained at 1 × TAE-$MgCl_2$. For duplexes, the mixture was subjected to the following annealing protocol: 2 min at 95°C, 80°C–70°C at −2°C $min^{-1}$, 70°C–50°C at −1°C $min^{-1}$, 50°C–20°C at − 2°C $min^{-1}$. An extended annealing protocol was used for DX tiles: 2 min at 95°C, 80°C–70°C at − 1°C $min^{-1}$, 70°C–50°C at − 0.5°C $min^{-1}$, 50°C–20°C at − 1°C $min^{-1}$ (melting curves shown in Section S1.3, Figure S4). The annealed mixtures were then purified with native polyacylamide gel electrophoresis (PAGE) using a Biorad Mini-PROTEAN system that was equipped with 1.5-mm-spaced glass plates for gel casting and 10-well, 1.5-mm-thick well

combs. Annealed DNA duplex samples were loaded into 12% PAGE gels (400 pmole per well) that were supplemented with 1 × TAE-$MgCl_2$ buffer. Annealed DX tile samples were loaded into 10% PAGE gels (400 pmole per well) that were also supplemented with 1 × TAE-$MgCl_2$ buffer. Gels were ran at 100 V at constant voltage for 45 min at room temperature. After electrophoresis, the gels were examined through a Vernier BlueView Transilluminator (Beaverton, OR) and the bands of interest were excised. The excised gel pieces were coarsely chopped, collected into a 2.0-mL Eppendorf DNA LoBind microcentrifuge tubes, and 1 × TAE-$MgCl_2$ buffer was added until all the gel pieces were covered with buffer. The mixture was incubated for 14 h at 35°C, then vortexed for 10 s to re-disperse the gel pieces and transferred into several Biorad Freeze 'N Squeeze tubes, which were spun at $10,000 \times g$ for 1 min. The supernatant from each tube was collected and concentrated to 50 μL using either a 3,000 or 30,000 Amicon molecular-weight-cutoff microcentrifuge filters (Millipore Sigma; Allentown, PA) for duplexes and DX tiles, respectively. Samples were finally stored at 4°C in 1 × TAE-$MgCl_2$ for no longer than 1 week.

### Steady-state ensemble spectroscopic characterization

Absorbance spectra were measured using an Evolution 260 Bio UV-Vis spectrophotometer (Thermo-Fisher) and fluorescence spectra ($\lambda_{exc}$ = 515 nm) were measured using a FluoroMax-4C (Horiba Jobin Yvon). For fluorescence measurements, a sample absorbance of 0.1 or less was maintained to avoid reabsorption effects. Quantum yields of DNA constructs were determined using the relative quantum yield determination method with rhodamine 101 in spectroscopic-grade ethanol ($\Phi_F$ = 0.92 measured using integrating sphere method) as Wurth et al.[100] All fluorescence spectra are corrected for lamp fluctuations and detector sensitivity (or S1c/R1c detector setting). The absorbance and fluorescence spectra of all the samples were measured in 10-mm pathlength quartz micro cuvettes (Millipore Sigma, catalog number: Z802662).

Steady-state ensemble energy-transfer efficiencies were estimated using steady-state fluorescence quenching experiments. The energy-transfer efficiency ($\Phi_{ET}$) of Cy3 to Cy5 was estimated by

$$\Phi_{ET} = 1 - \frac{\int_{\lambda_{em,min}}^{\lambda_{em,max}} I_{Cy3+Cy5} d\lambda_{em}}{\int_{\lambda_{em,min}}^{\lambda_{em,max}} I_{Cy3} d\lambda_{em}} \qquad \text{(Equation 1)}$$

where $\int_{\lambda_{em,min}}^{\lambda_{em,max}} I_{Cy3+Cy5}$ and $\int_{\lambda_{em,min}}^{\lambda_{em,max}} I_{Cy3}$ are the integrated fluorescence intensities of Cy3 measured from $\lambda_{em,max}$ = 520 nm to $\lambda_{em,min}$ = 750 nm in the presence or absence of Cy5, respectively. All samples were excited at $\lambda_{exc}$ = 515 nm. The full fluorescence spectra of Cy3 used to calculate $\int_{\lambda_{em,min}}^{\lambda_{em,max}} I_{Cy3+Cy5}$ were obtained by spectral decomposition of the Cy3 and Cy5 spectra using least-squares fitting which is detailed in Section S3.3.

### Ensemble time-resolved fluorescence lifetime

Ensemble fluorescence lifetime measurements were performed with a pulsed excitation source centered at 520 nm. A supercontinuum was generated by focusing a Ti:Sapphire laser (Vitara-S, Coherent; $\lambda_c$ = 800 nm, $\Delta\lambda$ = 70 nm, 20 fs pulse duration, 80 MHz repetition rate) into a nonlinear photonic crystal fiber (FemtoWhite 800, NKT photonics) and the desired spectral range was selected using a band-pass filter (Thorlabs; FB520-10). Fluorescence was collected at magic angle and passed through a long-pass filter (Omega Optics; 560LP RapidEdge), an inverted long-pass filter (Semrock; BLP01-647R-25), and a band-pass filter (Omega Optics; 580BP100 RapidBand). Single photons were collected by an SPAD (Micro Photon

Devices) and arrival times were recorded by a time-correlated single-photon module (Picoquant; PicoHarp 300). Instrument response function (IRF) was measured to be 56 ps. Histogrammed fluorescence lifetime was analyzed by least-squares reconvolution and fitted to the minimum number of components required to obtain the least structured residual.

Fluorescence anisotropy was obtained by time-resolved polarized fluorescence experiments (Table S18). The excitation and emission filters used were the same as above. Polarized fluorescence decay traces, parallel ($I_{\parallel}(t)$) and perpendicular ($I_{\perp}(t)$), were collected and used to calculate time-resolved fluorescence anisotropy, $r(t)$, as follows:

$$r(t) = \frac{I_{\parallel}(t) - G \times I_{\perp}(t)}{I_{\parallel}(t) + 2 \times G \times I_{\perp}(t)} \quad \text{(Equation 2)}$$

$$r(t) = (r_0 - r_\infty)\left[A\exp(-t/\tau_1) + (1-A)\exp(-t/\tau_2)\right] + r_\infty \quad \text{(Equation 3)}$$

$G$ was determined experimentally to be 0.43 using the intensity ratio of rhodamine 101 solution in glycerol:

$$G = \frac{I_{HV}}{I_{HH}} \quad \text{(Equation 4)}$$

where $I_{HV}$ and $I_{HH}$ are the background-subtracted fluorescence intensities excited with perpendicularly polarized light and detected in parallel and perpendicular, respectively.

### Femtosecond spectroscopy

Details of 2D electronic spectroscopy are given in the supplemental information, and the setup is described elsewhere.[101,102] Briefly, 2.8 W of the 5 W output from a 5 kHz Ti:sapphire regenerative amplifier (Coherent Libra) with a 40-fs duration and 800-nm center wavelength was focused into a 1-m tube of argon to generate a broadband continuum. The sub-805-nm portion of the continuum was filtered with a Schott glass filter (Thorlabs FGV9) to provide a center wavelength of 530 nm with a FWHM of 50 nm. The pulse was compressed to 11 fs by two pairs of chirped mirrors (Ultrafast Innovations GmbH) as characterized by a transient grating frequency-resolved optical gating experiment (Section S2.1). The 2D data were collected in a BOXCARS geometry[65,101] with an attenuated local oscillator ($\Delta t_{LO}$ = 500 fs). The coherence times were scanned with 0.25 fs steps from −175 fs to +175fs. Further details are given in Section S6.1.

Homodyne transient grating measurements were performed with the same geometry as the 2DES experiments in the absence of a local oscillator. Here, the time delay between pulses one and two was 0 fs while the time delay between pulses 2 and 3 was scanned to recover the transient grating spectrum at time steps of 1.3 fs for delay times from 0 to 2 ps.

### Single-molecule fluorescence spectroscopy

Single-molecule fluorescence lifetime measurements were performed with a home-built confocal microscope. Excitation light centered at 550 nm was obtained by filtering the same supercontinuum generated above for ensemble fluorescence spectroscopy with a band-pass filter (Omega Optics; RPB 540-560 RapidBand). Fluorescence was collected using the same emission filter set as for ensemble time-resolved fluorescence spectroscopy described above. Excitation power was set to 5.5 μJ $cm^{-2}$ per pulse at the sample plane. The sample was immobilized onto a quartz coverslip (Electron Microscope

Sciences) via aminosilane functionalization[103] and 2% biotin-PEGylated surface. While imaging, the sample was immersed in an imaging buffer (1 × TAE-$MgCl_2$) containing triplet (Sigma-Aldrich; Trolox at 2 mM final concentration) and enzymatic oxygen scavengers (protocatechuic acid/protocatechuic-3,4-dioxygenase at final concentrations of 2.5 mM/25 nM). The excitation laser was focused onto the sample and fluorescence was collected with the same oil-immersion objective (Olympus; UPLSAPO100XO, NA = 1.4). Single photons were collected by an avalanche photodiode (Excelitas; SPCM-AQRH-15) and arrival times were recorded by the same time-correlated single-photon counting module as used in ensemble fluorescence experiments. The instrument response function (IRF) was measured to be ~380 ps (full width at half maximum) by scattering excitation beam off a clean glass coverslip. All data analysis was performed in MATLAB (MathWorks). Representative data and examples of data analysis are in Section S4).

## All-atom MD simulations

The all-atom MD simulations were performed using the program Amber16[104] with the OL15 force field[105] for nucleic acids, and the GAFF2 force field[106] for the Cy3 molecules. Details of force field generation and all-atom system construction are given in Sections S6.2 and S6.3. Periodic boundary conditions were applied in an orthogonal simulation cell, and the dynamics were integrated at a time step of 2 fs. Van der Waals energies were calculated using a 12 Å cutoff. The Particle Mesh Ewald (PME) method was used to calculate full electrostatics with a grid spacing of 1 Å. Full electrostatic forces and non-bonded forces were calculated at each time step (2 fs). These simulations were performed in the *NpT* ensemble using a Berendsen barostat for pressure control at 1 bar,[107] and Langevin dynamics for temperature control at 300 K with a collision frequency of 5 $ps^{-1}$.[108] Hydrogen atom bonds were constrained to their equilibrium lengths using the SHAKE algorithm[109] during the simulations, and system configurations were recorded every 1 ps for downstream analysis. Prior to dynamics, energy minimization was performed on the solvent and ions alone, followed by the full unconstrained system for 10,000 steps each. Next, the solvent and ions were allowed to equilibrate as the system was heated to 300 K while the nucleic acid was harmonically constrained for 20 ps, followed by an unconstrained equilibration for 200 ps. For production dynamics, each system was run for 300 ns in duplicate (600 ns total). Structural analysis of MD simulations is outlined in Section S5.1. Results highlighting distributions of Cy3 configurations, SASA, and orientation factors are shown in Section S5.2.

## Cy3 excited-state calculations

The position of the Cy3 molecules was sampled at every 2 ns for 150 total configurations from each production MD simulation. The CPPTRAJ program,[110] as implemented in AmberTools17,[104] was utilized to extract the Cy3 coordinate data from each trajectory. Next, the phosphate groups in the sampled Cy3 molecules were replaced with hydrogen atoms, and density functional theory (DFT) was used to first optimize the hydrogen atom positions followed by a time-dependent DFT calculation[111,112] of the singlet excited states of the Cy3 molecules using the B3LYP functional,[113] the 6-31+G(d) Gaussian basis set,[114] and implicit COSMO water solvation,[115,116] as implemented in the NWChem 6.6 software package.[117] Excited-state energies from MD configurations are reported in Figures S30–S38. Calculation of monomeric and dimeric Cy3 optical properties are shown in Sections S5.3 and S5.4.

## Monte-Carlo FRET simulations

All-atom MD simulation of the duplex and DX structure were performed using the AMBER Molecular Dynamics package and the parameters described in the

supplemental information. Six replicates, each 100 ns in duration, were performed recording all atomic coordinates every 1 ps.

The data were analyzed using the CPPTraj software package[110] to extract the center of mass of each base pair and of the Cy3. The transition dipole moment unit vector of Cy3 was extracted as the unit vector from the N7 to the N17 atom. At each time point, and for each replicate the DNA axis was identified as the least-squares fit of the base pair center of mass. The DNA axis was used to define the z axis in the right-handed DNA-centered coordinate system, while the x axis was defined in the direction between the DNA axis and Cy3 center of mass. Dipole orientation statistics in this local coordinate system were then sampled for both scaffolds. The anisotropy fluorescence decay experiments were then simulated by computing the orientation correlation function of the transition dipole moment $\frac{2}{5}\left(\frac{3}{2}\langle\cos(\theta_t)\rangle - \frac{1}{2}\right)$, where $\theta_t = \arccos(\hat{\mu}_s \cdot \hat{\mu}_{s+t})$ is the angle between the transition dipole unit vectors $\hat{\mu}_s$ sampled a time t apart.

The position and orientation of the acceptor chromophore were obtained by assuming that the linker is always fully extended and the acceptor transition dipole is always parallel to the linker. These assumptions give rise to a cone of positions and orientations along a cone parallel to the axis of the DNA backbone, starting from the terminal base to which the acceptor is covalently bound. The direction of the linker axis was then sampled by selecting the polar angle from a normal distribution (mean $\overline{\theta}_A = 0$, standard deviation $\sigma_A = 33^\circ$) parametrized by the observed residual anisotropy, and by selecting the azimuthal angle from a uniform distribution. The polar angle was then rejected with a probability $P_R = \sin\theta$ to correctly weight the spherical samples. This algorithm yielded the same distribution of acceptor positions and orientations for both scaffoldings considered.

The donor chromophore position and orientation were sampled using two different models. In the first normal model, the position of the donor dye center of mass was taken to be fixed at its attachment position along the DNA scaffolding as a result of the double tether. Its orientation was then sampled, similarly to the acceptor, from a cone parallel to the DNA backbone axis. The polar angles were sampled from a normal distribution using the same algorithm as the acceptor with mean $\overline{\theta}_D = 0$ and scaffolding dependent standard deviation ($\sigma_{\text{duplex}} = 16^\circ$, $\sigma_{\text{DX}} = 22^\circ$) and the azimuthal angle was sampled uniformly. The FRET efficiency and rate in this model was calculated for $10^4$ sampled donor and acceptor conformations. In the "Molecular Dynamics" model, the positions and orientations of the donor chromophore were instead sampled directly from the MD simulation where a donor and acceptor position was selected for each frame.

To compute the FRET efficiency in the static limit, corresponding to an ensemble where chromophore reorientation occurs much slower than energy transfer, the FRET efficiency was computed for each conformation and then averaged to obtain the mean efficiency. The FRET efficiency in the dynamic limit, corresponding to a system where dipoles reorient much faster than energy transfer, is calculated by instead computing the FRET rate for each conformation. The average of this rate is then used to compute the overall efficiency of the FRET process.

## SUPPLEMENTAL INFORMATION

Supplemental information can be found online at https://doi.org/10.1016/j.chempr.2020.12.020.

## ACKNOWLEDGMENTS

Work by S.M.H., A.D., M.B., and G.S.S.-C. was supported by the US Department of Energy (DOE), Office of Science, Basic Energy Sciences (BES) under award DE-SC001999. Work by J.L.B. was supported by the DOE, Office of Science, BES under award DE-SC001999 (DNA construct assembly and characterization for 2D spectroscopy) and by the National Science Foundation (NSF) RAISE TAQS under award number 1839155 (DNA construct assembly for ensemble and single-molecule fluorescence measurements). Work by J.L.B. (circular dichroism spectroscopy and DNA denaturation experiments) and M.B. was supported by the US Army Research Office accomplished under cooperative agreement W911NF-19-2-0026 for the Institute for Collaborative Biotechnologies. Work by W.J.C. and W.P.B. was supported by the NSF RAISE TAQS under award number 1839155. Work by W.P.B. and M.B. was also supported by the Office of Naval Research award number N00014-17-1-2609. The Office of Naval Research award numbers N00014-13-1-0664 and N00014- 15-1-2830 funded the High-Performance Cluster used to perform simulations in this work. Work by L.M., Y.V., and R.H. was supported by the Swiss Nation Foundation grant number 200020_188468. S.M.H. acknowledges an NSF Graduate Research Fellowship. W.J.C. acknowledges an NSERC Postgraduate Scholarship. M.B. acknowledges funding from the preceding sources to support research design and direction according to the attributions of J.L.B. and W.P.B. G.S.S.-C. acknowledges a Beckman Young Investigator award, a Sloan Research Fellowship in Chemistry, and a CIFAR Global Scholar award.

## AUTHOR CONTRIBUTIONS

Conceptualization, J.L.B., R.H., M.B., and G.S.S.-C.; formal analysis, W.P.B., A.D., and W.J.C.; investigation, S.M.H., W.J.C., J.L.B., W.P.B., and A.D.; resources, L.M., Y.V., and J.L.B.; software, W.P.B. and A.D.; writing – original draft, S.M.H., W.J.C., J.L.B., and G.S.S.-C.; writing – review & editing, S.M.H., W.J.C., J.L.B., W.P.B., A.D., L.M., Y.V., A.P.W., R.H., M.B., and G.S.S.-C.; funding acquisition, A.P.W., R.H., M.B., and G.S.S.-C.; supervision, A.P.W., R.H., M.B., and G.S.S.-C.

## DECLARATION OF INTERESTS

The authors declare no competing interests.

Received: July 22, 2020
Revised: October 26, 2020
Accepted: December 17, 2020
Published: January 14, 2021; corrected online: February 18, 2021

## REFERENCES

1. Blankenship, R.E. (2014). Molecular Mechanisms of Photosynthesis, Second Edition (John Wiley & Sons).

2. van Grondelle, R., Bergström, H., Sundström, V., and Gillbro, T. (1987). Energy transfer within the bacteriochlorophyll antenna of purple bacteria at 77 K studied by picosecond absorption recovery. Biochim. Biophys. Acta *894*, 313–326.

3. Cogdell, R.J., Gall, A., and Köhler, J. (2006). The architecture and function of the light-harvesting apparatus of purple bacteria: from single molecules to in vivo membranes. Q. Rev. Biophys. *39*, 227–324.

4. Scholes, G.D., and Fleming, G.R. (2000). On the mechanism of light harvesting in photosynthetic purple bacteria: B800 to B850 energy transfer. J. Phys. Chem. B *104*, 1854–1868.

5. Scholes, G.D., Fleming, G.R., Chen, L.X., Aspuru-Guzik, A., Buchleitner, A., Coker, D.F., Engel, G.S., van Grondelle, R., Ishizaki, A., Jonas, D.M., et al. (2017). Using coherence to enhance function in chemical and biophysical systems. Nature *543*, 647–656.

6. Schaibley, J.R., Yu, H., Clark, G., Rivera, P., Ross, J.S., Seyler, K.L., Yao, W., and Xu, X. (2016). Valleytronics in 2D materials. Nat. Rev. Mater. *1*, 16055.

7. Noriega, R., Finley, D.T., Haberstroh, J., Geissler, P.L., Francis, M.B., and Ginsberg, N.S. (2015). Manipulating excited-state dynamics of individual light-harvesting chromophores through restricted motions in a hydrated nanoscale protein cavity. J. Phys. Chem. B *119*, 6963–6973.

8. So, M.C., Wiederrecht, G.P., Mondloch, J.E., Hupp, J.T., and Farha, O.K. (2015). Metal–organic framework materials for light-harvesting and energy transfer. Chem. Commun. *51*, 3501–3510.

9. Scholes, G.D., Fleming, G.R., Olaya-Castro, A., and van Grondelle, R. (2011). Lessons from

nature about solar light harvesting. Nat. Chem. *3*, 763–774.

10. Scholes, G.D., and Rumbles, G. (2006). Excitons in nanoscale systems. Nat. Mater. *5*, 683–696.

11. Fleming, G.R., Schlau-Cohen, G.S., Amarnath, K., and Zaks, J. (2012). Design principles of photosynthetic light-harvesting. Faraday Discuss *155*, 27–41.

12. Cheng, Y.C., and Fleming, G.R. (2009). Dynamics of light harvesting in photosynthesis. Annu. Rev. Phys. Chem. *60*, 241–262.

13. Krueger, B.P., Scholes, G.D., and Fleming, G.R. (1998). Calculation of couplings and energy-transfer pathways between the pigments of LH2 by the ab initio transition density cube method. J. Phys. Chem. B *102*, 5378–5386.

14. Jimenez, R., Dikshit, S.N., Bradforth, S.E., and Fleming, G.R. (1996). Electronic excitation transfer in the LH2 complex of Rhodobacter sphaeroides. J. Phys. Chem. *100*, 6825–6834.

15. Wu, J., Liu, F., Shen, Y., Cao, J., and Silbey, R.J. (2010). Efficient energy transfer in light-harvesting systems, I: optimal temperature, reorganization energy and spatial–temporal correlations. New J. Phys. *12*, 105012.

16. Tiwari, V., Peters, W.K., and Jonas, D.M. (2013). Electronic resonance with anticorrelated pigment vibrations drives photosynthetic energy transfer outside the adiabatic framework. Proc. Natl. Acad. Sci. USA *110*, 1203–1208.

17. Ishizaki, A., Calhoun, T.R., Schlau-Cohen, G.S., and Fleming, G.R. (2010). Quantum coherence and its interplay with protein environments in photosynthetic electronic energy transfer. Phys. Chem. Chem. Phys. *12*, 7319–7337.

18. Palmieri, B., Abramavicius, D., and Mukamel, S. (2009). Lindblad equations for strongly coupled populations and coherences in photosynthetic complexes. J. Chem. Phys. *130*, 204512.

19. Malý, P., Somsen, O.J., Novoderezhkin, V.I., Mančal, T., and van Grondelle, R. (2016). The role of resonant vibrations in electronic energy transfer. ChemPhysChem *17*, 1356–1368.

20. Saer, R., Orf, G.S., Lu, X., Zhang, H., Cuneo, M.J., Myles, D.A.A., and Blankenship, R.E. (2016). Perturbation of bacteriochlorophyll molecules in Fenna–Matthews–Olson protein complexes through mutagenesis of cysteine residues. Biochim. Biophys. Acta *1857*, 1455–1463.

21. Maiuri, M., Ostroumov, E.E., Saer, R.G., Blankenship, R.E., and Scholes, G.D. (2018). Coherent wavepackets in the Fenna–Matthews–Olson complex are robust to excitonic-structure perturbations caused by mutagenesis. Nat. Chem. *10*, 177–183.

22. Fresch, E., Meneghin, E., Agostini, A., Paulsen, H., Carbonera, D., and Collini, E. (2020). How the protein environment can tune the energy, the coupling, and the ultrafast dynamics of interacting chlorophylls: the example of the water-soluble chlorophyll protein. J. Phys. Chem. Lett. *11*, 1059–1067.

23. Yaghi, O.M., O'Keeffe, M., Ockwig, N.W., Chae, H.K., Eddaoudi, M., and Kim, J. (2003). Reticular synthesis and the design of new materials. Nature *423*, 705–714.

24. Delor, M., Dai, J., Roberts, T.D., Rogers, J.R., Hamed, S.M., Neaton, J.B., Geissler, P.L., Francis, M.B., and Ginsberg, N.S. (2018). Exploiting chromophore–protein interactions through linker engineering to tune photoinduced dynamics in a biomimetic light-harvesting platform. J. Am. Chem. Soc. *140*, 6278–6287.

25. Miller, R.A., Presley, A.D., and Francis, M.B. (2007). Self-assembling light-harvesting systems from synthetically modified tobacco mosaic virus coat proteins. J. Am. Chem. Soc. *129*, 3104–3109.

26. King, N.P., Bale, J.B., Sheffler, W., McNamara, D.E., Gonen, S., Gonen, T., Yeates, T.O., and Baker, D. (2014). Accurate design of co-assembling multi-component protein nanomaterials. Nature *510*, 103–108.

27. Li, X., Sinks, L.E., Rybtchinski, B., and Wasielewski, M.R. (2004). Ultrafast aggregate-to-aggregate energy transfer within self-assembled light-harvesting columns of zinc phthalocyanine tetrakis (perylenediimide). J. Am. Chem. Soc. *126*, 10810–10811.

28. Didraga, C., Klugkist, J.A., and Knoester, J. (2002). Optical properties of helical cylindrical molecular aggregates: the homogeneous limit. J. Phys. Chem. B *106*, 11474–11486.

29. Butkus, V., Valkunas, L., and Abramavicius, D. (2014). Vibronic phenomena and exciton–vibrational interference in two-dimensional spectra of molecular aggregates. J. Chem. Phys. *140*, 034306.

30. Lim, J., Paleček, D., Caycedo-Soler, F., Lincoln, C.N., Prior, J., Von Berlepsch, H., Huelga, S.F., Plenio, M.B., Zigmantas, D., and Hauer, J. (2015). Vibronic origin of long-lived coherence in an artificial molecular light harvester. Nat. Commun. *6*, 7755.

31. Collini, E., and Scholes, G.D. (2009). Coherent intrachain energy migration in a conjugated polymer at room temperature. Science *323*, 369–373.

32. Hayes, D., Griffin, G.B., and Engel, G.S. (2013). Engineering coherence among excited states in synthetic heterodimer systems. Science *340*, 1431–1434.

33. Brown, K.E., Salamant, W.A., Shoer, L.E., Young, R.M., and Wasielewski, M.R. (2014). Direct observation of ultrafast excimer formation in covalent perylenediimide dimers using near-infrared transient absorption spectroscopy. J. Phys. Chem. Lett. *5*, 2588–2593.

34. Halpin, A., Johnson, P.J., Tempelaar, R., Murphy, R.S., Knoester, J., Jansen, T.L., and Miller, R.J. (2014). Two-dimensional spectroscopy of a molecular dimer unveils the effects of vibronic coupling on exciton coherences. Nat. Chem. *6*, 196–201.

35. Wang, L., Griffin, G.B., Zhang, A., Zhai, F., Williams, N.E., Jordan, R.F., and Engel, G.S. (2017). Controlling quantum-beating signals in 2D electronic spectra by packing synthetic heterodimers on single-walled carbon nanotubes. Nat. Chem. *9*, 219–225.

36. Cannon, B.L., Patten, L.K., Kellis, D.L., Davis, P.H., Lee, J., Graugnard, E., Yurke, B., and Knowlton, W.B. (2018). Large Davydov splitting and strong fluorescence suppression: an investigation of exciton delocalization in dna-templated Holliday junction dye aggregates. J. Phys. Chem. A *122*, 2086–2095.

37. Cannon, B.L., Kellis, D.L., Patten, L.K., Davis, P.H., Lee, J., Graugnard, E., Yurke, B., and Knowlton, W.B. (2017). Coherent exciton delocalization in a two-state DNA-templated dye aggregate system. J. Phys. Chem. A *121*, 6905–6916.

38. Kringle, L., Sawaya, N.P.D., Widom, J., Adams, C., Raymer, M.G., Aspuru-Guzik, A., and Marcus, A.H. (2018). Temperature-dependent conformations of exciton-coupled Cy3 dimers in double-stranded DNA. J. Chem. Phys. *148*, 085101.

39. Cunningham, P.D., Kim, Y.C., Díaz, S.A., Buckhout-White, S., Mathur, D., Medintz, I.L., and Melinger, J.S. (2018). Optical properties of vibronically coupled Cy3 dimers on DNA scaffolds. J. Phys. Chem. B *122*, 5020–5029.

40. Mandal, S., Zhou, X., Lin, S., Yan, H., and Woodbury, N.W. (2019). Directed energy transfer through DNA-templated J-aggregates. Bioconjugate Chem *30*, 1870–1879.

41. Zhou, X., Mandal, S., Jiang, S., Lin, S., Yang, J., Liu, Y., Whitten, D.G., Woodbury, N.W., and Yan, H. (2019). Efficient long-range, directional energy transfer through DNA-templated dye aggregates. J. Am. Chem. Soc. *141*, 8473–8481.

42. Boulais, É., Sawaya, N.P.D., Veneziano, R., Andreoni, A., Banal, J.L., Kondo, T., Mandal, S., Lin, S., Schlau-Cohen, G.S., Woodbury, N.W., et al. (2018). Programmed coherent coupling in a synthetic DNA-based excitonic circuit. Nat. Mater. *17*, 159–166.

43. Banal, J.L., Kondo, T., Veneziano, R., Bathe, M., and Schlau-Cohen, G.S. (2017). Photophysics of J-aggregate-mediated energy transfer on DNA. J. Phys. Chem. Lett. *8*, 5827–5833.

44. Mazuski, R.J., Díaz, S.A., Wood, R.E., Lloyd, L.T., Klein, W.P., Mathur, D., Melinger, J.S., Engel, G.S., and Medintz, I.L. (2020). Ultrafast excitation transfer in Cy5 DNA photonic wires displays dye conjugation and excitation energy dependency. J. Phys. Chem. Lett. *11*, 4163–4172.

45. Adeyemi, O.O., Malinovskii, V.L., Biner, S.M., Calzaferri, G., and Häner, R. (2012). Photon harvesting by excimer-forming multichromophores. Chem. Commun. *48*, 9589–9591.

46. Probst, M., Wenger, D., Biner, S.M., and Häner, R. (2012). The DNA three-way junction as a mould for tripartite chromophore assembly. Org. Biomol. Chem. *10*, 755–759.

47. Hemmig, E.A., Creatore, C., Wünsch, B., Hecker, L., Mair, P., Parker, M.A., Emmott, S., Tinnefeld, P., Keyser, U.F., and Chin, A.W. (2016). Programming light-harvesting

efficiency using DNA origami. Nano Lett *16*, 2369–2374.

48. Dutta, P.K., Varghese, R., Nangreave, J., Lin, S., Yan, H., and Liu, Y. (2011). DNA-directed artificial light-harvesting antenna. J. Am. Chem. Soc. *133*, 11985–11993.

49. Garo, F., and Häner, R. (2012). A DNA-based light-harvesting antenna. Angew. Chem. Int. Ed. *51*, 916–919.

50. Markova, L.I., Malinovskii, V.L., Patsenker, L.D., and Häner, R. (2013). J-vs. H-type assembly: pentamethine cyanine (Cy5) as a near-IR chiroptical reporter. Chem. Commun. *49*, 5298–5300.

51. Cunningham, P.D., Díaz, S.A., Yurke, B., Medintz, I.L., and Melinger, J.S. (2020). Delocalized two-exciton states in dna scaffolded cyanine dimers. J. Phys. Chem. B *124*, 8042–8049.

52. Heussman, D., Kittell, J., Kringle, L., Tamimi, A., von Hippel, P.H., and Marcus, A.H. (2019). Measuring local conformations and conformational disorder of (Cy3)2 dimer labeled DNA fork junctions using absorbance, circular dichroism and two-dimensional fluorescence spectroscopy. Faraday Discuss. *216*, 211–235.

53. Cipolloni, M., Fresch, B., Occhiuto, I., Rukin, P., Komarova, K.G., Cecconello, A., Willner, I., Levine, R.D., Remacle, F., and Collini, E. (2017). Coherent electronic and nuclear dynamics in a rhodamine heterodimer–dna supramolecular complex. Phys. Chem. Chem. Phys. *19*, 23043–23051.

54. Sohail, S.H., Otto, J.P., Cunningham, P.D., Kim, Y.C., Wood, R.E., Allodi, M.A., Higgins, J.S., Melinger, J.S., and Engel, G.S. (2020). DNA scaffold supports long-lived vibronic coherence in an indodicarbocyanine (Cy5) dimer. Chem. Sci. *11*, 8546–8557.

55. Nicoli, F., Roos, M.K., Hemmig, E.A., Di Antonio, M., de Vivie-Riedle, R., and Liedl, T. (2016). Proximity-induced H-aggregation of cyanine dyes on DNA-duplexes. J. Phys. Chem. A *120*, 9941–9947.

56. Mustroph, H., Reiner, K., Mistol, J., Ernst, S., Keil, D., and Hennig, L. (2009). Relationship between the molecular structure of cyanine dyes and the vibrational fine structure of their electronic absorption spectra. ChemPhysChem *10*, 835–840.

57. Hestand, N.J., and Spano, F.C. (2018). Expanded theory of H- and J-molecular aggregates: the effects of vibronic coupling and intermolecular charge transfer. Chem. Rev. *118*, 7069–7163.

58. Sundström, V., and Gillbro, T. (1985). Excited state dynamics and photophysics of aggregated dye chromophores in solution. J. Chem. Phys. *83*, 2733–2743.

59. Dean, J.C., Oblinsky, D.G., Rafiq, S., and Scholes, G.D. (2016). Methylene blue exciton states steer nonradiative relaxation: ultrafast spectroscopy of methylene blue dimer. J. Phys. Chem. B *120*, 440–454.

60. Huff, J.S., Davis, P.H., Christy, A., Kellis, D.L., Kandadai, N., Toa, Z.S.D., Scholes, G.D., Yurke, B., Knowlton, W.B., and Pensack, R.D. (2019). DNA-templated aggregates of strongly coupled cyanine dyes: nonradiative decay governs exciton lifetimes. J. Phys. Chem. Lett. *10*, 2386–2392.

61. Stennett, E.M., Ma, N., Van Der Vaart, A., and Levitus, M. (2014). Photophysical and dynamical properties of doubly linked Cy3–DNA constructs. J. Phys. Chem. B *118*, 152–163.

62. Arnott, S., Chandrasekaran, R., Hall, I.H., Puigjaner, L.C., Walker, J.K., and Wang, M. (1983). DNA secondary structures: helices, wrinkles, and junctions. Cold Spring Harb. Symp. Quant. Biol. *47*, 53–65.

63. Kjellberg, P., Brüggemann, B., and Pullerits, T. (2006). Two-dimensional electronic spectroscopy of an excitonically coupled dimer. Phys. Rev. B *74*, 024303.

64. Gallagher Faeder, S.M., and Jonas, D.M. (1999). Two-dimensional electronic correlation and relaxation spectra: theory and model calculations. J. Phys. Chem. A *103*, 10489–10505.

65. Fuller, F.D., and Ogilvie, J.P. (2015). Experimental implementations of two-dimensional Fourier transform electronic spectroscopy. Annu. Rev. Phys. Chem. *66*, 667–690.

66. Szöcs, V., Pálszegi, T., Lukeš, V., Sperling, J., Milota, F., Jakubetz, W., and Kauffmann, H.F. (2006). Two-dimensional electronic spectra of symmetric dimers: intermolecular coupling and conformational states. J. Chem. Phys. *124*, 124511.

67. Cho, M., Vaswani, H.M., Brixner, T., Stenger, J., and Fleming, G.R. (2005). Exciton analysis in 2D electronic spectroscopy. J. Phys. Chem. B *109*, 10542–10556.

68. Petkov, B.K., Gellen, T.A., Farfan, C.A., Carbery, W.P., Hetzler, B.E., Trauner, D., Li, X., Glover, W.J., Ulness, D.J., and Turner, D.B. (2019). Two-dimensional electronic spectroscopy reveals the spectral dynamics of Förster resonance energy transfer. Chem *5*, 2111–2125.

69. Rothemund, P.W. (2006). Folding dna to create nanoscale shapes and patterns. Nature *440*, 297–302.

70. Douglas, S.M., Dietz, H., Liedl, T., Högberg, B., Graf, F., and Shih, W.M. (2009). Self-assembly of DNA into nanoscale three-dimensional shapes. Nature *459*, 414–418.

71. Veneziano, R., Ratanalert, S., Zhang, K., Zhang, F., Yan, H., Chiu, W., and Bathe, M. (2016). Designer nanoscale DNA assemblies programmed from the top down. Science *352*, 1534.

72. Jun, H., Zhang, F., Shepherd, T., Ratanalert, S., Qi, X., Yan, H., and Bathe, M. (2019). Autonomously designed free-form 2D DNA origami. Sci. Adv. *5*, eaav0655.

73. Jun, H., Shepherd, T.R., Zhang, K., Bricker, W.P., Li, S., Chiu, W., and Bathe, M. (2019). Automated sequence design of 3D polyhedral wireframe DNA origami with honeycomb edges. ACS Nano *13*, 2083–2093.

74. Jun, H., Wang, X., Bricker, W.P., and Bathe, M. (2019). Automated sequence design of 2D wireframe dna origami with honeycomb edges. Nat. Commun. *10*, 5419.

75. Wamhoff, E.C., Banal, J.L., Bricker, W.P., Shepherd, T.R., Parsons, M.F., Veneziano, R., Stone, M.B., Jun, H., Wang, X., and Bathe, M. (2019). Programming structured DNA assemblies to probe biophysical processes. Annu. Rev. Biophys. *48*, 395–419.

76. Li, X., Yang, X., Qi, J., and Seeman, N.C. (1996). Antiparallel DNA double crossover molecules as components for nanoconstruction. J. Am. Chem. Soc. *118*, 6131–6140.

77. Sa-Ardyen, P., Vologodskii, A.V., and Seeman, N.C. (2003). The flexibility of DNA double crossover molecules. Biophys. J. *84*, 3829–3837.

78. Kwak, K., Park, S., Finkelstein, I.J., and Fayer, M.D. (2007). Frequency-frequency correlation functions and apodization in two-dimensional infrared vibrational echo spectroscopy: a new approach. J. Chem. Phys. *127*, 124503.

79. Šanda, F., Perlík, V., Lincoln, C.N., and Hauer, J. (2015). Center line slope analysis in two-dimensional electronic spectroscopy. J. Phys. Chem. A *119*, 10893–10909.

80. Nemeth, A., Milota, F., Mančal, T., Lukeš, V., Hauer, J., Kauffmann, H.F., and Sperling, J. (2010). Vibrational wave packet induced oscillations in two-dimensional electronic spectra. I. experiments. J. Chem. Phys. *132*, 184514.

81. Mančal, T., Nemeth, A., Milota, F., Lukeš, V., Kauffmann, H.F., and Sperling, J. (2010). Vibrational wave packet induced oscillations in two-dimensional electronic spectra. II. Theory. J. Chem. Phys. *132*, 184515.

82. Nowakowski, P.J., Khyasudeen, M.F., and Tan, H.-S. (2018). The effect of laser pulse bandwidth on the measurement of the frequency fluctuation correlation functions in 2D electronic spectroscopy. Chem. Phys. *515*, 214–220.

83. Khyasudeen, M.F., Nowakowski, P.J., and Tan, H.S. (2019). Measuring the ultrafast correlation dynamics between the Qx and Qy bands in chlorophyll molecules. J. Phys. Chem. B *123*, 1359–1364.

84. Hart, S.M., Banal, J.L., Bathe, M., and Schlau-Cohen, G. (2020). Identification of non-radiative decay pathways in Cy3. J. Phys. Chem. Lett. *11*, 5000–5007.

85. Alden, C.J., and Kim, S.H. (1979). Solvent-accessible surfaces of nucleic acids. J. Mol. Biol. *132*, 411–434.

86. Sanborn, M.E., Connolly, B.K., Gurunathan, K., and Levitus, M. (2007). Fluorescence properties and photophysics of the sulfoindocyanine Cy3 linked covalently to DNA. J. Phys. Chem. B *111*, 11064–11074.

87. Weinreis, S.A., Ellis, J.P., and Cavagnero, S. (2010). Dynamic fluorescence depolarization: a powerful tool to explore protein folding on the ribosome. Methods *52*, 57–73.

88. Förster, T. (1948). Zwischenmolekulare energiewanderung und Fluoreszenz. Ann. Phys. *437*, 55–75.

89. Van Der Meer, B.W., Coker, G., and Chen, S.-Y.S. (1994). Resonance Energy Transfer: Theory and Data, First Edition (Wiley-VCH Verlag).

90. Dale, R.E., Eisinger, J., and Blumberg, W.E. (1979). The orientational freedom of molecular probes. the orientation factor in intramolecular energy transfer. Biophys. J. *26*, 161–193.

91. Stryer, L. (1978). Fluorescence energy transfer as a spectroscopic ruler. Annu. Rev. Biochem. *47*, 819–846.

92. VanBeek, D.B., Zwier, M.C., Shorb, J.M., and Krueger, B.P. (2007). Fretting about FRET: correlation between $\kappa$ and r. Biophys. J. *92*, 4168–4178.

93. Eilert, T., Kallis, E., Nagy, J., Röcker, C., and Michaelis, J. (2018). Complete kinetic theory of FRET. J. Phys. Chem. B *122*, 11677–11694.

94. Sindbert, S., Kalinin, S., Nguyen, H., Kienzler, A., Clima, L., Bannwarth, W., Appel, B., Müller, S., and Seidel, C.A. (2011). Accurate distance determination of nucleic acids via Förster resonance energy transfer: implications of dye linker length and rigidity. J. Am. Chem. Soc. *133*, 2463–2480.

95. Iqbal, A., Arslan, S., Okumus, B., Wilson, T.J., Giraud, G., Norman, D.G., Ha, T., and Lilley, D.M. (2008). Orientation dependence in fluorescent energy transfer between Cy3 and Cy5 terminally attached to double-stranded nucleic acids. Proc. Natl. Acad. Sci. USA *105*, 11176–11181.

96. Ivanov, V., Li, M., and Mizuuchi, K. (2009). Impact of emission anisotropy on fluorescence spectroscopy and fret distance measurements. Biophys. J. *97*, 922–929.

97. Chen, X., and Silbey, R.J. (2010). Effect of correlation of local fluctuations on exciton coherence. J. Chem. Phys. *132*, 204503.

98. Chen, X., and Silbey, R.J. (2011). Excitation energy transfer in a non-markovian dynamical disordered environment: localization, narrowing, and transfer efficiency. J. Phys. Chem. B *115*, 5499–5509.

99. Strümpfer, J., and Schulten, K. (2011). The effect of correlated bath fluctuations on exciton transfer. J. Chem. Phys. *134*, 095102.

100. Würth, C., Grabolle, M., Pauli, J., Spieles, M., and Resch-Genger, U. (2013). Relative and absolute determination of fluorescence quantum yields of transparent samples. Nat. Protoc. *8*, 1535–1550.

101. Son, M., Mosquera-Vázquez, S., and Schlau-Cohen, G.S. (2017). Ultrabroadband 2D electronic spectroscopy with high-speed, shot-to-shot detection. Opt. Express *25*, 18950–18962.

102. Son, M., Pinnola, A., Bassi, R., and Schlau-Cohen, G.S. (2019). The electronic structure of lutein 2 is optimized for light harvesting in plants. Chem *5*, 575–584.

103. Hua, B., Han, K.Y., Zhou, R., Kim, H., Shi, X., Abeysirigunawardena, S.C., Jain, A., Singh, D., Aggarwal, V., Woodson, S.A., et al. (2014). An improved surface passivation method for single-molecule studies. Nat. Methods *11*, 1233–1236.

104. Case, D., Cerutti, D., Cheatham, T., III, Darden, T., Duke, R., Giese, T., Gohlke, H., Goetz, A., Greene, D., Homeyer, N., et al. AMBER 2017 (University of California, San Francisco).

105. Galindo-Murillo, R., Robertson, J.C., Zgarbová, M., Šponer, J., Otyepka, M., Jurečka, P., and Cheatham, T.E., III. (2016). Assessing the current state of Amber force field modifications for DNA. J. Chem. Theor. Comput. *12*, 4114–4127.

106. Wang, J., Wolf, R.M., Caldwell, J.W., Kollman, P.A., and Case, D.A. (2004). Development and testing of a general Amber force field. J. Comput. Chem. *25*, 1157–1174.

107. Berendsen, H.J.C., Postma, J.P.M., van Gunsteren, W.F., DiNola, A., and Haak, J.R. (1984). Molecular Dynamics with coupling to an external bath. J. Chem. Phys. *81*, 3684–3690.

108. Izaguirre, J.A., Catarello, D.P., Wozniak, J.M., and Skeel, R.D. (2001). Langevin stabilization of molecular dynamics. J. Chem. Phys. *114*, 2090–2098.

109. Ryckaert, J.-P., Ciccotti, G., and Berendsen, H.J.C. (1977). Numerical integration of the Cartesian equations of motion of a system with constraints: molecular dynamics of n-alkanes. J. Comput. Phys. *23*, 327–341.

110. Roe, D.R., and Cheatham, T.E., III. (2013). PTRAJ and CPPTRAJ: software for processing and analysis of molecular dynamics trajectory data. J. Chem. Theor. Comput. *9*, 3084–3095.

111. Kohn, W., and Sham, L.J. (1965). Self-consistent equations including exchange and correlation effects. Phys. Rev. *140*, A1133–A1138.

112. Runge, E., and Gross, E.K.U. (1984). Density-functional theory for time-dependent systems. Phys. Rev. Lett. *52*, 997–1000.

113. Becke, A.D. (1993). Density-functional thermochemistry. III. The role of exact exchange. J. Chem. Phys. *98*, 5648–5652.

114. Hehre, W.J., Ditchfield, R., and Pople, J.A. (1972). Self-consistent molecular orbital methods. XII. Further extensions of Gaussian-type basis sets for use in molecular orbital studies of organic molecules. J. Chem. Phys. *56*, 2257–2261.

115. Klamt, A., and Schüürmann, G. (1993). COSMO: A new approach to dielectric screening in solvents with explicit expressions for the screening energy and its gradient. J. Chem. Soc. Perkin Trans. 2 *2*, 799–805.

116. York, D.M., and Karplus, M. (1999). A smooth solvation potential based on the conductor-like screening model. J. Phys. Chem. A *103*, 11060–11079.

117. Valiev, M., Bylaska, E.J., Govind, N., Kowalski, K., Straatsma, T.P., Van Dam, H.J.J., Wang, D., Nieplocha, J., Apra, E., Windus, T.L., et al. (2010). NWChem: A comprehensive and scalable open-source solution for large scale molecular simulations. Comput. Phys. Commun. *181*, 1477–1489.

**Chem, Volume *7***

## Supplemental Information

# Engineering couplings for exciton transport using synthetic DNA scaffolds

**Stephanie M. Hart, Wei Jia Chen, James L. Banal, William P. Bricker, Amro Dodin, Larysa Markova, Yuliia Vyborna, Adam P. Willard, Robert Häner, Mark Bathe, and Gabriela S. Schlau-Cohen**

# Contents

# List of Figures

# List of Tables

# S1 Supplemental Data: Characterization of linear Cy3 aggregates on DNA duplexes

## S1.1 DNA duplex sequences

**Table S1** | Single-stranded DNA sequences for linear Cy3 aggregates on DNA duplexes.

| Sequence identifier | ssDNA sequence (5' to 3' direction) |
|---|---|
| Cy3 monomer 1 | TGCACTCTCG**X**TGACCGAGCT |
| Cy3 monomer 2 | AGCTCGGTCATCGAGAGTGCA |
| Cy3 dimer 1 | TGCACTCTCG**XX**TGACCGAGCT |
| Cy3 dimer 2 | AGCTCGGTCATTCGAGAGTGCA |
| Cy3 trimer 1 | TGCACTCTCG**XXX**TGACCGAGCT |
| Cy3 trimer 2 | AGCTCGGTCATTTCGAGAGTGCA |
| Control DNA monomer 1 | TGCACTCTCGTTGACCGAGCT |
| Control DNA monomer 2 | AGCTCGGTCATCGAGAGTGCA |
| Control DNA dimer 1 | TGCACTCTCGTTTGACCGAGCT |
| Control DNA dimer 2 | AGCTCGGTCATTCGAGAGTGCA |
| Control DNA trimer 1 | TGCACTCTCGAAATGACCGAGCT |
| Control DNA trimer 2 | AGCTCGGTCATTTCGAGAGTGCA |

* **X** denotes internal Cy3 modification

## S1.2 Analytical characterization of Cy3 aggregates on DNA oligonucleotides

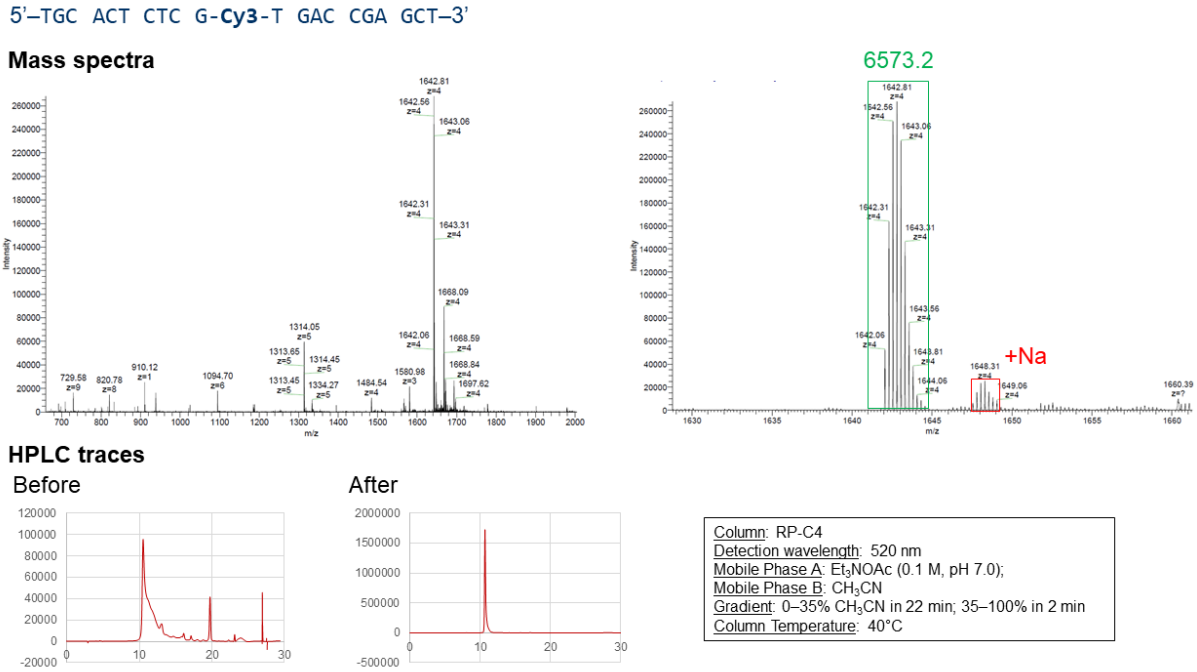


**Figure S1 | Characterization data for Cy3 monomer 1.** Top: Mass analysis using nanoelectrospray ionization mass spectrometry. Bottom: High-performance liquid chromatography (HPLC) purification traces of crude (before) and post-HPLC purification (after). Strands were purified using ion-pair reversed-phase HPLC with a linear gradient from 100% 0.1 M triethylammonium acetate ($Et_3NOAc$; ion-pair reagent) to 65% 0.1 M $Et_3NOAc$:35% acetonitrile over 22 minutes at 1 mL $min^{-1}$.

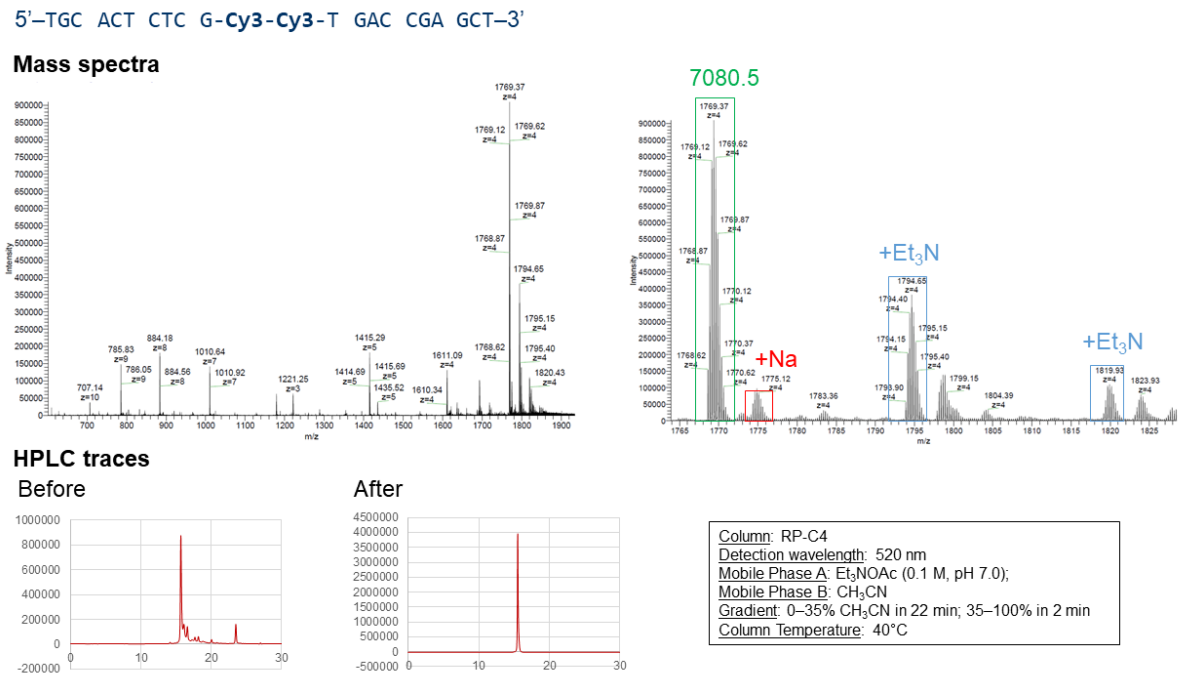


**Figure S2 | Characterization data for Cy3 dimer 1.** Top: Mass analysis using nanoelectrospray ionization mass spectrometry. Bottom: HPLC purification traces of crude (before) and post-HPLC purification (after). Strands were purified using ion-pair reversed-phase HPLC with a linear gradient from 100% 0.1 M triethylammonium acetate ($Et_3NOAc$; ion-pair reagent) to 65% 0.1 M $Et_3NOAc$:35% acetonitrile over 22 minutes at 1 mL $min^{-1}$.+$Et_3N$ is triethylammonium from the buffer used for ion-pair reversed-phase HPLC purification.

5'–TGC ACT CTC G-**Cy3-Cy3-Cy3**-T GAC CGA GCT–3'

**Mass spectra**

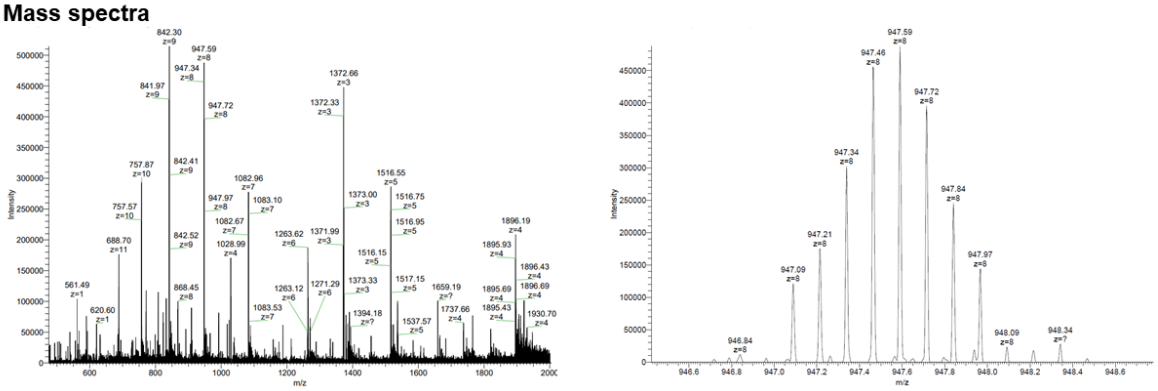


**HPLC trace**

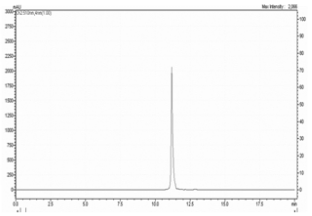

Column: RP-C4
Detection wavelength: 520 nm
Mobile Phase A: $Et_3NOAc$ (0.1 M, pH 7.0);
Mobile Phase B: $CH_3CN$
Gradient: 0–35% $CH_3CN$ in 22 min; 35–100% in 2 min
Column Temperature: 40°C

**Figure S3 | Characterization data for Cy3 trimer 1.** Top: Mass analysis using nanoelectrospray ionization mass spectrometry. Bottom: HPLC purification trace of purified oligonucleotide strand. Strands were purified using ion-pair reversed-phase HPLC with a linear gradient from 100% 0.1 M triethylammonium acetate ($Et_3NOAc$; ion-pair reagent) to 65% 0.1 M $Et_3NOAc$:35% acetonitrile over 22 minutes at 1 mL $min^{-1}$.

## S1.3 DNA melting profiles of Cy3-modified DNA duplexes

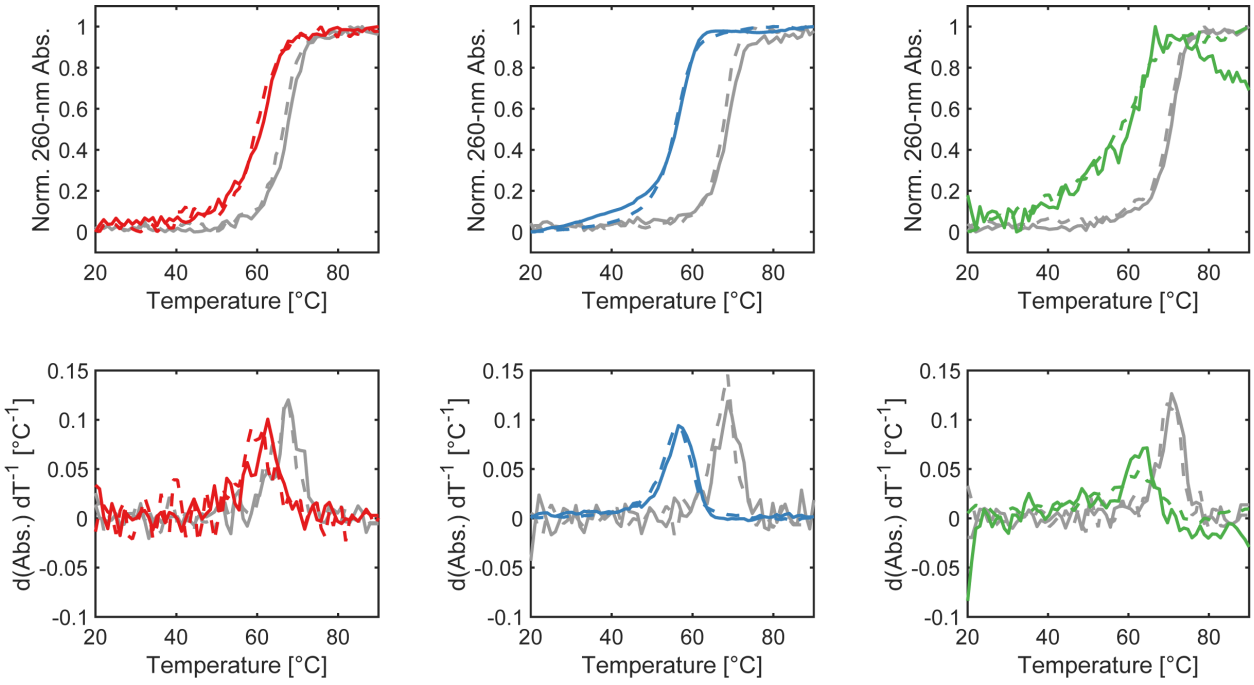


**Figure S4 | Temperature-dependent absorbance spectra of Cy3-modified DNA duplexes.** Top row: DNA melting and annealing curves of Cy3-modified DNA duplexes, monomer (red), dimer (blue), and trimer (green). Change in absorbance at 260 nm with temperature was monitored using UV spectrophotometry. Solid lines are DNA heating/melting curves that are measured from 20°C–90°C at a rate of $+1$°C min$^{-1}$. Broken lines are DNA cooling/annealing curves that are measured from 90°C–20°C at a rate of $-1$ °C min$^{-1}$. Bottom row: First-order derivatives of melting and annealing curves. Gray curves are canonical DNA duplex controls for comparison. [DNA] = 1.0 $\mu$M in 40 mM Tris, 20 mM acetate, 2 mM EDTA, 12 mM $MgCl_2$.

## S1.4 Determining molar absorption coefficients of Cy3-DNA duplex constructs using spectral decomposition

### S1.4.1 DNA sequences

**Table S2** | Single-stranded DNA sequences for linear Cy3 aggregates on DNA duplexes.

| Sequence identifier | ssDNA sequence (5' to 3' direction) |
|---|---|
| Cy3 monomer 1 | TGCACTCTCG**X**TGACCGAGCT |
| Cy3 monomer 2 + Cy5 | /Cy5/TAGCTCGGTCATCGAGAGTGCA |
| Cy3 dimer 1 | TGCACTCTCG**XX**TGACCGAGCT |
| Cy3 dimer 2 + Cy5 | /Cy5/TAGCTCGGTCATTCGAGAGTGCA |
| Cy3 trimer 1 | TGCACTCTCG**XXX**TGACCGAGCT |
| Cy3 trimer 2 + Cy5 | /Cy5/TAGCTCGGTCATTTCGAGAGTGCA |

* **X** denotes internal Cy3 modification

### S1.4.2 Spectral decomposition using least-square fitting

To validate our measured molar absorption coefficients of Cy3-DNA duplex constructs, we used a spectral decomposition approach using Cy3-DNA constructs that contain Cy5 as a fiducial marker (Table S2). Briefly, for a mixture

of multiple absorbing components and in the weak excitonic coupling regime, the total/sum spectra, $S$, is given by a linear combination of individual constituent spectra:

$$S = \alpha_1 \mathbf{X}_1 + \alpha_2 \mathbf{X}_2 + \ldots + \alpha_n \mathbf{X}_n \tag{1}$$

where $\alpha_n$ is the fractional contribution of each component spectra $\mathbf{X}_n$. If each component spectra $X_n$ is known, then the contribution factors $\alpha_n$ can be solved. The measured absorbance spectra of Cy3-DNA duplex constructs containing Cy5 were normalized at the Cy5 absorbance peak. We then used non-negative least square fitting to calculate the component spectra for Cy3 monomer, dimer, and trimer on DNA duplexes and Cy5. From the decomposed spectra of Cy3-DNA duplex constructs, the molar absorption coefficient of Cy5 at the maximum absorbance wavelength (250000 $M^{-1}$ $cm^{-1}$) was then multiplied to all the spectra and then corrected for the number of Cy3 chromophores per DNA duplex to obtain the molar absorption coefficients of the Cy3-DNA duplex constructs (Figure S5). The same approach was used to decompose the Cy3 and Cy5 components from fluorescence spectra that was collected from samples that were used to measure energy-transfer efficiencies (Supplemental Section S3.3).

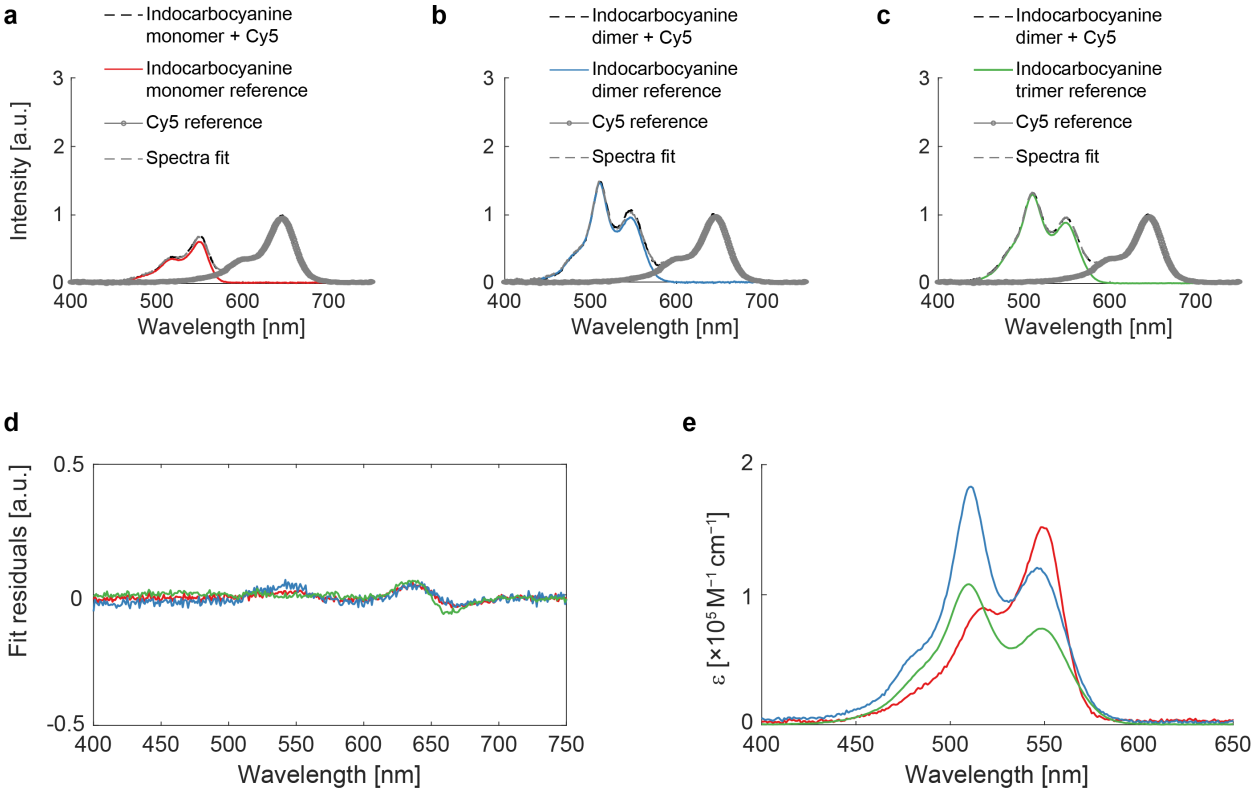


**Figure S5 | Spectral decomposition of Cy3 constructs with Cy5. (a–c)** Normalized spectra of Cy3-DNA constructs with Cy5 (black broken lines) or without Cy5 (solid lines, monomer: red, dimer: blue, trimer: green) and Cy5 spectra (solid lines with circle marker). Resulting spectra from spectral decomposition are overlaid as broken gray lines. **(d)** Fit residuals: $S_{\text{exp}} - S_{\text{fit}}$, where $S_{\text{exp}}$ is the normalized experimental absorbance spectra and $S_{\text{fit}}$ is the resulting absorbance spectra from linear squares fitting. **(e)** Calculated molar absorption coefficients of the Cy3-DNA duplex constructs.

## S1.5 Fluorescence lifetimes of linear aggregates of Cy3 on DNA duplexes

Individual fluorescence decay curves $I(t)$ were fitted with two-exponential decay function, in the case of the Cy3 monomer

$$I(t) = \text{IRF} \otimes \sum_{i=1}^{2} A_i \exp\left(-t/\tau_i\right) \tag{2}$$

or three-exponential decay function, in the case of the Cy3 dimer and trimer

$$I(t) = \mathrm{IRF} \otimes \sum_{i=1}^{3} A_i \exp\left(-t/\tau_i\right) \tag{3}$$

with the instrument response function (IRF) using iterative reconvolution. $A_i$ is the fractional amplitude of component $i$, and $\tau_i$ is the fluorescence lifetime constant of component $i$. Goodness-of-fit was determined by minimizing least-squares error without weighting and inspecting the fit residuals. The fit parameters for the traces shown in Main Text Figure 1e are shown below (Table S3).

**Table S3** | Fitting results of time-resolved lifetime measurements of Cy3 monomer, dimer, and trimer on DNA duplexes using Eq. 2 for monomer and Eq. 3 for dimer and trimer (non-magic angle).

| | $A_1$ | $\tau_1$ [ns] | $A_2$ | $\tau_2$ [ns] | $A_3$ | $\tau_3$ [ns] |
|---|---|---|---|---|---|---|
| Monomer | $0.53 \pm 0.03$ | $0.80 \pm 0.06$ | $0.47 \pm 0.03$ | $2.09 \pm 0.04$ | - | - |
| Dimer | $0.42 \pm 0.02$ | $0.11 \pm 0.02$ | $0.33 \pm 0.04$ | $1.09 \pm 0.11$ | $0.24 \pm 0.01$ | $3.43 \pm 0.26$ |
| Trimer | $0.59 \pm 0.01$ | $0.09 \pm 0.01$ | $0.28 \pm 0.01$ | $0.60 \pm 0.06$ | $0.11 \pm 0.01$ | $2.00 \pm 0.18$ |

## S1.6 Effect of complementary nucleotide on Cy3 monomers and dimers on DNA duplexes

### S1.6.1 DNA sequences

**Table S4** | Single-stranded DNA sequences for Cy3 monomers with different complementary nucleotides on DNA duplexes.

| Sequence identifier | ssDNA sequence (5' to 3' direction) |
|---|---|
| Cy3 monomer 1 | TGCACTCTCG**X**TGACCGAGCT |
| Cy3 monomer control | TGCACTCTCGATGACCGAGCT |
| Cy3 monomer 2 T | AGCTCGGTCATCGAGAGTGCA |
| Cy3 monomer 2 A | AGCTCGGTCAACGAGAGTGCA |
| Cy3 monomer 2 C | AGCTCGGTCACCGAGAGTGCA |
| Cy3 monomer 2 G | AGCTCGGTCAGCGAGAGTGCA |

* **X** denotes internal Cy3 modification

**Table S5** | Single-stranded DNA sequences for Cy3 dimers with different complementary nucleotides on DNA duplexes.

| Sequence identifier | ssDNA sequence (5' to 3' direction) |
|---|---|
| Cy3 dimer 1 | TGCACTCTCG**XX**TGACCGAGCT |
| Cy3 dimer control | TGCACTCTCGAATGACCGAGCT |
| Cy3 dimer 2 TT | AGCTCGGTCATTCGAGAGTGCA |
| Cy3 dimer 2 AA | AGCTCGGTCAAACGAGAGTGCA |
| Cy3 dimer 2 CC | AGCTCGGTCACCCGAGAGTGCA |
| Cy3 dimer 2 GG | AGCTCGGTCAGGCGAGAGTGCA |

* **X** denotes internal Cy3 modification

### S1.6.2 PAGE and steady-state ensemble characterization of DNA duplexes

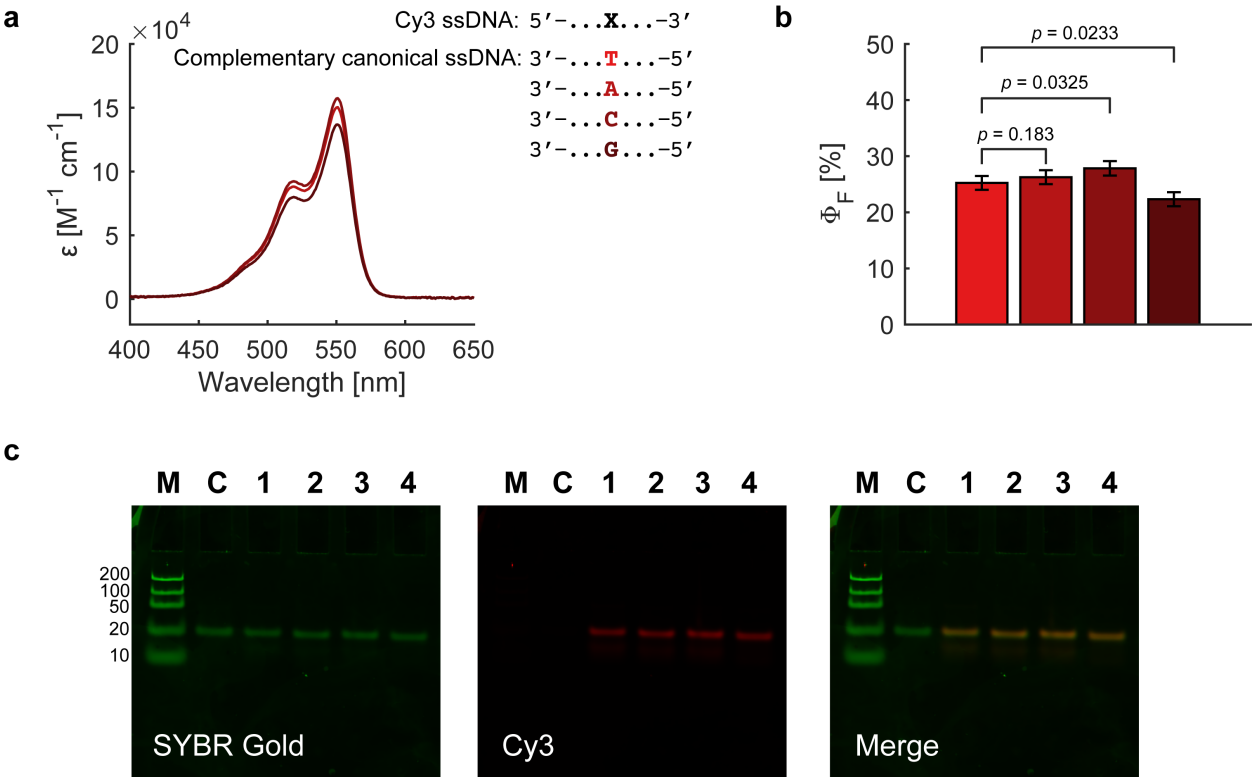


**Figure S6 | Dependence of Cy3 monomer quantum yield ($\Phi_F$) based on the complementary nucleotides. (a)** Measured absorbance spectra in units of molar absorption coefficient ($M^{-1}$ $cm^{-1}$) in 40 mM Tris, 20 mM acetate, 2 mM EDTA, 12 mM $MgCl_2$. **(b)** $\Phi_F$ of Cy3 monomer in the presence of different complementary nucleotides. Two-sample t-test with unequal variance was used for significance testing. Quantum yields are plotted as mean ± s.d. values that were calculated from measurements of three independent replicates. [DNA] = 0.5 $\mu$M. **(c)** Native 12% PAGE gel. **M:** Thermo-Scientific FastRuler Ultra Low Range DNA Ladder, **C:** Cy3 monomer control + Cy3 monomer 2 T, **1:** Cy3 monomer 1 + Cy3 monomer 2 T DNA duplex, **2:** Cy3 monomer 1 + Cy3 monomer 2 A DNA duplex, **3:** Cy3 monomer 1 + Cy3 monomer 2 C DNA duplex, **4:** Cy3 monomer 1 + Cy3 monomer 2 G DNA duplex.

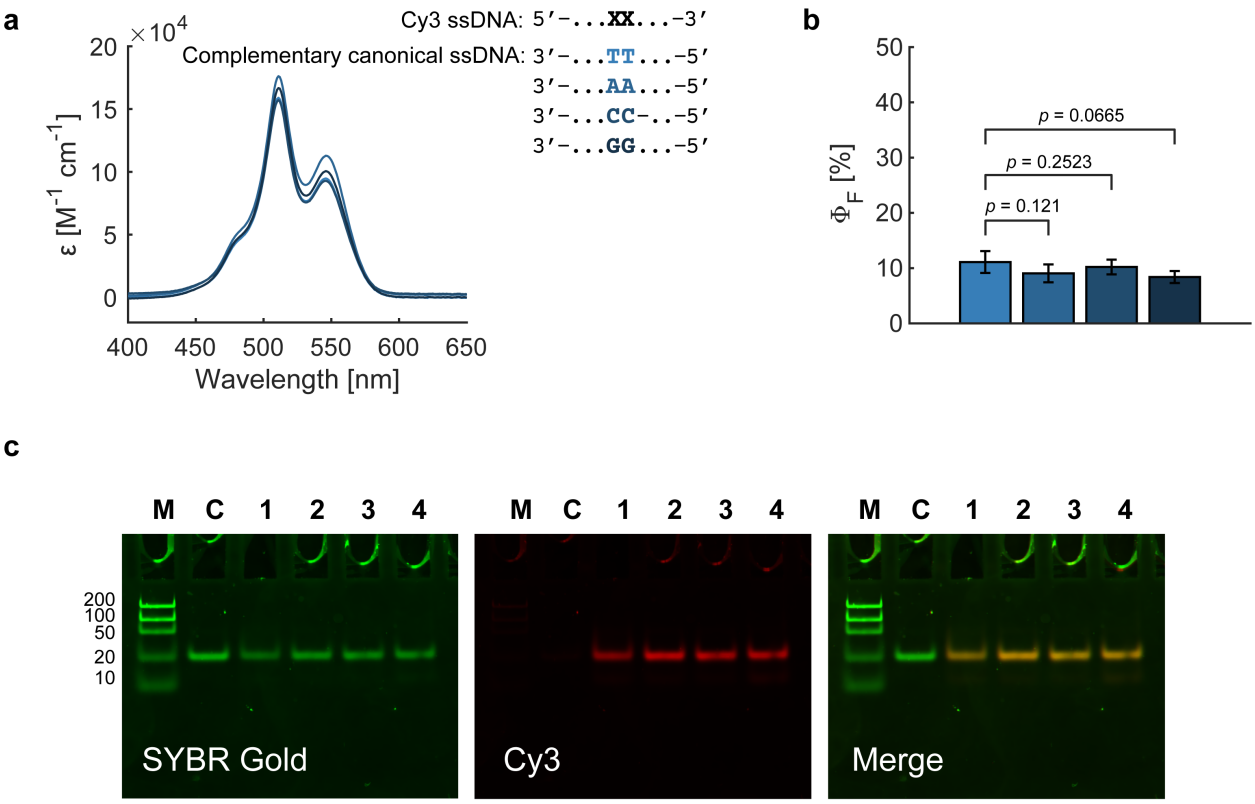


**Figure S7 | Dependence of Cy3 dimer quantum yield ($\Phi_F$) based on the complementary nucleotides on the complementary strand. (a)** Measured absorbance spectra in units of molar absorption coefficient ($M^{-1}$ $cm^{-1}$) in 40 mM Tris, 20 mM acetate, 2 mM EDTA, 12 mM $MgCl_2$. **(b)** $\Phi_F$ of Cy3 dimer in the presence of different complementary nucleotides. Two-sample t-test with unequal variance was used for significance testing. Quantum yields are plotted as mean $\pm$ s.d. values that were calculated from measurements of three independent replicates. [DNA] = 0.5 $\mu$M. **(c)** Native 12% PAGE gel. **M:** Thermo-Scientific FastRuler Ultra Low Range DNA Ladder, **C:** Cy3 dimer control + Cy3 dimer 2 TT, **1:** Cy3 dimer 1 + Cy3 dimer 2 TT DNA duplex, **2:** Cy3 dimer 1 + Cy3 dimer 2 AA DNA duplex, **3:** Cy3 dimer 1 + Cy3 dimer 2 CC DNA duplex, **4:** Cy3 dimer1 + Cy3 dimer 2 GG DNA duplex.

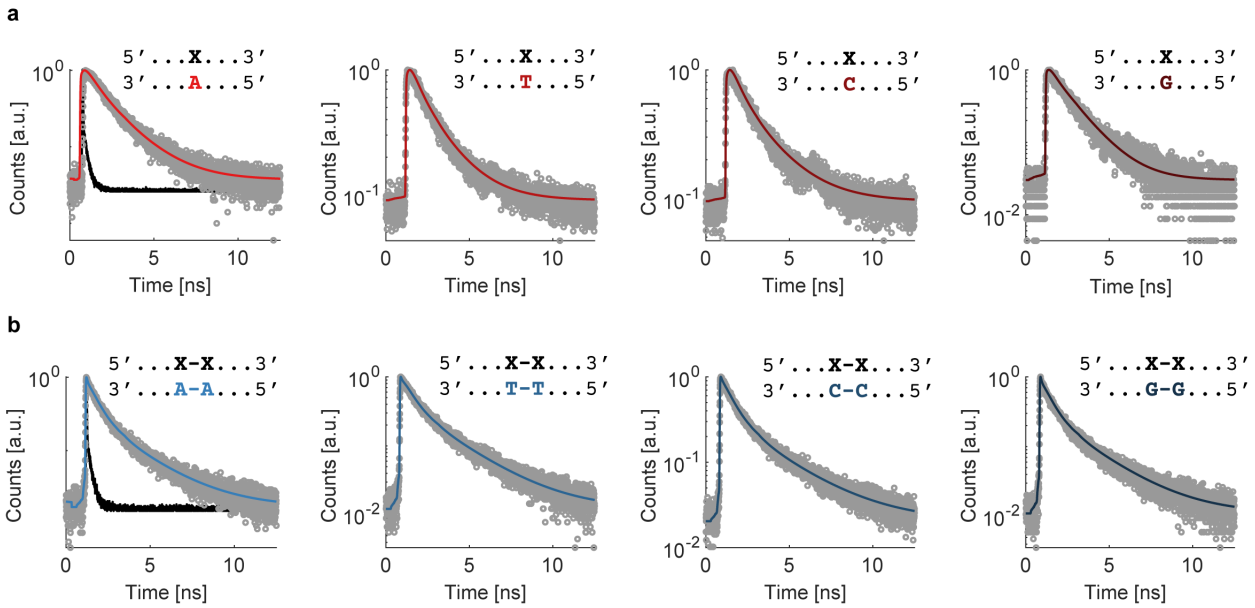


**Figure S8 | Sequence-dependence of Cy3 fluorescence decay traces. (a)** Cy3 monomer and **(b)** Cy3 dimer. Samples were excited at $\lambda_{ex}$=520 nm and fluorescence were collected at $\lambda_{em}$=560 nm. [DNA] = 1.0 $\mu$M in 40 mM Tris, 20 mM acetate, 2 mM EDTA, 12 mM $MgCl_2$. Fitted values are summarized in Table S6. Black traces in the leftmost panels of **a** and **b** are instrument response functions. Measurements were performed under all parallel excitation and emission conditions.

**Table S6** | Fitted fluorescence lifetime values of fluorescence decay traces in Figure S8.

| **Opposite nucleotide** | **Cy3 monomer** | | | **Cy3 dimer** | | | |
|---|---|---|---|---|---|---|---|
| | ($A_1$) $\tau_1$ [ns] | ($A_2$) $\tau_2$ [ns] | $\tau_{ave}$ [ns] | ($A_1$) $\tau_1$ [ns] | ($A_2$) $\tau_2$ [ns] | ($A_3$) $\tau_3$ [ns] | $\tau_{avg}$ [ns] |
| A | (0.49) 1.82 | (0.51) 0.62 | 1.2 | (0.13) 2.47 | (0.35) 0.54 | (0.52) 0.07 | 0.6 |
| T | (0.54) 1.73 | (0.46) 0.46 | 1.2 | (0.19) 2.55 | (0.38) 0.56 | (0.43) 0.07 | 0.7 |
| C | (0.51) 2.02 | (0.49) 0.51 | 1.4 | (0.17) 2.91 | (0.39) 0.62 | (0.44) 0.09 | 0.8 |
| G | (0.60) 1.44 | (0.40) 0.29 | 1.0 | (0.13) 2.47 | (0.34) 0.52 | (0.53) 0.07 | 0.5 |

* Fluorescence decay traces for Cy3 monomers and dimers were fitted with a multi-exponential decay function: $I(t) = \sum_i A_i \exp(-t/\tau_i)$ with the IRF through iterative reconvolution. $I(t)$ is the photon counts as a function of time $t$, $A_i$ is the fractional amplitude of component $i$, and $\tau_i$ is the fluorescence lifetime constant of component $i$. The average fluorescence lifetime $\tau_{avg}$ was calculated using amplitude-weighted averaging given by $\tau_{avg} = \sum_i A_i\tau_i / \sum_i A_i$. Fractional amplitudes are indicated in parentheses. [DNA] = 0.5 $\mu$M in 40 mM Tris, 20 mM acetate, 2 mM EDTA, 12 mM $MgCl_2$.

## S1.7 Fluorescence lifetimes of Cy3 dimers with varied nucleotide spacings on DNA duplexes

### S1.7.1 DNA sequences

**Table S7** | Single-stranded DNA sequences for nucleotide-spaced aggregates on DNA duplexes.

| Sequence identifier | ssDNA sequence (5' to 3' direction) |
|---|---|
| Cy3 dimer 1 nt (1) | TGCACTCTCG**X**T**X**TGACCGAGCT |
| Cy3 dimer 1 nt (2) | AGCTCGGTCATATCGAGAGTGCA |
| Cy3 dimer 2 nt (1) | TGCACTCTCG**X**TT**X**TGACCGAGCT |
| Cy3 dimer 2 nt (2) | AGCTCGGTCATAATCGAGAGTGCA |
| Cy3 dimer 3 nt (1) | TGCACTCTCG**X**TTT**X**TGACCGAGCT |
| Cy3 dimer 3 nt (2) | AGCTCGGTCATAAATCGAGAGTGCA |

* **X** denotes internal Cy3 modification

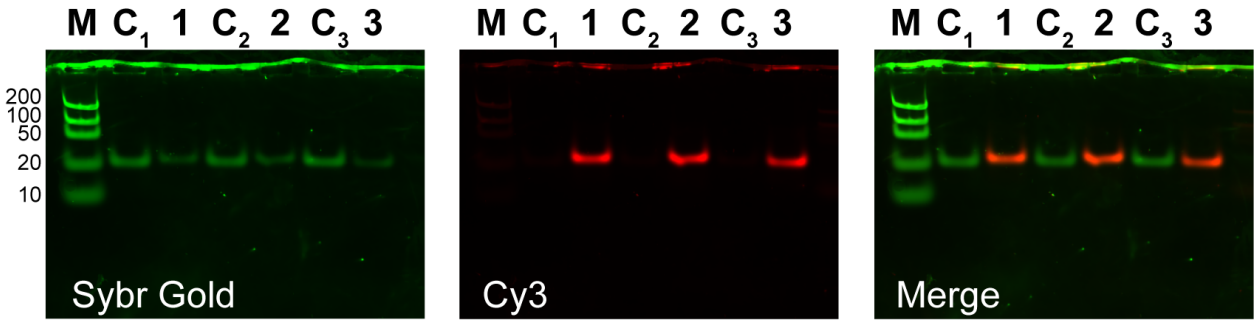


**Figure S9 | Native 12% PAGE analyses of nucleotide-spaced Cy3 dimers on DNA duplexes. M:** Thermo-Scientific FastRuler Ultra Low Range DNA Ladder, $\mathbf{C_1}$**:** canonical duplex control, **1:** one-nucleotide spaced Cy3 dimer, $\mathbf{C_2}$**:** canonical duplex control, **2:** two-nucleotide spaced Cy3 dimer, $\mathbf{C_3}$**:** canonical duplex control, **3:** three-nucleotide spaced Cy3 dimer. Canonical duplex controls have the same number of nucleotides and sequence as the Cy3-modified duplexes. However, Cy3 is instead replaced in DNA duplex controls with a deoxyadenosine to form DNA duplexes without mismatches.

### S1.7.2 Fluorescence lifetimes of nucleotide-spaced dimers

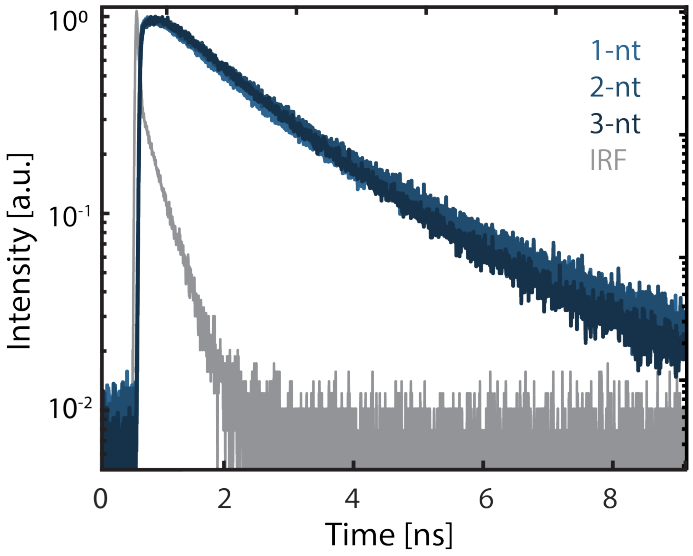


**Figure S10 | Time-resolved fluorescence lifetimes of Cy3 dimers with varied nucleotide spacings on DNA duplexes.** Normalized fluorescence decay curves of nucleotide-spaced Cy3 dimers.

**Table S8** | Fitted fluorescence lifetime values of fluorescence decay traces in Figure S10.

| **Cy3 dimer construct** | $(\boldsymbol{A_1})\ \boldsymbol{\tau_1}$ [ns] | $(\boldsymbol{A_2})\ \boldsymbol{\tau_2}$ [ns] | $(\boldsymbol{A_3})\ \boldsymbol{\tau_3}$ [ns] |
|---|---|---|---|
| 1-nt spaced Cy3 dimer | $(0.42 \pm 0.02)\ 0.07 \pm 0.03$ | $(0.39 \pm 0.02)\ 0.75 \pm 0.03$ | $(0.19 \pm 0.02)\ 2.19 \pm 0.05$ |
| 2-nt spaced Cy3 dimer | $(0.34 \pm 0.02)\ 0.08 \pm 0.02$ | $(0.39 \pm 0.02)\ 0.80 \pm 0.02$ | $(0.27 \pm 0.02)\ 2.07 \pm 0.05$ |
| 3-nt spaced Cy3 dimer | $(0.27 \pm 0.12)\ 0.12 \pm 0.02$ | $(0.50 \pm 0.02)\ 0.90 \pm 0.03$ | $(0.23 \pm 0.02)\ 2.01 \pm 0.04$ |

* Fluorescence decay traces for Cy3 monomers and dimers were fitted with a multi-exponential decay function: $I(t) = \sum_i A_i \exp(-t/\tau_i)$ with the IRF through iterative reconvolution. $I(t)$ is the photon counts as a function of time $t$, $A_i$ is the fractional amplitude of component $i$, and $\tau_i$ is the fluorescence lifetime constant of component $i$. Fractional amplitudes are indicated in parentheses. Error bars are standard deviations from three replicates. [DNA] = 0.5 $\mu$M in 40 mM Tris, 20 mM acetate, 2 mM EDTA, 12 mM $MgCl_2$.

## S1.8 Circular dichroism spectra of Cy3 linear aggregates and dimers with varied nucleotide spacing on DNA duplexes

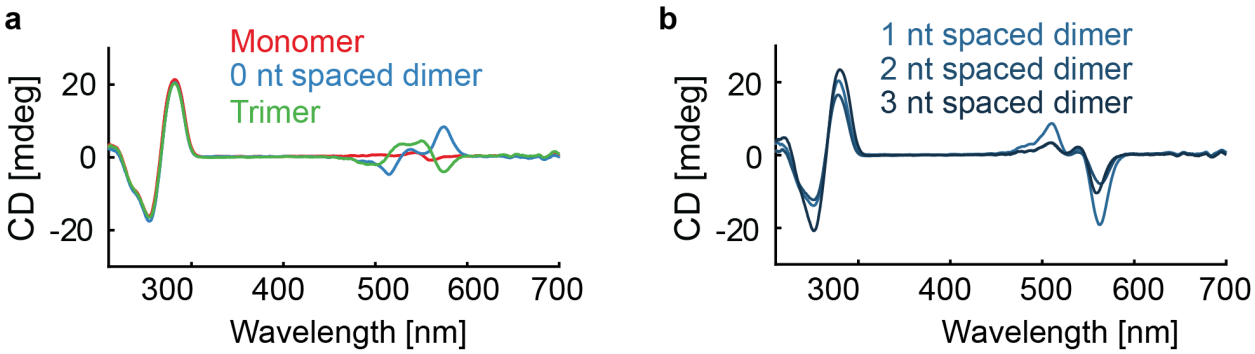


**Figure S11 | Circular dichroism spectra of Cy3 aggregates.** CD spectra of (**a**) linear constructs with increasing number of Cy3 whose schematic is shown in Figure1a and (**b**) linear Cy3 dimer constructs with intra-dimer spacing of 1–3 nucleotides whose schematic is shown in Figure2a.

# S2 Supplemental Data: Two-dimensional electronic spectroscopy

## S2.1 2DES pulse characterization

The pulses used for two-dimensional electronic spectroscopy were characterized using a transient grating frequency resolved optical gating experiment, as shown in Supplemental Figure S12.

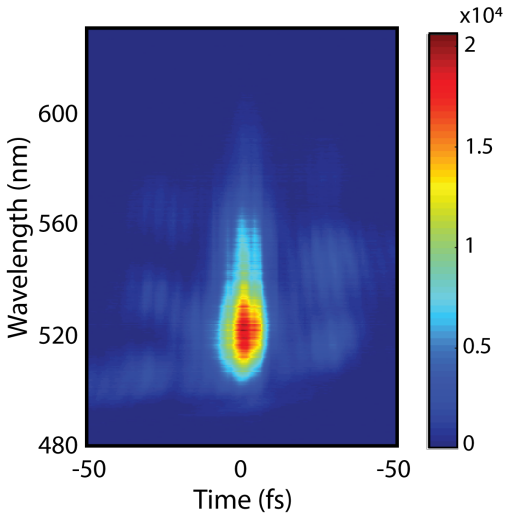


**Figure S12 | Pulse characterization.** Transient grating frequency resolved optical gating spectrum of pulse used in 2DES and homodyne transient grating measurements.

## S2.2 Coupling cross peak intensity analysis

The exact excitation and emission frequencies of the $\omega_{ex}$ = ∼18100 cm$^{-1}$ and $\omega_{em}$ = ∼19500 cm$^{-1}$ cross peak varied for each dimer construct. The excitation frequency was selected as the maximum of the $\omega_{ex}$ = ∼18100 cm$^{-1}$ and $\omega_{em}$ = ∼18100 cm$^{-1}$ diagonal peak and the emission frequency was selected as the maximum in the range of 19000 cm$^{-1}$ to 20000 cm$^{-1}$ (shown by arrows in Figure 2b). The cross-peak intensity was then scaled by dividing by the intensity of the $\omega_{ex}$ = ∼18100 cm$^{-1}$ and $\omega_{em}$ = ∼18100 cm$^{-1}$ diagonal peak. Error bars shown in Figure 2 are the standard deviation of three replicates. Slices along the diagonal peak and cross peak are shown in Figure S13.

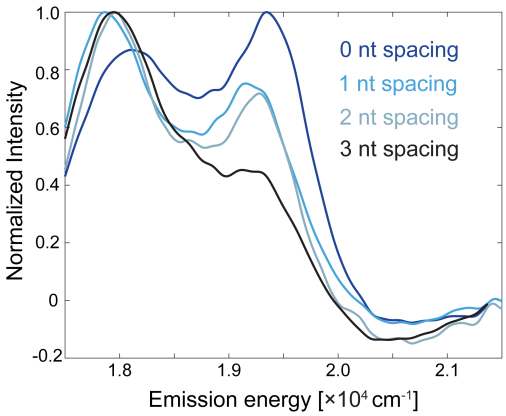


**Figure S13 | Signatures of electronic coupling. (a)** Coupling crosspeaks for coupled Cy3 dimers. Lower energy peak is along the diagonal, higher energy peak is the crosspeak. **(b)** Intensity of lower energy cross peak ($\omega_{ex}$ = 19500 cm$^{-1}$ /$\omega_{em}$ = 18100 cm$^{-1}$) for coupled dimers and monomers (scaled by 18100 cm$^{-1}$ diagonal peak intensity).

## S2.3 Cy3 monomer-DNA construct sequences

**Table S9** | Single-stranded DNA sequences for Cy3 monomers on DNA duplexes and DX tiles.

| Sequence identifier | ssDNA sequence (5' to 3' direction) |
|---|---|
| Duplex 1 | TGCACTCTCG**X**TGACCGAGCT |
| Duplex 2 | AGCTCGGTCATCGAGAGTGCA |
| DX tile 1 | CTGAAGTGACCGAGAAGCTCG |
| | GTCATCGAGAGTGCAGGGGCT |
| | CGAATCCGGG |
| DX tile 2 | TAGGGCGTGGGGGTCACTTCAG |
| DX tile 3 | TCGCCTGGGCTCTCG**X**TGAC |
| DX tile 4 | ACGCTGAACTTGAGGCCCGAAG |
| | CCCAGGCGAGAGCGTCCAGCCC |
| | ACGCCCTA |
| DX tile 5 | CCCGGATTCGAAAGTTCAGCGT |
| DX tile 6 | TTCGGGCCTCGCCCCTGCAC |
| DX tile 7 | CTGGACGCTCCGAGCTTCTC |

* **X** denotes internal Cy3 modification

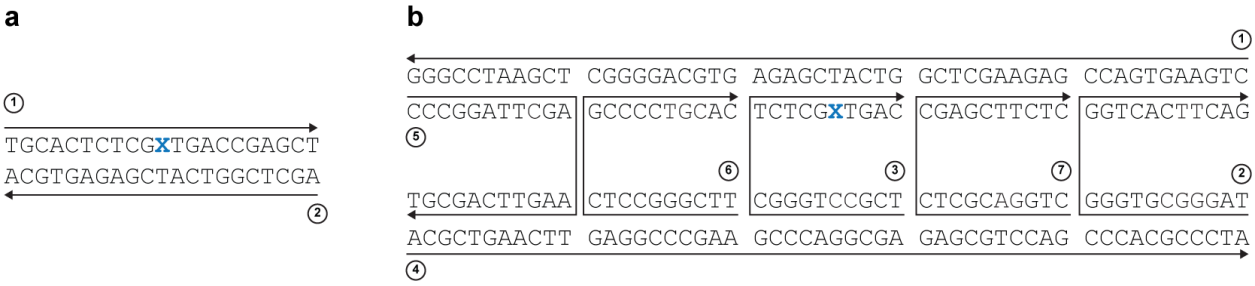


**Figure S14** | **Schematic of Cy3-modified DNA constructs used for 2DES measurements. (a)** duplex. **(b)** DX tile.

## S2.4 Comparison of steady-state photophysics of Cy3 monomer-DNA constructs used for CLS analyses

**Table S10** | Quantum yield comparison of different Cy3 monomer-DNA constructs used in CLS analyses.

| Construct identifier | Sequence list | Quantum yield [%] |
|---|---|---|
| Cy3 monomer at the middle of DNA duplex | Table S9 | $25.4 \pm 1.6$ ($n = 12$) |
| Cy3 monomer at the middle of DX tile | Table S9 | $24.4 \pm 2.7$ ($n = 11$) |

* Error bars are standard deviations. $n$ is the number of independent replicates measured.

## S2.5 Description of the centerline slope analysis

Centerline slope analysis (CLS) of a particular transition in the 2D spectrum reports on how that electronic or vibronic transition is coupled to the surrounding bath environment. This is performed by finding the forward-time centerline (FCL) by taking the derivative of the spectrum ($S$) with respect to the emission frequency,

$$\left.\frac{\partial S(\omega_{\mathrm{em}}, T, \omega_{\mathrm{ex}})}{\partial \omega_{\mathrm{em}}}\right|_{\omega_{\mathrm{em}}=\omega_{\mathrm{FCL}}} = 0 \tag{4}$$

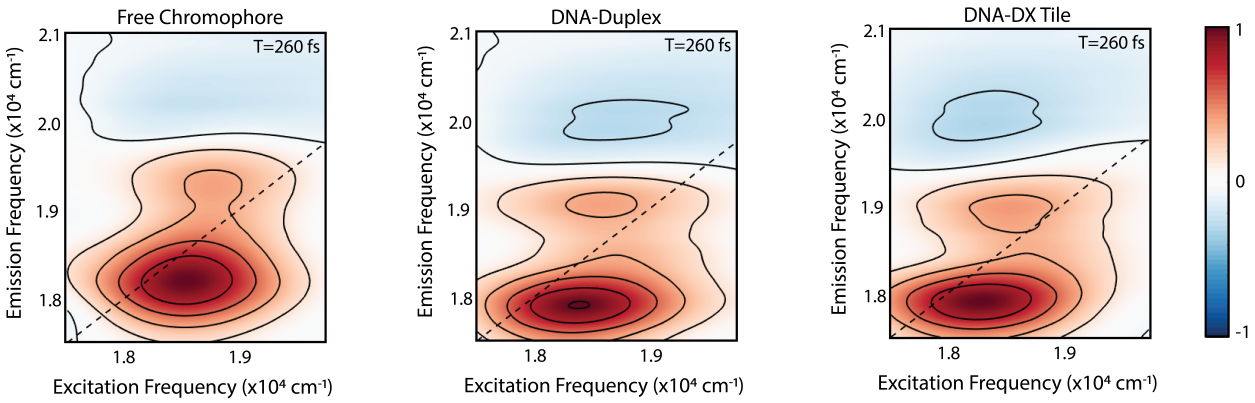


**Figure S15 | Cy3 monomer 2D spectra.** Representative spectra of the Cy3 monomer free in solution and scaffolded to a DNA duplex and DX tile.

and then plotting the ratio of the excitation to FCL emission frequency, which corresponds to the normalized frequency-frequency correlation function.

$$\frac{\omega_{\text{FCL}}}{\omega_{\text{ex}}} = \frac{\left\langle \delta\omega_{eg}(t)\delta\omega_{eg}(0)\right\rangle}{\left\langle \delta\omega_{eg}(0)\delta\omega_{eg}(0)\right\rangle} \tag{5}$$

The decay of this function corresponds to the loss over correlation between the excitation and emission frequencies owing to spectral diffusion over the population time, $T$, and is frequently modeled as a Brownian oscillator to include both overdamped and underdamped modes. Here we observe a short sub-50 fs component and a longer picosecond component corresponding to timescales of solvation and charge redistribution after photoexcitation. [4, 5]

Representative 2D spectra are shown in Figure S15. Figure S16a shows the ratio of the lower diagonal peak ($\omega_{\text{ex}}$ = 18050 cm$^{-1}$ /$\omega_{\text{em}}$ = 18050 cm$^{-1}$) and the upper cross peak ($\omega_{\text{ex}}$ = 18050 cm$^{-1}$ /$\omega_{\text{em}}$ = 19400 cm$^{-1}$) for the free chromophore, highlighting how the ratio between these peaks remains constant over time. The spectra were phased according to the projection slice theorem [6]. Figure S16b shows the projected 2D spectrum for the free chromophore at a waiting time of 260 fs as well as the pump-probe spectrum. Here the centerline slope was fit centered at 18250 cm$^{-1}$ for the monomer in DNA and 18050 cm$^{-1}$ for the free chromophore. The spectrum and center line slope of the free chromophore at a waiting time of 2 ps is shown in Figure S16c highlighting the non-zero center line slope at longer time delays, which reflects the contribution of static disorder and may arise from the subpopulations observed through the multiple components of the fluorescence lifetime d ecays. The residual exponential dynamics arising from overdamped modes in the spectral density were subtracted prior to Fourier transform of the CLS data to generate Main Text Figure 3d. The fit parameters required to do so are shown in Table S11 below.

To further investigate the electronic-vibrational coupling, homodyne transient grating experiments were performed to identify signatures of vibrational wavepackets in the three monomeric DNA environments. Figure S17a shows the power spectrum of short-time population subtracted transient grating data (under 500 fs). The peak frequencies correspond to the frequency of vibrational wavepackets on the ground and excited state potential energy surfaces. We find that by simulating the transient grating frequency components between 250 cm$^{-1}$ and 750 cm$^{-1}$ with a 60 fs dephasing time, we recover a broad peak centered at 410 cm$^{-1}$ (Figure S17b). This suggests that the broad feature recovered in Main Text Figure 3d at 450 cm$^{-1}$ could be a result from a superposition of these vibrational modes (components shown in Table S12). The residual CLS oscillations giving rise to Figure 3c are shown in Figure S17c. Data are the average of two replicates. Error bars are the variation between replicates for each sample type.

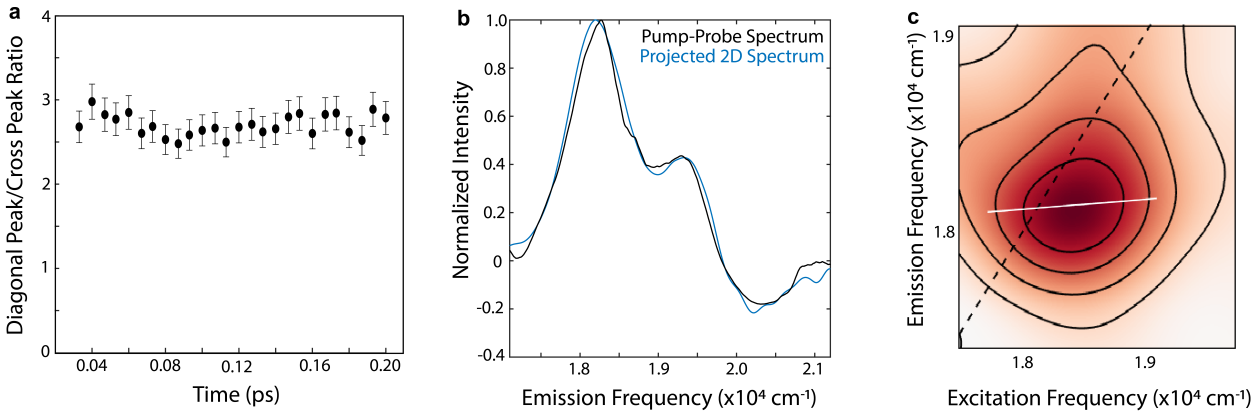


**Figure S16 | Cy3 monomer centerline slope methodology. (a)** Ratio of 18050 $cm^{-1}$ diagonal peak to excitation frequencies $\omega_{ex}$ = 18050 and 19400 $cm^{-1}$ cross peak as a function of waiting time for the Cy3 free chromophore. **(b)** Pump-probe spectrum and projection of 2D spectrum for $T$ = 260 fs for the free chromophore. **(c)** 2D spectra of the free chromophore for a waiting time 2 ps showing the persistence of non-zero a centerline slope.

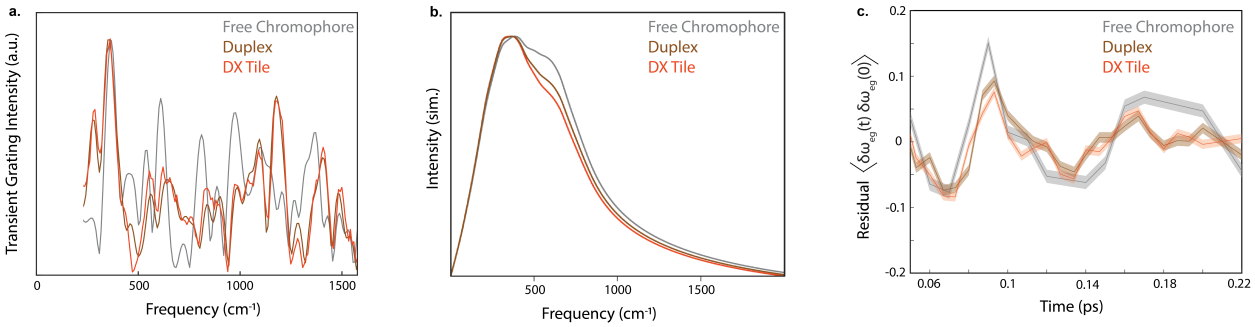


**Figure S17 | Coupling to discrete normal modes in frequency-frequency correlation function** (**a**) Homodyne transient grating spectra at and emission frequency of $\omega_{em}$ = 18050 $cm^{-1}$. (**b**) Simulated data comparing the frequency-frequency correlation function to model of vibrational modes between 350 and 650 $cm^{-1}$ (comparable to Figure 3d).(**c**) Exponential subtracted residual oscillations from the data in Figure 3c.

**Table S11** | Parameters for CLS analysis residual subtraction.

| **Construct** | **Fit Parameters** |
|---|---|
| Free chromophore | $\tau_1 = 22$ fs $A_1 = 0.89$ $\tau_2 = 2.54$ ps $A_2 = 0.11$ |
| Duplex monomer | $\tau_1 = 17$ fs $A_1 = 0.92$ $\tau_2 = 1.27$ ps $A_2 = 0.08$ |
| DX Tile monomer | $\tau_1 = 18$ fs $A_1 = 0.91$ $\tau_2 = 0.98$ ps $A_2 = 0.09$ |

**Table S12** | Parameters for CLS underdamped frequency model.

| **Mode Frequency** | **Weighted Amplitude** |
|---|---|
| 375 $cm^{-1}$ | $A_{\text{chromophore}} = 0.46$ $A_{\text{duplex}} = 0.51$ $A_{\text{DX tile}} = 0.49$ |
| 550 $cm^{-1}$ | $A_{\text{chromophore}} = 0.26$ $A_{\text{duplex}} = 0.27$ $A_{\text{DX tile}} = 0.28$ |
| 612 $cm^{-1}$ | $A_{\text{chromophore}} = 0.28$ $A_{\text{duplex}} = 0.22$ $A_{\text{DX tile}} = 0.23$ |

# S3 Supplemental Data: Fluorescence spectroscopy for energy transfer characterization

## S3.1 DNA sequences of constructs used for FRET experiments

**Table S13** | Single-stranded DNA sequences for FRET experiments involving duplex scaffolds.

| Sequence identifier | ssDNA sequence (5' to 3' direction) |
|---|---|
| FRET monomer duplex 1 | TAGGGCGTGGGGGTCAC**X**TCAG |
| FRET monomer duplex 2 + Cy5 | /Cy5/TCTGAAGTGACCCCCACGCCCTA/Biotin/ |
| FRET dimer duplex 1 | TAGGGCGTGGGGGTCAC**XX**CAG |
| FRET dimer duplex 2 + Cy5 | /Cy5/TCTGAAGTGACCCCCACGCCCTA/Biotin/ |

* **X** denotes internal Cy3 modification

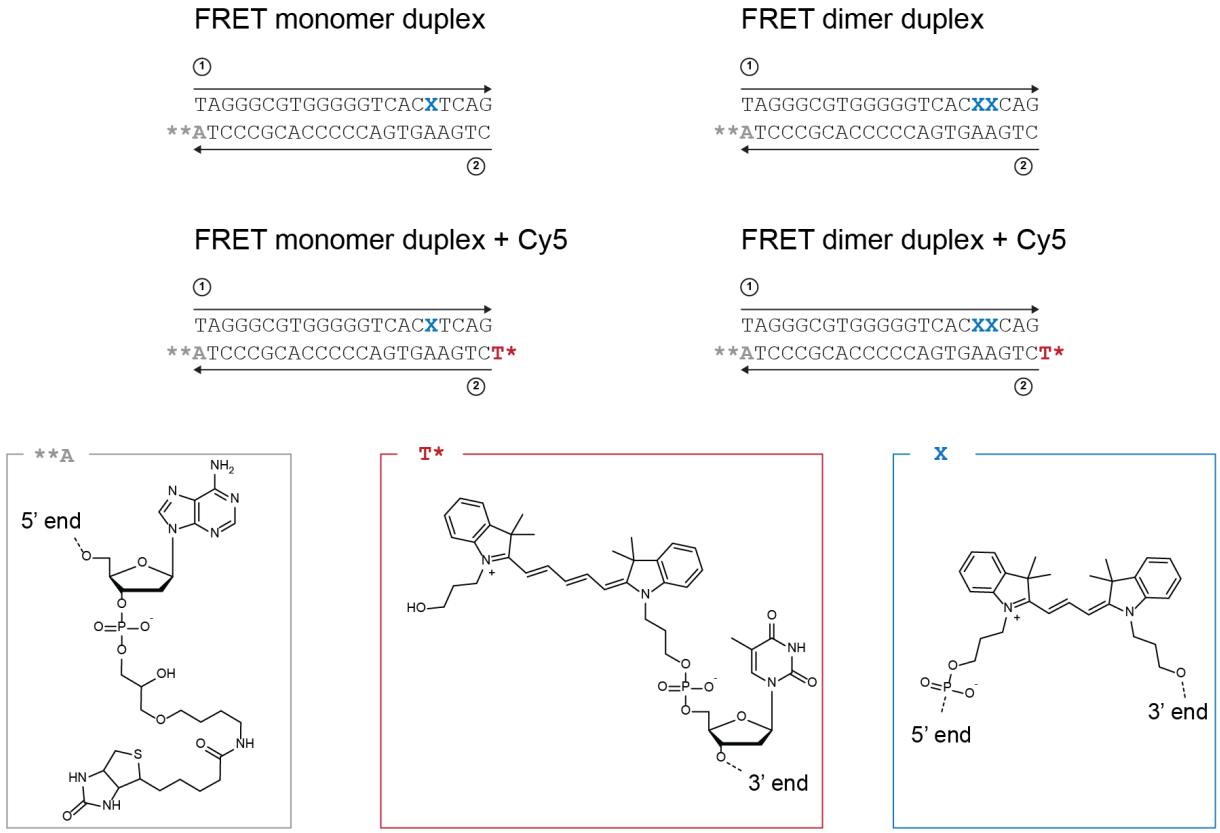


**Figure S18** | **Schematic of Cy3-modified DNA duplex constructs used for all FRET measurements.** **(a)** DNA duplex. **(b)** DX tile.

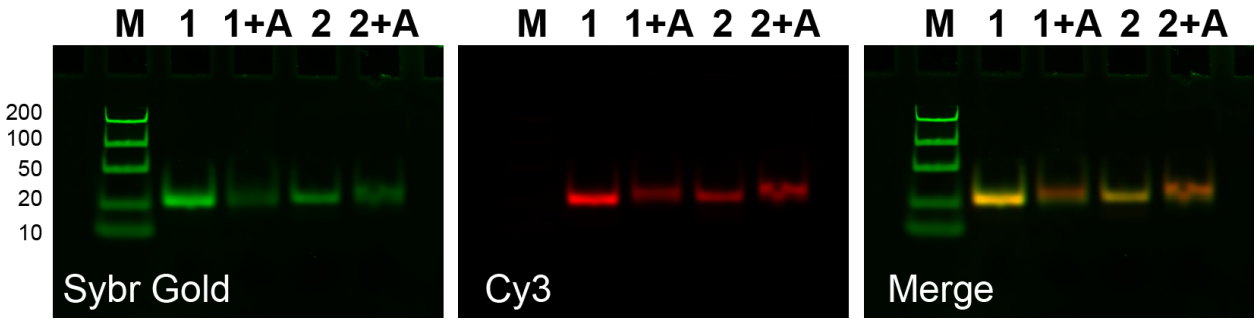


**Figure S19 | Native 12% PAGE analyses of purified Cy3 monomers and dimers on DNA duplexes with or without Cy5. M:** Thermo-Scientific FastRuler Ultra Low Range DNA Ladder, **1:** Cy3 monomer on DNA duplex without Cy5, **1+A:** Cy3 monomer on DNA duplex with Cy5, **2:** Cy3 dimer on DNA duplex without Cy5, **2+A:** Cy3 dimer on DNA duplex with Cy5.

**Table S14** | Single-stranded DNA sequences FRET experiments involving DX tile scaffolds.

| **Sequence identifier** | **ssDNA sequence (5' to 3' direction)** |
|---|---|
| DX FRET Cy5 1 | /Cy5/TCTGAAGTGACCGAGAAGCGGCGGGA AGTATCGTGAAGGGGCTCGAATCCG GG |
| DX monomer FRET 2 | TAGGGCGTGGGGGTCAC**X**TCAG |
| DX dimer FRET 2 | TAGGGCGTGGGGGTCAC**XX**CAG |
| DX FRET 3 | TCGCCTGGGCGATACTTCCC |
| DX FRET 4 | /Biotin/ACGCTGAACTTGAGGCCCGAAGCCC AGGCGAGAGCGTCCAGCCCACGCCC TA |
| DX FRET 5 | CCCGGATTCGAAAGTTCAGCGT |
| DX FRET 6 | TTCGGGCCTCGCCCCTTCAC |
| DX FRET 7 | CTGGACGCTCGCCGCTTCTC |

* **X** denotes internal Cy3 modification

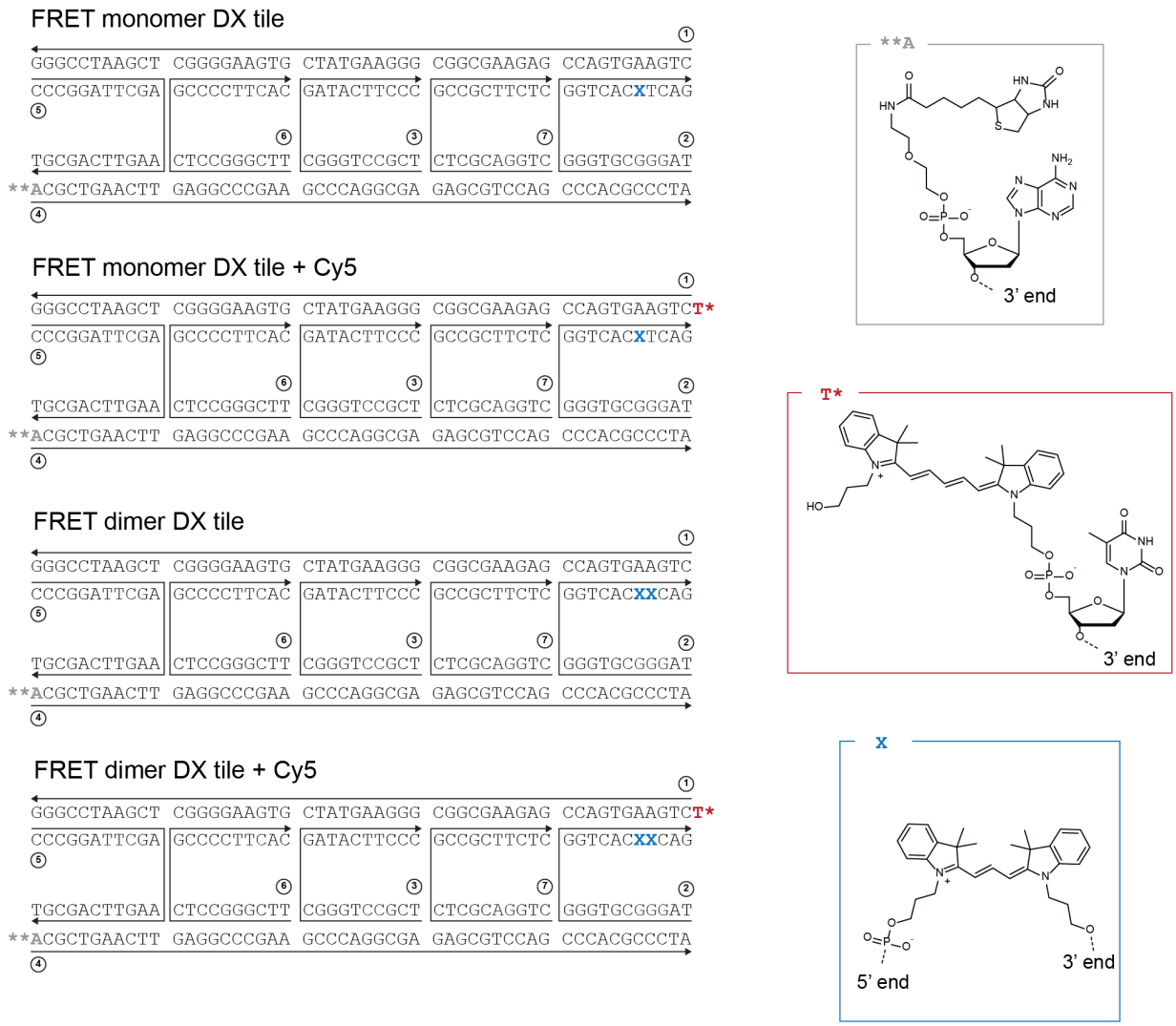


**Figure S20 | Schematic of Cy3-modified DNA DX tile constructs used for all FRET measurements.** **(a)** DNA duplex. **(b)** DX tile.

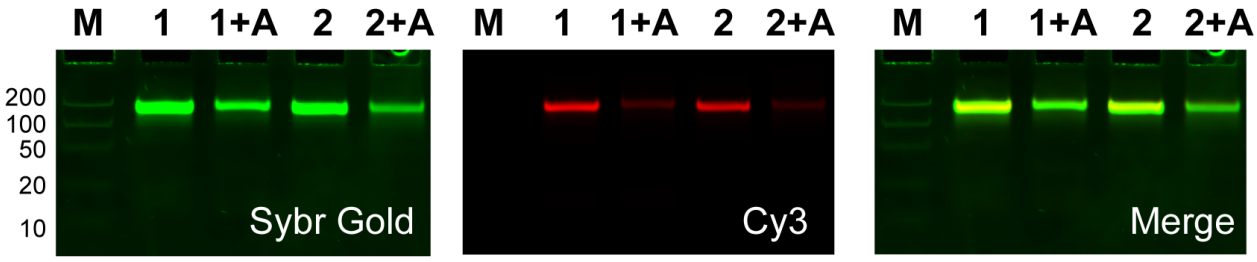


**Figure S21 | Native 10% PAGE analyses of purified Cy3 monomers and dimers in DX tiles with or without Cy5.** **M:** Thermo-Scientific FastRuler Ultra Low Range DNA Ladder, **1:** Cy3 monomer in DX tile without Cy5, **1+A:** Cy3 monomer in DX tile with Cy5, **2:** Cy3 dimer in DX tile without Cy5, **2+A:** Cy3 dimer in DX tile with Cy5.

## S3.2 Comparison of steady-state photophysics of Cy3-modified DNA duplexes and DX tiles without Cy5 acceptor

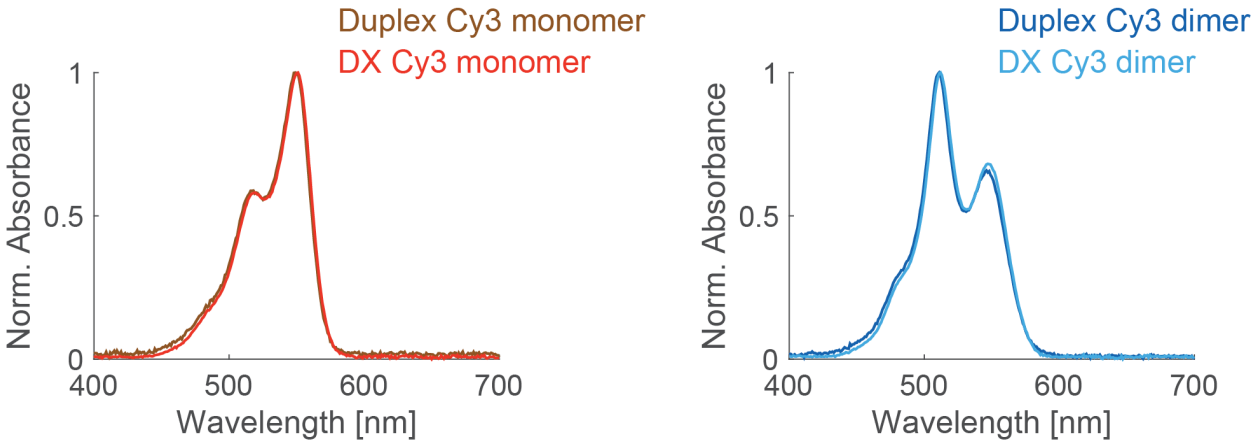


**Figure S22 | Comparison of steady-state absorbance spectra of Cy3-modified DNA duplexes and DX tiles.** Normalized absorbance spectra of Cy3 monomers (left) and Cy3 dimers (right) on DNA duplexes and DX tiles without Cy5.

**Table S15** | Quantum yield comparison of different Cy3-modified DNA constructs used in FRET experiments.

| Construct identifier | Sequence list | Quantum yield [%] |
|---|---|---|
| Cy3 monomer near the 3'-end of DNA duplex | Table S13 | $25.9 \pm 3.2$ ($n = 3$) |
| Cy3 dimer near the 3'-end of DNA duplex | Table S13 | $8.8 \pm 1.5$ ($n = 8$) |
| Cy3 monomer near the 3'-end of DX tile | Table S14 | $24.2 \pm 1.9$ ($n = 6$) |
| Cy3 dimer near the 3'-end of DX tile | Table S14 | $8.4 \pm 1.0$ ($n = 12$) |

* All constructs do not contain Cy5. Error bars are standard deviations. $n$ is the number of independent replicates measured.

## S3.3 Measurement of FRET efficiency of Cy3 monomer/dimer to Cy5 on DNA duplexes using steady-state fluorescence quenching

The emission spectra of the Cy3 donor and Cy5 acceptor from a FRET system can be decomposed similar to spectral decomposition method used in Supplemental Information Section S1.4.2.[7] For a mixture of multiple emitting components, the total/sum spectra, $S_{\text{em}}$, is given by a linear combination of individual constituent spectra:

$$S_{\text{em}} = \alpha_{1,\text{em}}\mathbf{X}_{1,\text{em}} + \alpha_{2,\text{em}}\mathbf{X}_{2,\text{em}} + \ldots + \alpha_{n,\text{em}}\mathbf{X}_{n,\text{em}} \tag{6}$$

where $\alpha_{n,\text{em}}$ is the fractional contribution of each component emission spectra $\mathbf{X}_{n,\text{em}}$. If each component emission spectra $X_{n,\text{em}}$ is known, then the contribution factors $\alpha_{n,\text{em}}$ can be solved. We then used non-negative least square fitting to calculate the component emission spectra for Cy3 monomer or dimer on DNA duplexes or DX tiles, and Cy5. The results of the fits and the decomposed Cy3 and Cy5 spectra are shown in Supplemental Information Figure S23.

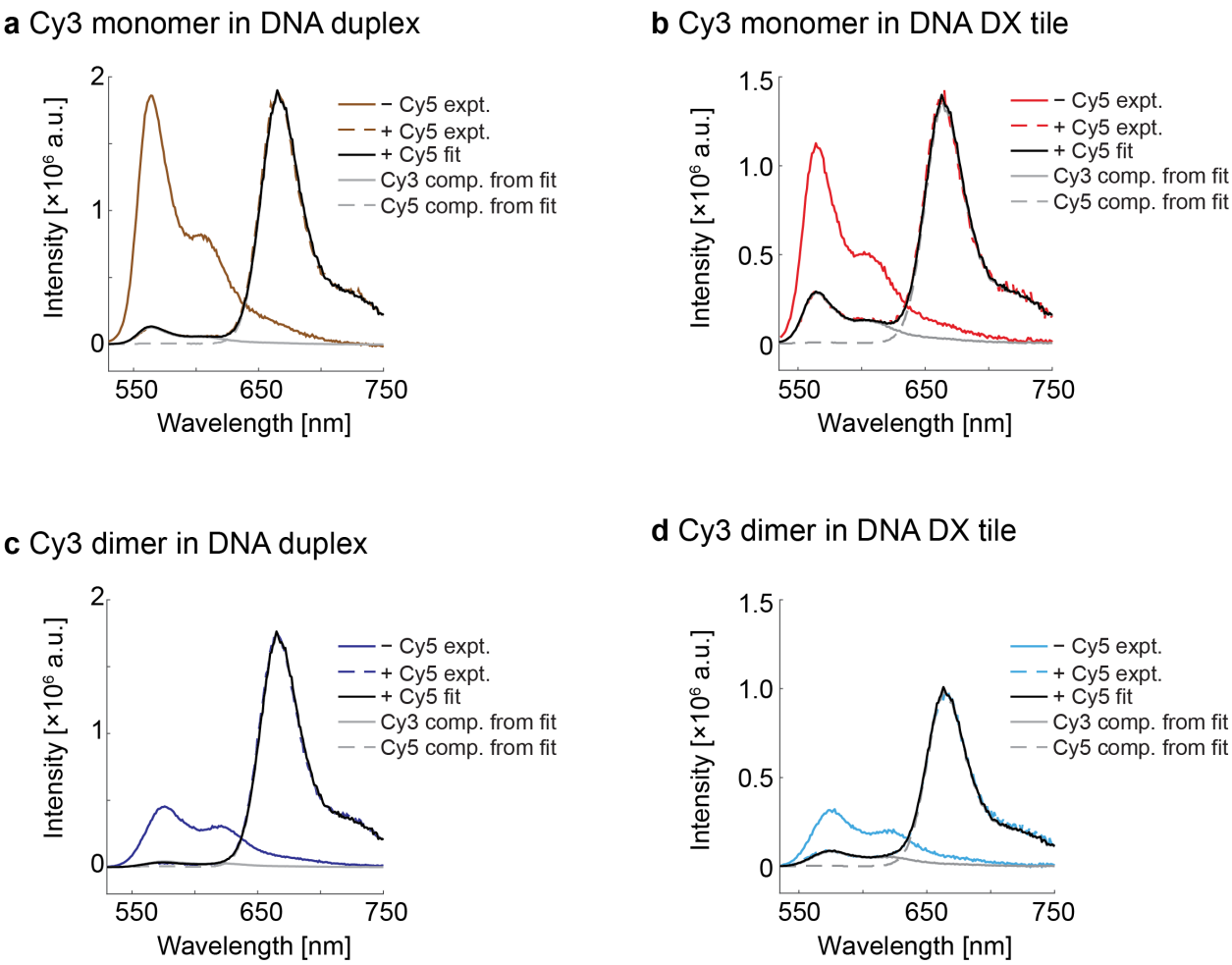


**Figure S23 | Fluorescence spectra of Cy3-modified duplexes and DX tiles with or without Cy5.** Absorption factor-corrected fluorescence spectra of Cy3 monomer in duplexes (**a**) or DX tiles (**b**) and Cy3 dimer in duplexes (**c**) or DX tiles (**d**) with or without Cy5 acceptor. All spectra are corrected using the absorption factor at the excitation wavelength $\lambda_{exc}$ = 525 nm. Absorption factor is defined as $1 - 10^{-\text{Absorbance}}$.

## S3.4 Comparison of time-resolved photophysics of Cy3-modified DNA duplexes and DX tiles without Cy5 acceptor

Fluorescence decay curves of monomer constructs were fitted using the least-squares method with the convolution of the instrument response function (IRF) and a biexponential function (Eq. 7). Cy3 dimer constructs were fitted with the convolution of the instrument response function (IRF) and a triexponential function (Eq. 8). Resultant parameters of the fit are presented in Table S16 for Cy3 monomer constructs and in Table S17 for Cy3 dimer constructs.

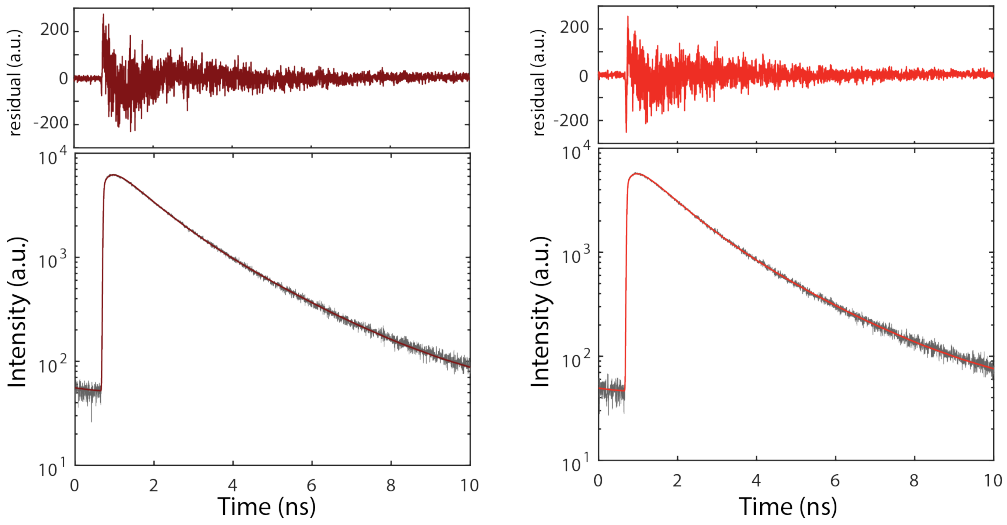


**Figure S24 | Comparison of time-resolved fluorescence decay of Cy3 monomer constructs.** Normalized magic angle fluorescence decay curves of duplex-scaffolded Cy3 monomer (left, bottom) and associated residual (left, top), and of DX tile-scaffolded Cy3 monomer (right, bottom) and associated residual (right, top). Gray traces are raw data and solid lines are the respective results of least-squares fitting using Eq. 7. Parameters of fits are presented in Table S16.

$$I(t) = A_0 + \mathrm{IRF} \otimes \sum_{i=1}^{2} A_i \exp\left(-t/\tau_i\right) \tag{7}$$

**Table S16** | Fitting results of time-resolved lifetime measurements of Cy3 monomer duplex and DX tile constructs using Eq. 7.

| | $A_0$ | $A_1$ | $\tau_1$ [ns] | $A_2$ | $\tau_2$ [ns] |
|---|---|---|---|---|---|
| Duplex | $2 \pm 5$ | $0.53 \pm 0.03$ | $0.73 \pm 0.03$ | $0.47 \pm 0.03$ | $2.00 \pm 0.06$ |
| DX tile | $2 \pm 6$ | $0.56 \pm 0.02$ | $0.77 \pm 0.02$ | $0.44 \pm 0.02$ | $1.97 \pm 0.02$ |

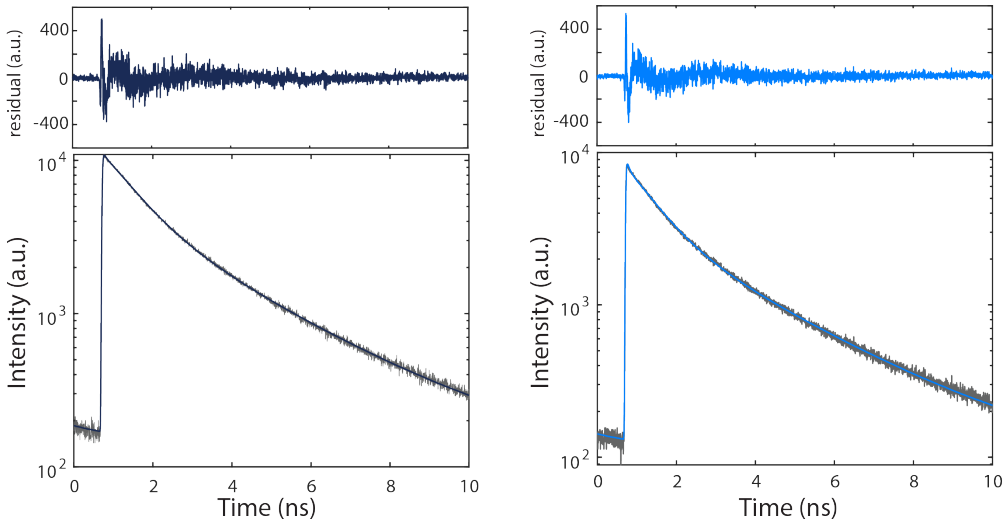


**Figure S25 | Comparison of time-resolved fluorescence decay of Cy3 dimer constructs.** Normalized magic angle fluorescence decay curves of duplex-scaffolded Cy3 dimer (left, bottom) and associated residual (left, top), and of DX tile-scaffolded Cy3 dimer (right, bottom) and associated residual (right, top). Gray traces are raw data and solid lines are the respective results of least-squares fitting using Eq. 8. Parameters of fits are presented in Table S17.

$$I(t) = A_0 + \mathrm{IRF} \otimes \sum_{i=1}^{3} A_i \exp\left(-t/\tau_i\right) \tag{8}$$

**Table S17** | Fitting results of time-resolved lifetime measurements of Cy3 dimer duplex and DX tile constructs using Eq. 8.

| | $A_0$ | $A_1$ | $\tau_1$ [ns] | $A_2$ | $\tau_2$ [ns] | $A_3$ | $\tau_3$ [ns] |
|---|---|---|---|---|---|---|---|
| Duplex | $33 \pm 29$ | $0.50 \pm 0.03$ | $0.10 \pm 0.01$ | $0.30 \pm 0.01$ | $0.91 \pm 0.07$ | $0.20 \pm 0.04$ | $3.26 \pm 0.15$ |
| DX tile | $27 \pm 25$ | $0.54 \pm 0.05$ | $0.10 \pm 0.01$ | $0.29 \pm 0.02$ | $0.85 \pm 0.09$ | $0.17 \pm 0.03$ | $3.17 \pm 0.19$ |

## S3.5 Time-resolved fluorescence anisotropy measurements of Cy3 monomer constructs and of Cy5 in the absence of Cy3

Fluorescence anisotropy decays were determined by exciting samples with vertically polarized 520 nm light and consecutively collecting vertically and horizontally polarized emission using the filter set described in the Methods section of the Main Text. The rising edge of the two decay curves were overlayed and the anisotropy curve was produced using Eq. 2 and fit using Eq. 3. The results of the fit of duplex- and DX tile-scaffolded monomer constructs and terminally-labelled Cy5 constructs are presented in Table S18.

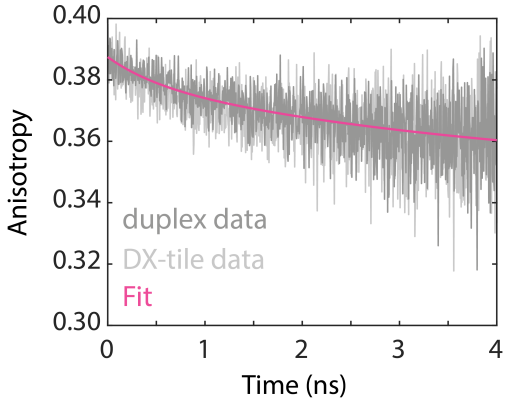


**Figure S26** | Anisotropy data for Cy5 terminally attached to Duplex and DX-tile constructs (sequences in Tables S13 and S14). Fit to the duplex-Cy5 data is shown in pink. Parameters are given in Table S18. The two constructs exhibit indistinguishable rotational properties for the attached Cy5.

The half-cone describing the limit of fluorescence depolarization is calculated from a multiexponential fluorescence anisotropy decay following the method from Ref. [8]:

$$\frac{r(t)}{r(0)} = Ae^{-t/\tau_1} + (1-A)e^{-t/\tau_2} \tag{9}$$

$$= (1-S^2)e^{-t/\tau_1} + S^2 e^{-t/\tau_2} \tag{10}$$

where

$$S^2 = \left[\frac{1}{2}\cos\theta(1+\cos\theta)\right]^2 \tag{11}$$

**Table S18** | Fluorescence anisotropy fits for duplex- and DX tile-scaffolded Cy3 monomers in the absence of Cy5 and for Cy5 in the absence of Cy3 using Eq. 2.

| | $r_0$ | $r_\infty$ | $A$ | $\tau_1$ [ns] | $\tau_2$ [ns] |
|---|---|---|---|---|---|
| Duplex | 0.40 (±0.01) | 0.34 (±0.01) | 0.10 (±0.02) | 0.19 (±0.15) | 3.45 (±0.94) |
| DX Tile | 0.40 (±0.09) | 0.33 (±0.03) | 0.20 (±0.09) | 0.62 (±0.14) | 22.97 (±16.22) |
| Cy5 | 0.39 (±0.01) | 0.34 (±0.01) | 0.23 (±0.02) | 0.59 (±0.35) | 7.86 (±7.98) |

Using the amplitude parameters ($A$) in S18, the limiting half-cone of duplex ($\theta_{\mathrm{duplex}}$) and DX tile ($\theta_{\mathrm{DX}}$) monomers with respect to the axis of rotation, i.e., axis normal to the DNA backbone (see Fig. 5 for a schematic diagram), were calculated to be $\theta_{\mathrm{duplex}} = 16° \pm 2°$ and $\theta_{\mathrm{DX}} = 22° \pm 6°$ (mean ± s.d., $n$ = 3 independent replicates), respectively.

## S3.6 Monte Carlo Modeling of FRET transfer in DNA Origami

The Cy3 to Cy5 FRET efficiency as calculated for static and dynamic averaging using both Gaussian and molecular dynamics derived angle distributions is shown in Table S19.

**Table S19** | Summary of predicted FRET efficiencies for different models considered.

| Construct | Gaussian Static Avg. | Gaussian Dynamic Avg. | MD Static Avg. | MD Dynamic Avg. |
|---|---|---|---|---|
| Duplex | 98% | 98% | 83% | 99% |
| DX Tile | 97% | 97% | 86% | 98% |

# S4 Supplemental Data: Single-molecule fluorescence spectroscopy

## S4.1 Single-molecule traces and analysis

The fluorescence photons from single DNA-dye constructs were recorded until photobleaching. The time-tagged fluorescence photons were binned into 10 ms bins and different intensity levels were determined via change-point analysis[9]. Representative intensity traces for monomeric Cy3 on duplexes and DX tiles are shown in Figure S27A and B, respectively, and for dimeric Cy3 on duplexes and DX tiles are shown in Figure S28A and B, respectively.

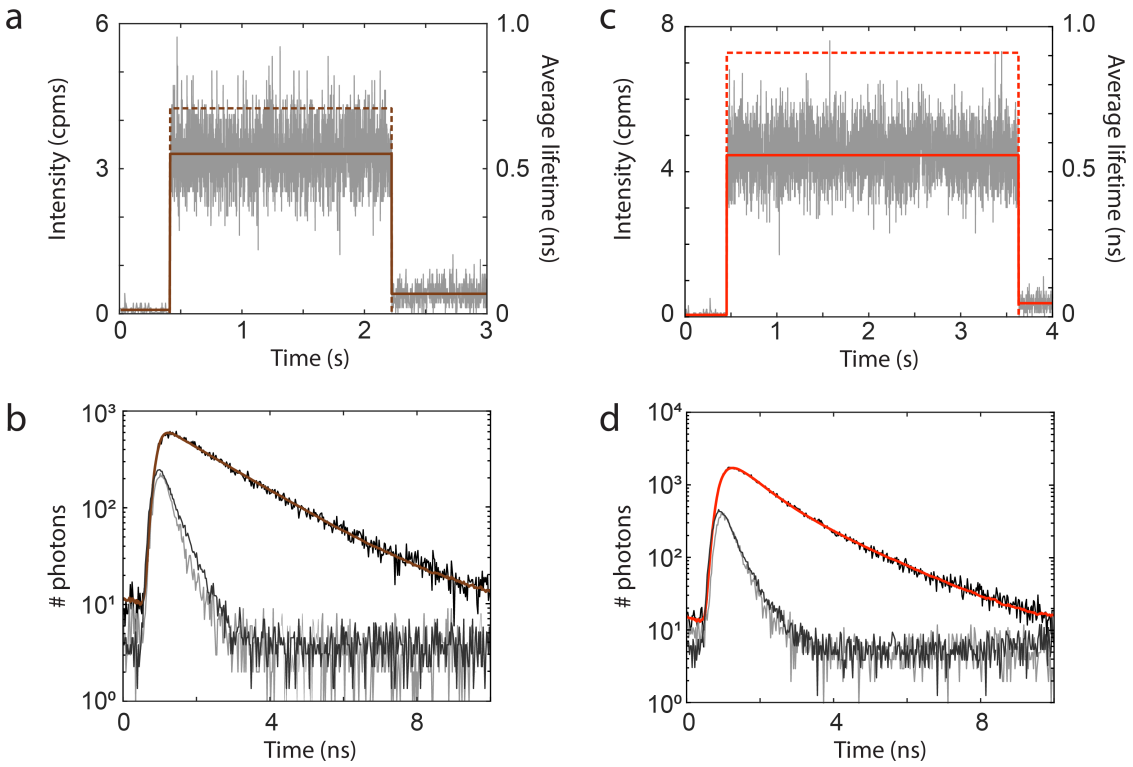


**Figure S27 | Representative single-molecule data for Cy3 monomer constructs.** (**a**) Time trace (gray) measured from a single Cy3 monomer scaffolded by duplex at the high FRET (HF) position. The number of photons binned at 10 ms is indicated in counts per millisecond (cpms). Solid dark red line indicates the average intensity and dashed dark red line indicates the average lifetime of this level. (**b**) Lifetime decay trace (black) of level shown in (**a**), corresponding result of MLE fitting (dark red), IRF (dark gray), and background (light gray). (**c**) Time trace (gray) measured in single Cy3 monomer scaffolded by DX tile at the HF position. The number of photons binned at 10 ms is indicated in cpms. Solid light red line indicates the average intensity and dashed light red line indicates the average lifetime of this level. (**d**) Lifetime decay trace (black) of level shown in **c**, corresponding result of MLE fitting (light red), IRF (dark gray), and background (light gray). Parameters of the fits are presented in Table S20.

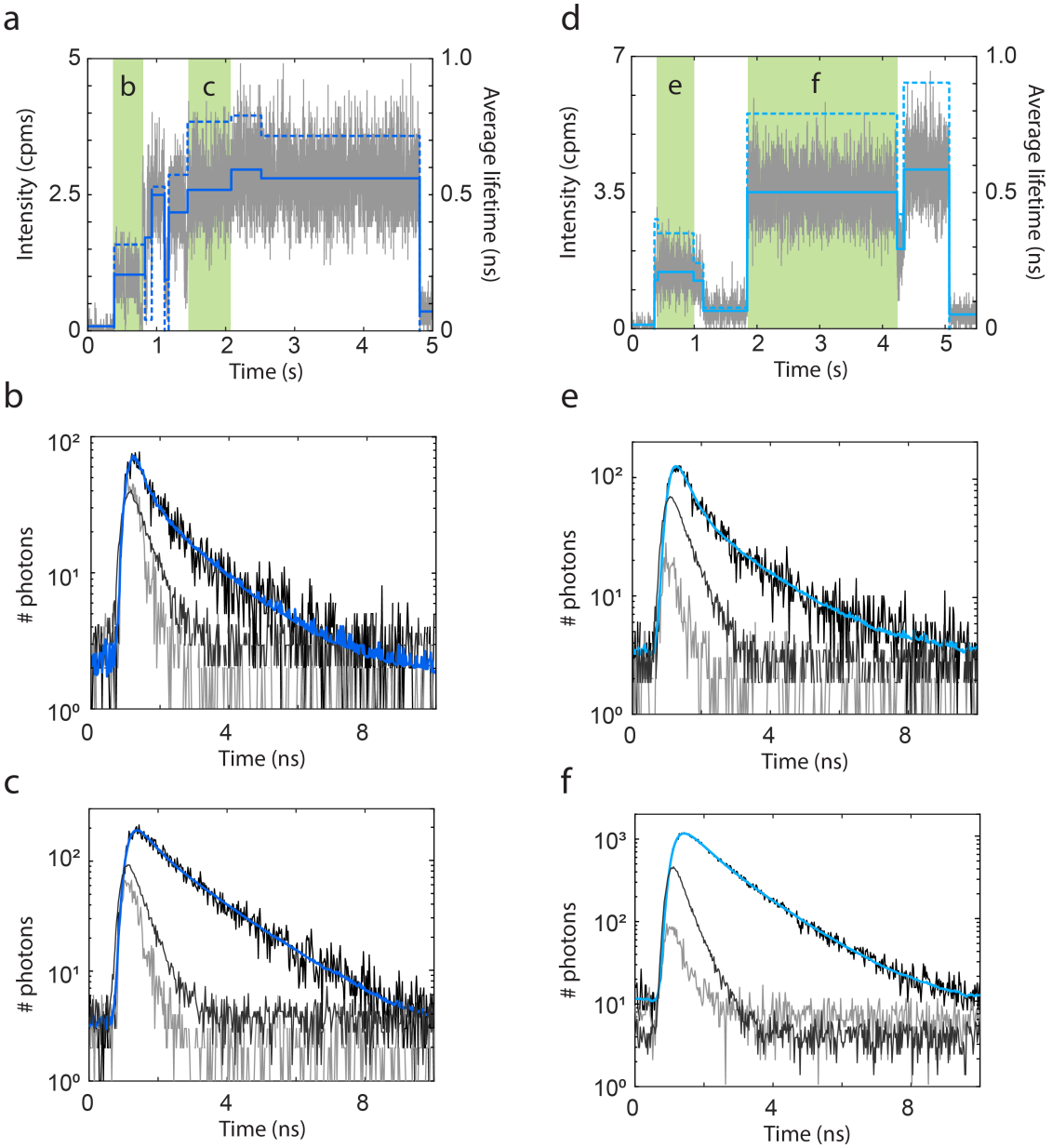


**Figure S28 | Representative single-molecule data for Cy3 dimer constructs.** (**a**) Time trace (gray) measured in single Cy3 dimer scaffolded by duplex at the high FRET (HF) position. The number of photons binned at 10 ms is indicated in counts per millisecond (cpms). Solid dark blue line indicates the average intensity and dashed dark blue line indicates the average lifetime of each level. (**b**) Lifetime decay trace (black) of representative low intensity level indicated in (**a**), corresponding result of MLE fitting (dark blue), IRF (dark gray), and background (light gray). (**c**) Lifetime decay trace (black) of representative high intensity level indicated in (**a**), corresponding result of MLE fitting (dark blue), IRF (dark gray), and background (light gray). (**d**) Time trace (gray) measured in single Cy3 dimer scaffolded by DX tile at the HF position. The number of photons binned at 10 ms is indicated in cpms. Solid light blue line indicates the average intensity and dashed light blue line indicates the average lifetime of each level. (**e**) Lifetime decay trace (black) of representative low intensity level indicated in (**e**), corresponding result of MLE fitting (light blue), IRF (dark gray), and background (light gray). (**f**) Lifetime decay trace (black) of representative high intensity level indicated in (**e**), corresponding result of MLE fitting (light blue), IRF (dark gray), and background (light gray). Parameters of the fits are presented in Table S20.

## S4.2 Lifetime fitting of single molecules

The fluorescence lifetime decay of each fluorescence intensity level was fitted individually by constructing a histogram of the delay times associated with all detected photons for that level and then using MLE reconvolution[10, 11] to extract two-lifetime components using the model fit function:

$$F(t) = N_{\mathrm{tot}}\left[(1-\gamma_F)\frac{A_0 + \mathrm{IRF} \otimes [A_1 \exp(-t/\tau_1) + (1-A_1)\exp(-t/\tau_2)]}{\int_{0\ \mathrm{ns}}^{12.5\ \mathrm{ns}} \{A_0 + \mathrm{IRF} \otimes [A_1 \exp(-t/\tau_1) + (1-A_1)(\exp -t/\tau_2)]\} dt} + \gamma_F \frac{\mathrm{BG}(t)}{\int_{0\ \mathrm{ns}}^{12.5\ \mathrm{ns}} \mathrm{BG}(t) dt}\right] \tag{12}$$

where $\gamma_F$ is the fraction of background signal, $\mathrm{BG}(t)$, as collected on the same sample in an area where there are no molecules. $N_{\mathrm{tot}}$ is the background-subtracted photon-count (area under the curve) of the lifetime trace. $\tau_1$ and $\tau_2$ are the two lifetime components, $A_1$ the fraction amplitude of $\tau_1$ and $A_0$ is an offset parameter. Representative lifetime fits are shown in Figure S27 and Figure S28. $\tau_1$ and $\tau_2$ of the four different constructs are presented in Figure S29, and the average lifetime of each single molecules is calculated and reported as:

$$\tau_{\mathrm{avg}} = A_1\tau_1 + (1-A_1)\tau_2 \tag{13}$$

**Table S20** | MLE fit results of lifetime traces of duplex and DX tile-scaffolded Cy3 monomer and dimer constructs, as shown in Figures S27 and S28, using Equation 12.

| **Trace ID** | $A_0$ | $A_1$ | $\tau_1$ [ns] | $\tau_2$ [ns] | $\gamma_F$ | $N_{\mathrm{tot}}$ |
|---|---|---|---|---|---|---|
| Duplex monomer (Figure S27b) | 0.00 | 0.66 | 0.12 | 1.91 | 0.13 | 1627 |
| DX tile monomer (Figure S27d) | 0.00 | 0.68 | 0.52 | 1.77 | 0.10 | 3583 |
| Duplex dimer (Figure S28b) | 0.01 | 0.79 | 0.24 | 2.00 | 0.17 | 57 |
| Duplex dimer (Figure S28c) | −0.01 | 0.43 | 0.26 | 2.26 | 0.05 | 626 |
| DX tile dimer (Figure S28e) | 0.00 | 0.88 | 0.17 | 1.83 | 0.15 | 234 |
| DX tile dimer (Figure S28f) | 0.00 | 0.60 | 0.35 | 1.47 | 0.06 | 2166 |

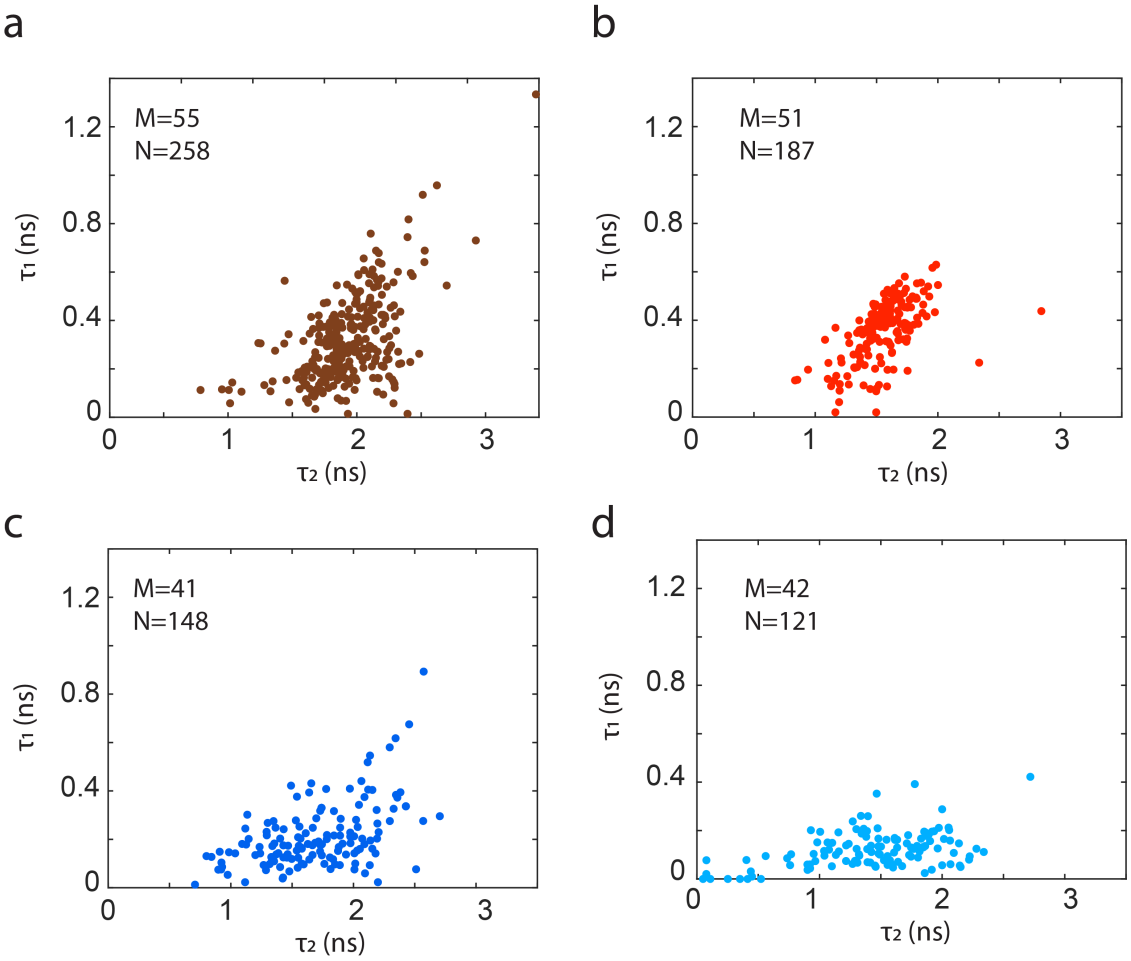


**Figure S29 | Scatter plot of the two lifetime components from single-molecule lifetime measurements.** The two time constants for each intensity level are shown for data from single monomeric Cy3 scaffolded by (**a**) duplex and by (**b**) DX tile, and for single dimeric Cy3 scaffolded by (**c**) duplex and by (**d**) DX tile at the high FRET (HF) position. Single Cy3 average lifetimes shown in Figure 4b and c are calculated from these components ($\tau_1$ and $\tau_2$) using Equation 13. For each construct, $M$ is the number of single molecules observed and $N$ is the total number of intensity levels recorded for the $M$ molecules.

# S5 Supplemental Data: Molecular dynamics simulations of Cy3 modified DNA duplexes and DX tiles

## S5.1 Structural analysis of DNA-scaffolded Cy3 from MD trajectories.

For monomeric, dimeric, and trimeric DNA-scaffolded Cy3 complexes, MD trajectories are analyzed to determine the binding behavior of monomeric Cy3 residues with the DNA and the other Cy3 residues (for dimers and trimers). In the monomeric and 0 nt dimeric MD simulations, the geometry of the Cy3 chromophores and neighboring DNA base-pairs is mapped by considering the centroid of the Cy3 chromophore, the three neighboring minor groove base-pairs, the unpaired bases opposite to the Cy3, and the three neighboring major groove base-pairs (Figures S30a, S31a, and S32a). The CPPTRAJ program[12] in AmberTools17[13] was utilized to extract distances from the Cy3 residues to the minor groove, opposite base-pairs, and the major groove, as well as the distance between Cy3 residues in the dimeric complexes (Figures S30c, S31c, and S32c).

For the dimeric complexes with 1 nt, 2 nt, and 3 nt spacers between Cy3 chromophores, only the distance between Cy3 residues and the transition dipole angles between Cy3 residues are reported (Figures S33c-d, S34c-d, and S35c-

d), which are the parameters correlating closely with the electronic coupling strength. For the trimeric complexes, the distance between each pair of Cy3 residues and the transition dipole angles between each pair of Cy3 residues are reported (Figures S36c-f and S37c-f).

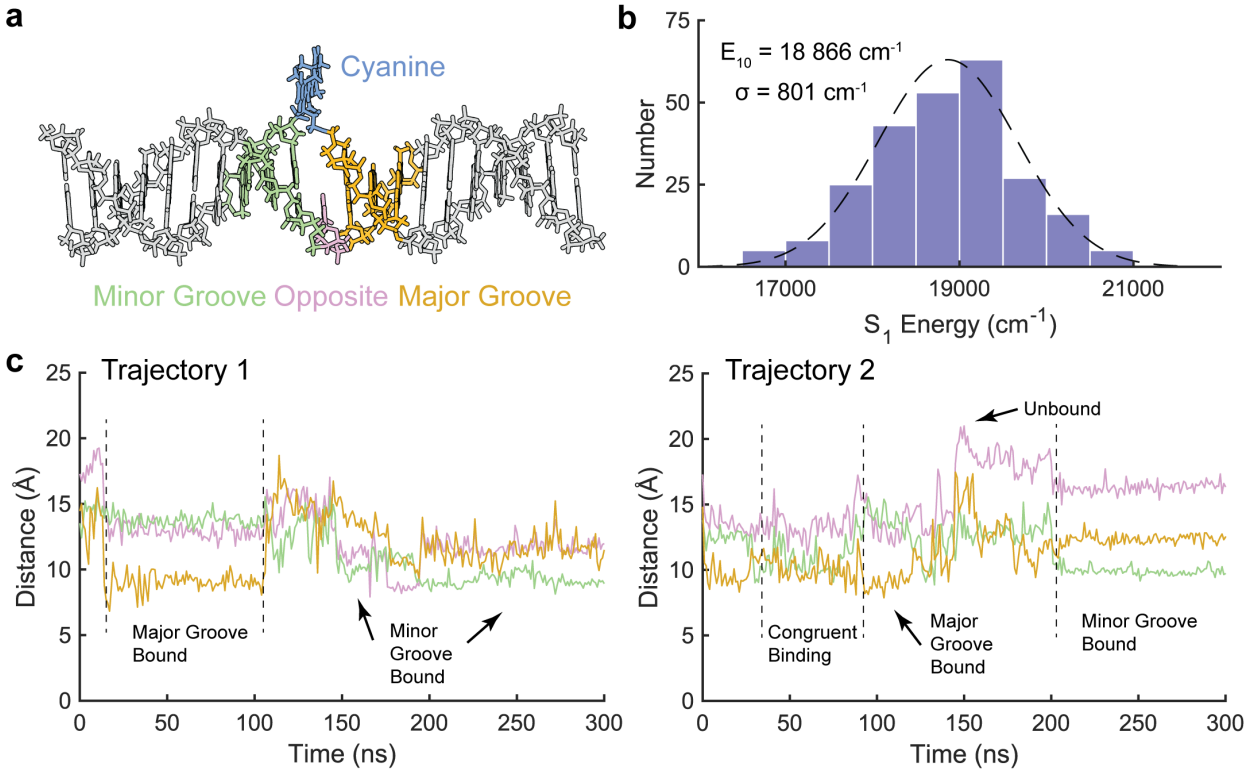


**Figure S30 | Molecular dynamics trajectories for the Cy3 monomer.** **(a)** Initial coordinates for DNA and Cy3 monomer complex, with the minor groove, major groove, and bases opposite to the Cy3 highlighted. **(b)** First singlet excited state energies calculated using TD-DFT and fit to a normal distribution. TD-DFT calculations performed on MD snapshots taken every 2 ns. **(c)** Coarse-grained distances of DNA and Cy3 taken during the MD simulations for two replicates (left and right, respectively).

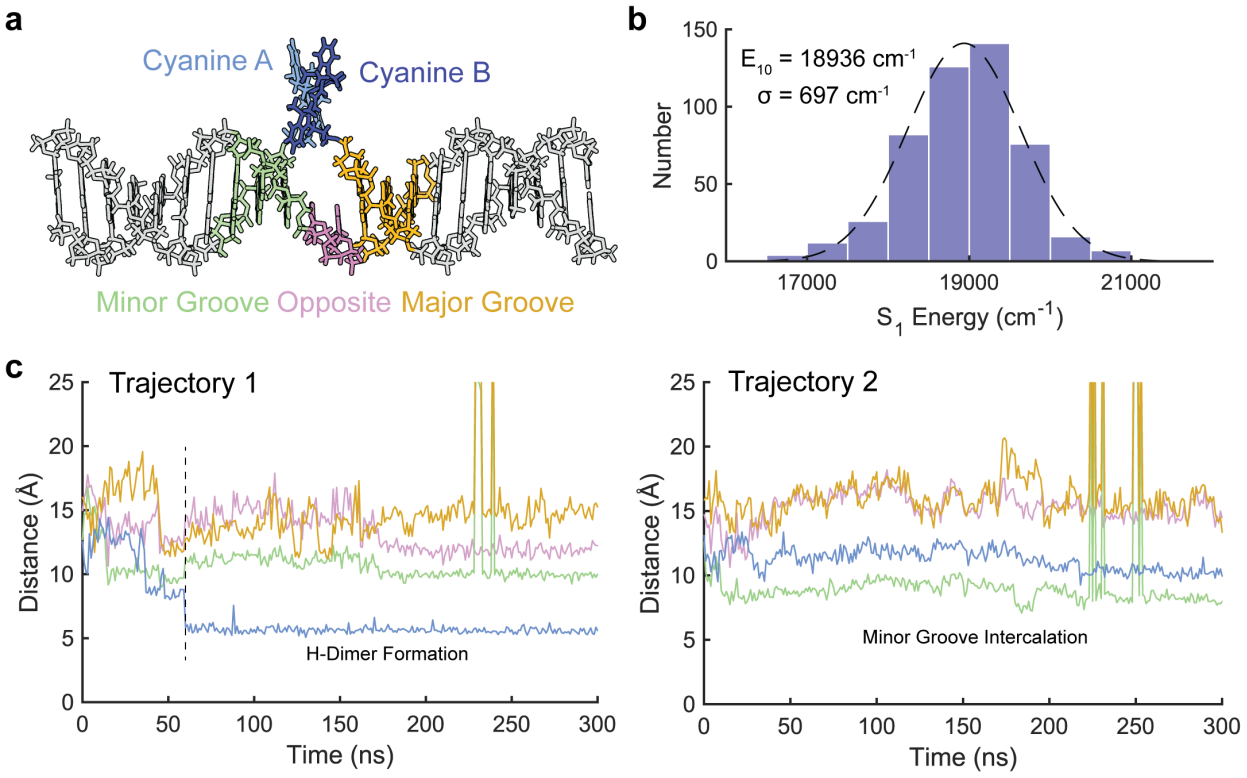


**Figure S31 | Molecular dynamics trajectories for the Cy3 dimer configuration one.** **(a)** Initial coordinates for DNA and Cy3 dimer complex in configuration one, with the minor groove, major groove, and bases opposite to the Cy3 highlighted. **(b)** First singlet excited state energies calculated using TD-DFT and fit to a normal distribution. TD-DFT calculations performed on MD snapshots taken every 2 ns. Energy values below 16500 cm$^{-1}$ and above 21500 cm$^{-1}$ are removed for this fit. **(c)** Coarse-grained distances of DNA and Cy3 taken during the MD simulations for two replicates (left and right, respectively).

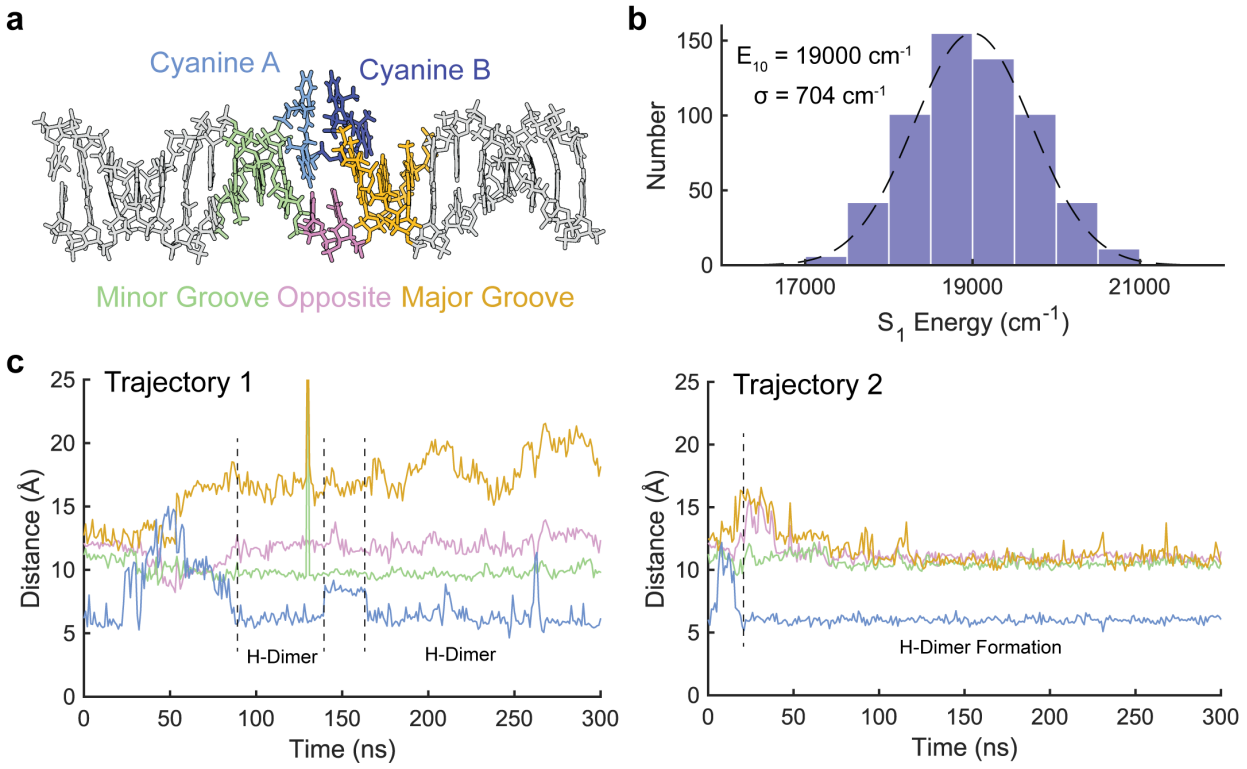


**Figure S32 | Molecular dynamics trajectories for the Cy3 dimer configuration two.** **(a)** Initial coordinates for DNA and Cy3 dimer complex in configuration two, with the minor groove, major groove, and bases opposite to the Cy3 highlighted. **(b)** First singlet excited state energies calculated using TD-DFT and fit to a normal distribution. TD-DFT calculations performed on MD snapshots taken every 2 ns. Energy values below 16500 $cm^{-1}$ and above 21500 $cm^{-1}$ are removed for this fit. **(c)** Coarse-grained distances of DNA and Cy3 taken during the MD simulations for two replicates (left and right, respectively).

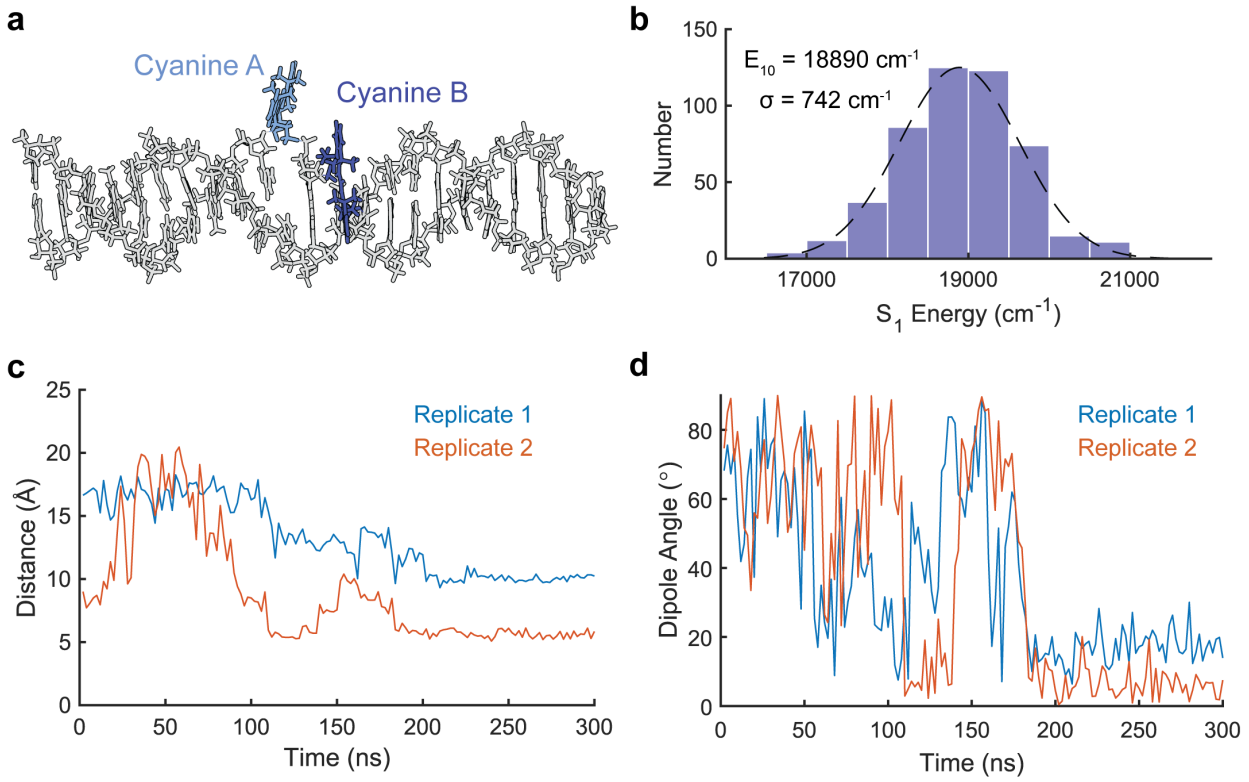


**Figure S33 | Molecular dynamics trajectories for the Cy3 dimer one nucleotide spacer. (a)** Initial coordinates for DNA and Cy3 dimer 1 nt complex, with the two Cy3 monomers highlighted. **(b)** First singlet excited state energies calculated using TD-DFT and fit to a normal distribution. TD-DFT calculations performed on MD snapshots taken every 2 ns. Energy values below 16500 $cm^{-1}$ and above 21500 $cm^{-1}$ are removed for this fit. **(c–d)** Coarse-grained distances of Cy3 distances and transition dipole angles taken during the MD simulations for two replicates.

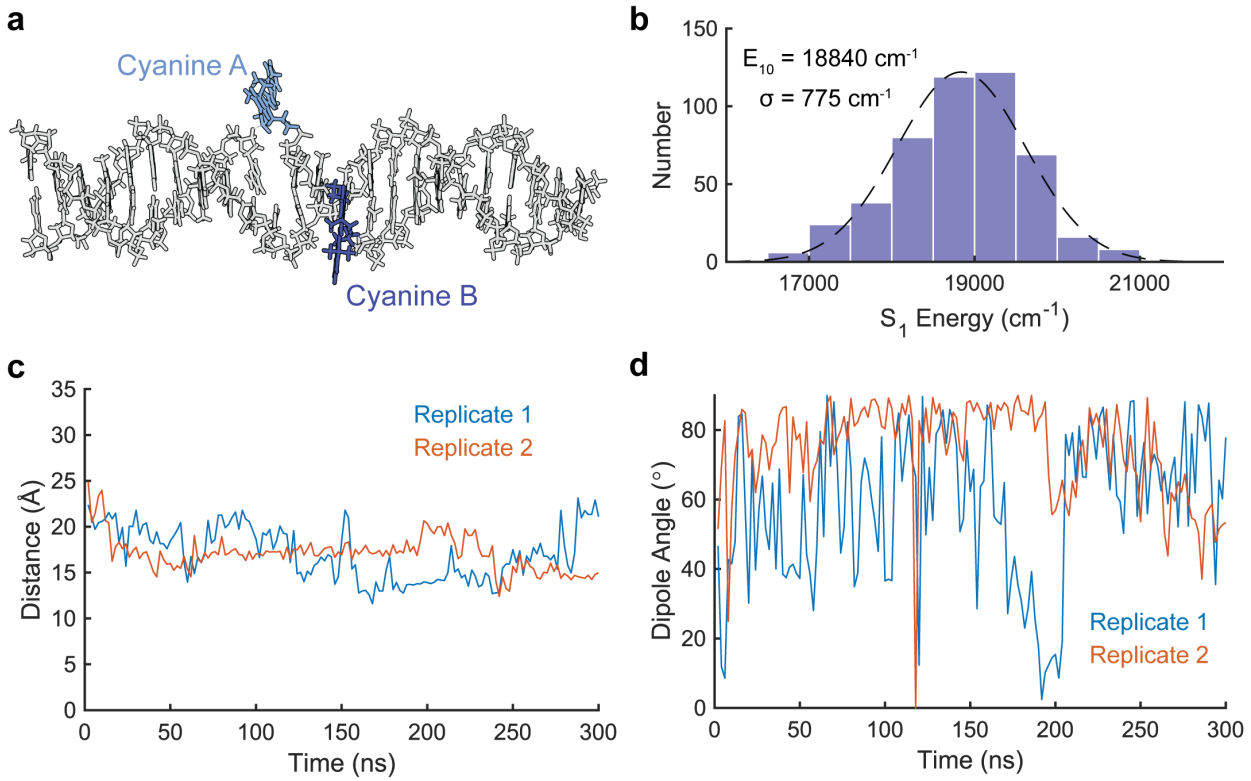


**Figure S34 | Molecular dynamics trajectories for the Cy3 dimer 2 nt spacer.** **(a)** Initial coordinates for DNA and Cy3 dimer 2 nt complex, with the two Cy3 monomers highlighted. **(b)** First singlet excited state energies calculated using TD-DFT and fit to a normal distribution. TD-DFT calculations performed on MD snapshots taken every 2 ns. Energy values below 16500 $cm^{-1}$ and above 21500 $cm^{-1}$ are removed for this fit. **(c–d)** Coarse-grained distances of Cy3 distances and transition dipole angles taken during the MD simulations for two replicates.

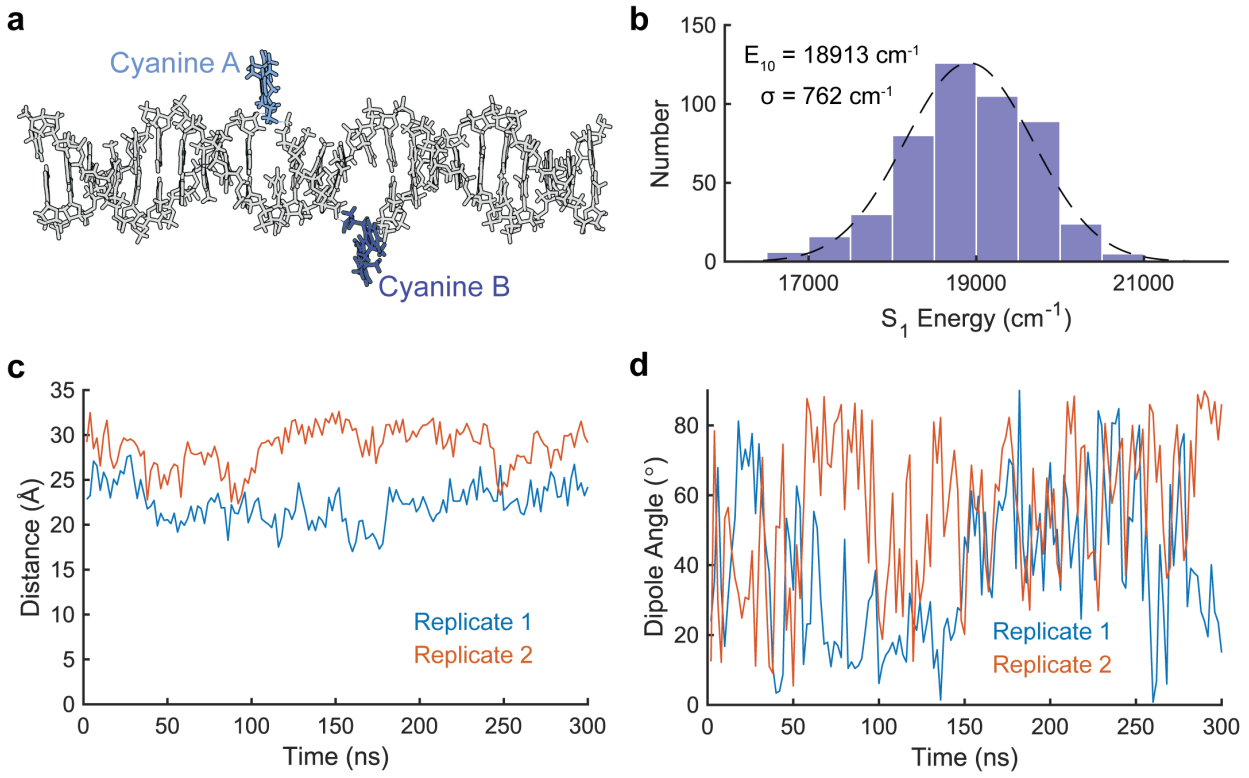


**Figure S35 | Molecular dynamics trajectories for the Cy3 dimer 3 nt spacer. (a)** Initial coordinates for DNA and Cy3 dimer 3 nt complex, with the two Cy3 monomers highlighted. **(b)** First singlet excited state energies calculated using TD-DFT and fit to a normal distribution. TD-DFT calculations performed on MD snapshots taken every 2 ns. Energy values below 16500 $cm^{-1}$ and above 21500 $cm^{-1}$ are removed for this fit. **(c–d)** Coarse-grained distances of Cy3 distances and transition dipole angles taken during the MD simulations for two replicates.

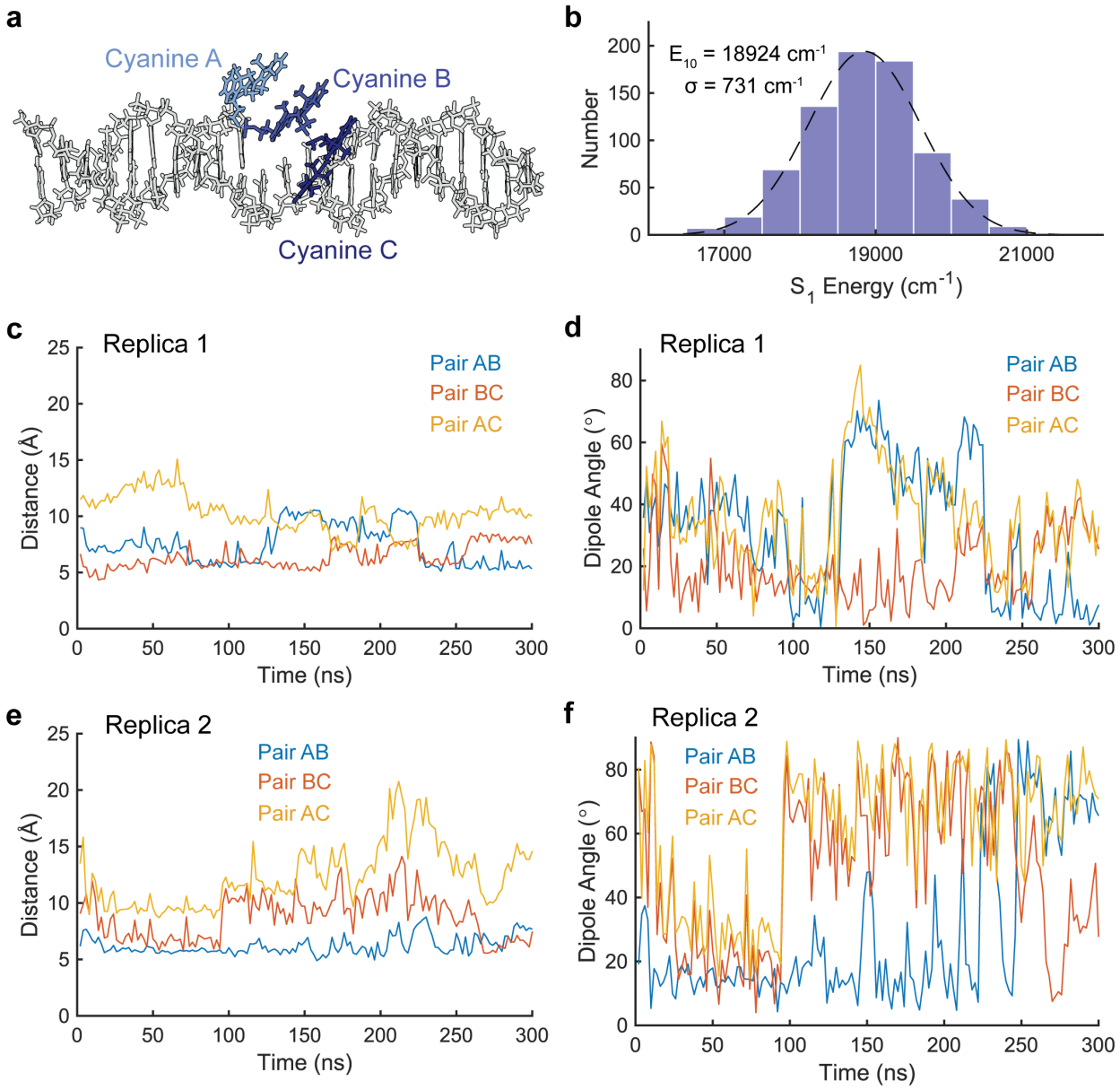


**Figure S36 | Molecular dynamics trajectories for the Cy3 trimer configuration one.** **(a)** Initial coordinates for DNA and Cy3 trimer configuration one, with the three Cy3 monomers highlighted. **(b)** First singlet excited state energies calculated using TD-DFT and fit to a normal distribution. TD-DFT calculations performed on MD snapshots taken every 2 ns. Energy values below 16500 $cm^{-1}$ and above 21500 $cm^{-1}$ are removed for this fit. **(c–d)** Coarse-grained distances of Cy3 distances and transition dipole angles taken during the MD simulations for the first replicate. **(e–f)** Coarse-grained distances of Cy3 distances and transition dipole angles taken during the MD simulations for the second replicate.

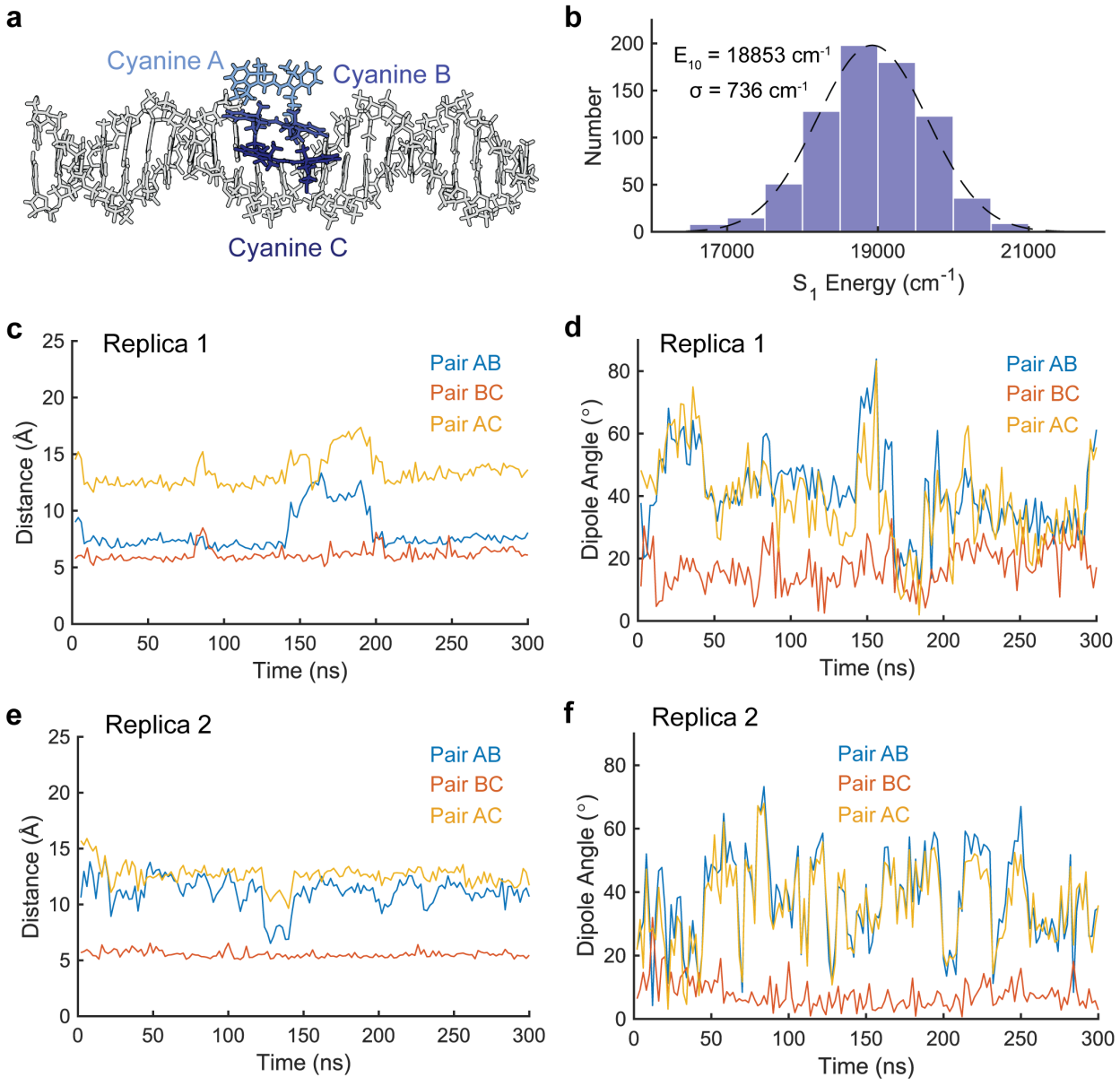


**Figure S37 | Molecular dynamics trajectories for the Cy3 trimer configuration two.** **(a)** Initial coordinates for DNA and Cy3 trimer configuration two, with the three Cy3 monomers highlighted. **(b)** First singlet excited state energies calculated using TD-DFT and fit to a normal distribution. TD-DFT calculations performed on MD snapshots taken every 2 ns. Energy values below 16500 $cm^{-1}$ and above 21500 $cm^{-1}$ are removed for this fit. **(c–d)** Coarse-grained distances of Cy3 distances and transition dipole angles taken during the MD simulations for the first replicate. **(e–f)** Coarse-grained distances of Cy3 distances and transition dipole angles taken during the MD simulations for the second replicate.

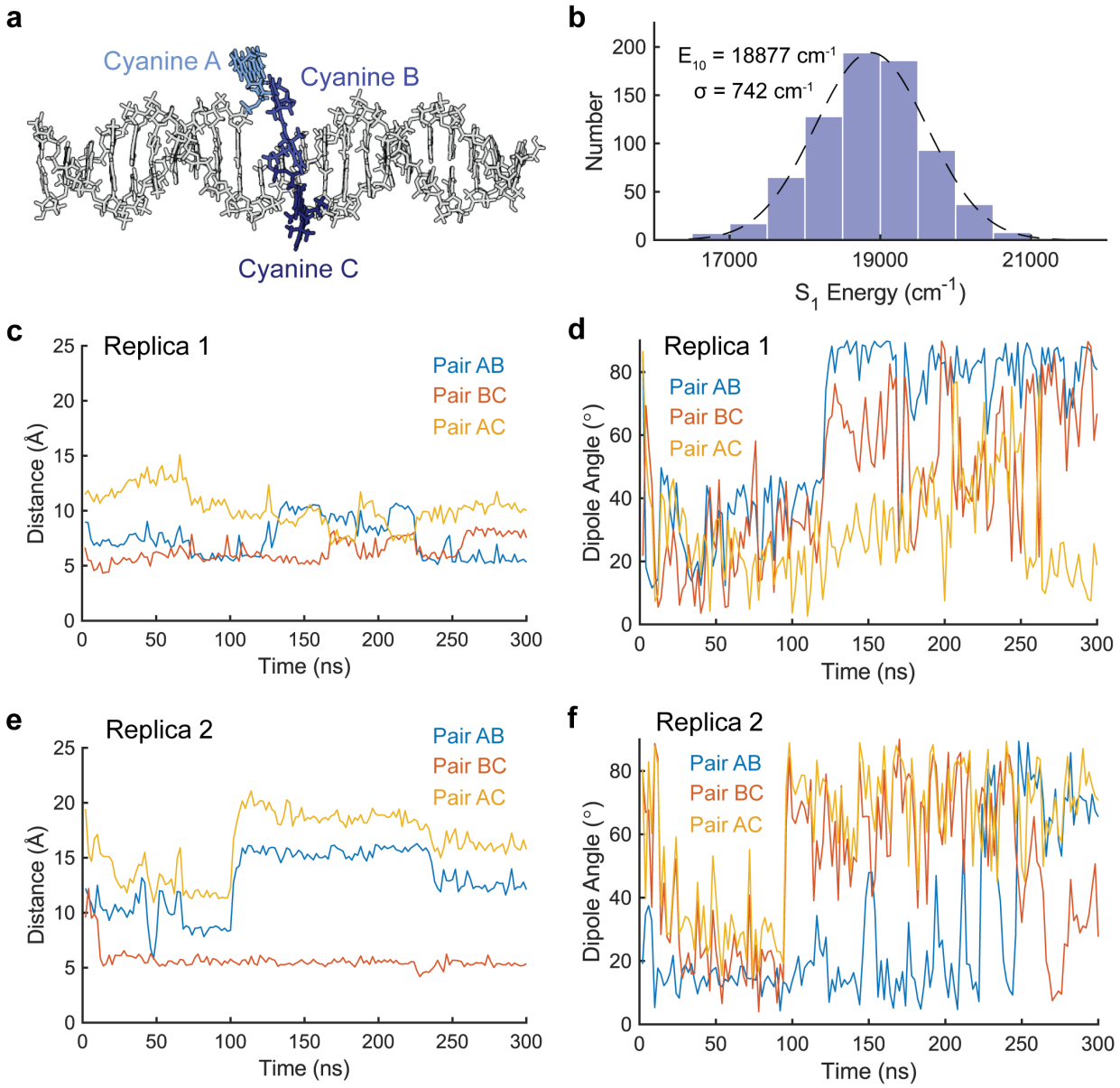


**Figure S38 | Molecular dynamics trajectories for the Cy3 trimer configuration three.** **(a)** Initial coordinates for DNA and Cy3 trimer configuration three, with the three Cy3 monomers highlighted. **(b)** First singlet excited state energies calculated using TD-DFT and fit to a normal distribution. TD-DFT calculations performed on MD snapshots taken every 2 ns. Energy values below 16500 $cm^{-1}$ and above 21500 $cm^{-1}$ are removed for this fit. **(c–d)** Coarse-grained distances of Cy3 distances and transition dipole angles taken during the MD simulations for the first replicate. **(e–f)** Coarse-grained distances of Cy3 distances and transition dipole angles taken during the MD simulations for the second replicate.

## S5.2 Local environmental effects on Cy3 residues.

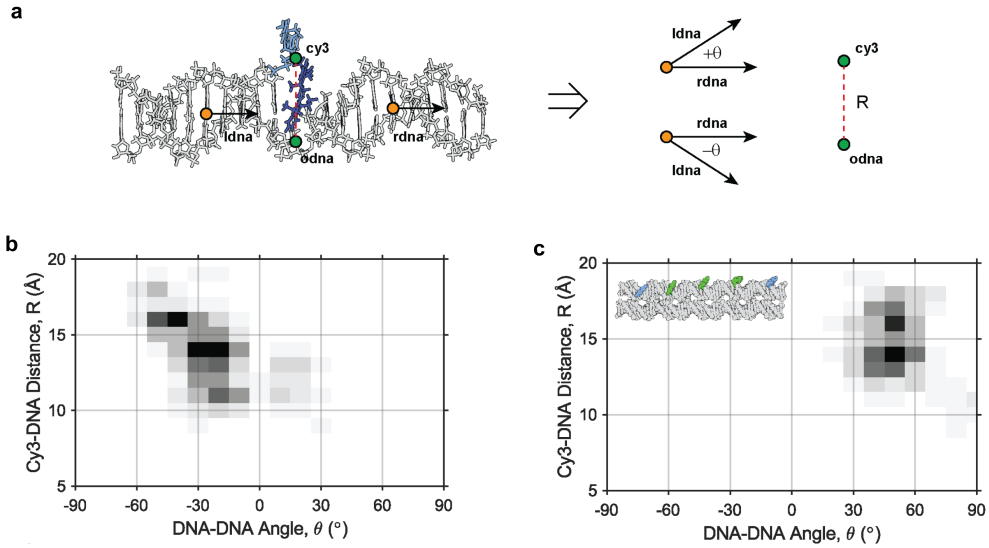


**Figure S39 | Configurational effect of Cy3 modifications on local DNA structure.** **(a)** On-the-fly local coordinate system for analyzing the DNA environment with respect to the Cy3 modification during an MD simulation. The sign of the DNA bending angle, $\theta$, depends on the relative direction of the Cy3-DNA axis, which has a distance of $R$. Correlation between the DNA-DNA bending angle, $\theta$, and the Cy3-DNA distance, $R$, for **(b)** duplex monomers with Cy3 in the center position, **(c)** inner DX tile monomers.

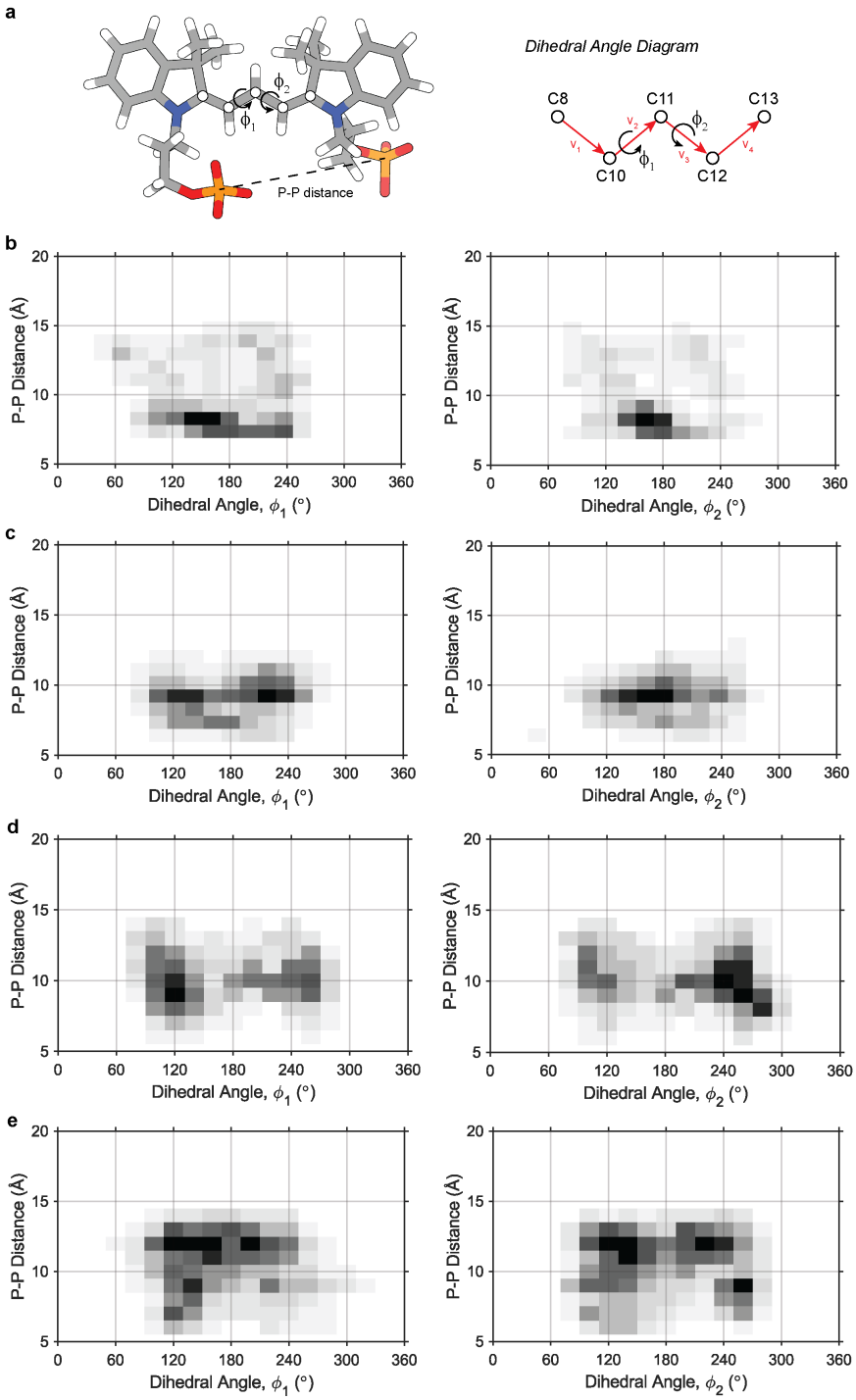


**Figure S40 | Local fluctuations in Cy3 modification structure.** **(a)** Diagram of Cy3 modification showing the location of dihedral angles $\phi_1$ and $\phi_2$, as well as the distance spanning consecutive phosphate groups. **(b)** Correlation between the dihedral angles, $\phi_1$ (left) and $\phi_2$ (right), and the P-P distance for duplex monomers, **(c)** duplex dimers, **(d)** DX tile monomers, and **(e)** DX tile dimers.

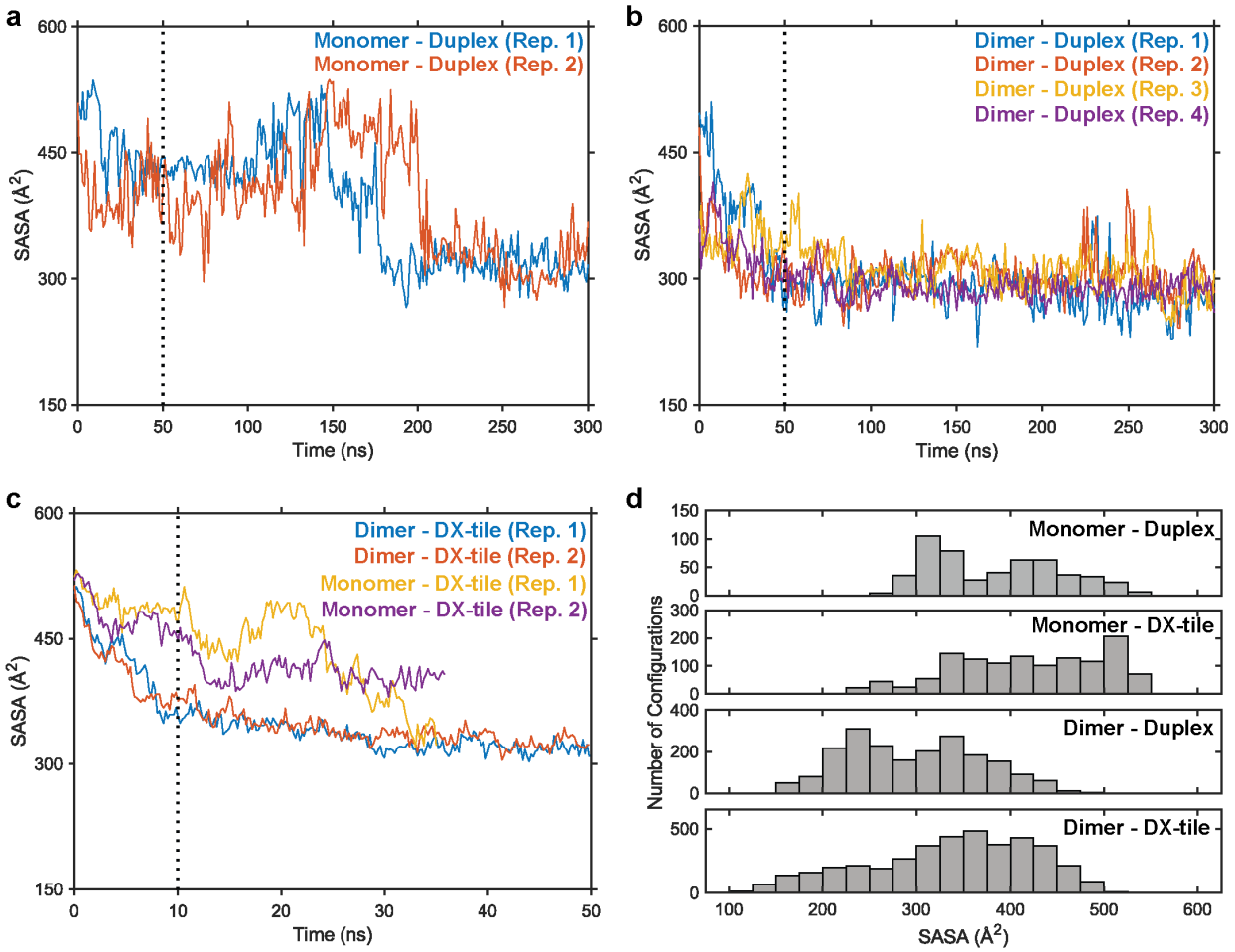


**Figure S41 | Solvent accessible surface area (SASA) of Cy3 residues.** Solvent accessible surface area (SASA) of the **(a)** Cy3 monomer replicates and the **(b)** Cy3 dimer replicates in duplex DNA, and of the **(c)** Cy3 monomer/dimer replicates on a DX tile over the MD simulation time. For the dimer simulations, each data point represents the average of the two monomeric Cy3 residues. **(d)** Comparison of SASA values for the duplex and DX tile constructs, where configurations were sampled after 50 ns (duplex) or 10 ns (DX tile). For the dimer simulations, each monomeric Cy3 residue is sampled separately.

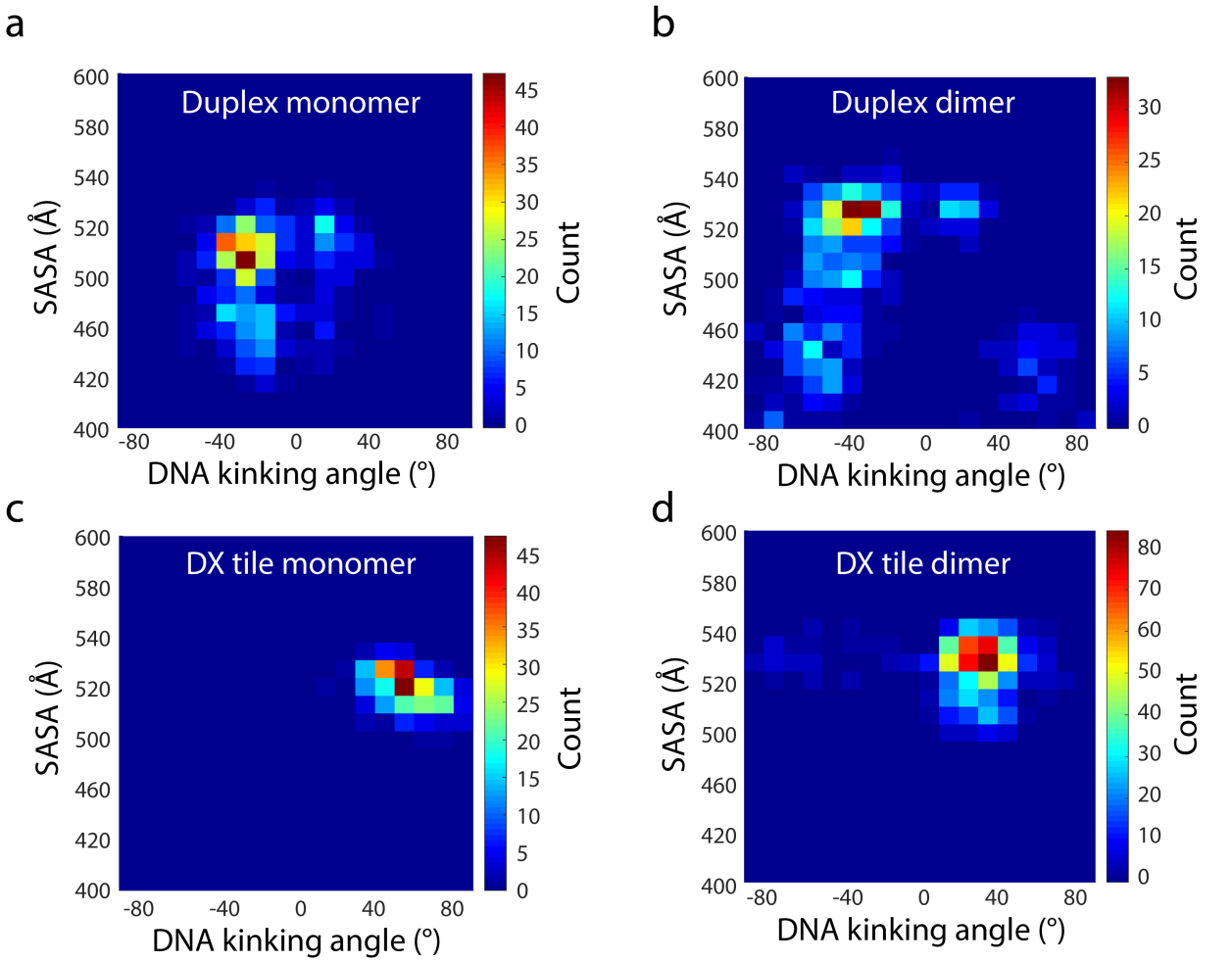


**Figure S42 | Solvent accessible surface area (SASA) and DNA kinking of Cy3 residues.** Comparison of solvent accessible surface area (SASA) and DNA kinking angles of Cy3 monomer on **(a)** duplex and **(b)** DX tile and of Cy3 dimer on **(c)** duplex and **(d)** DX tile

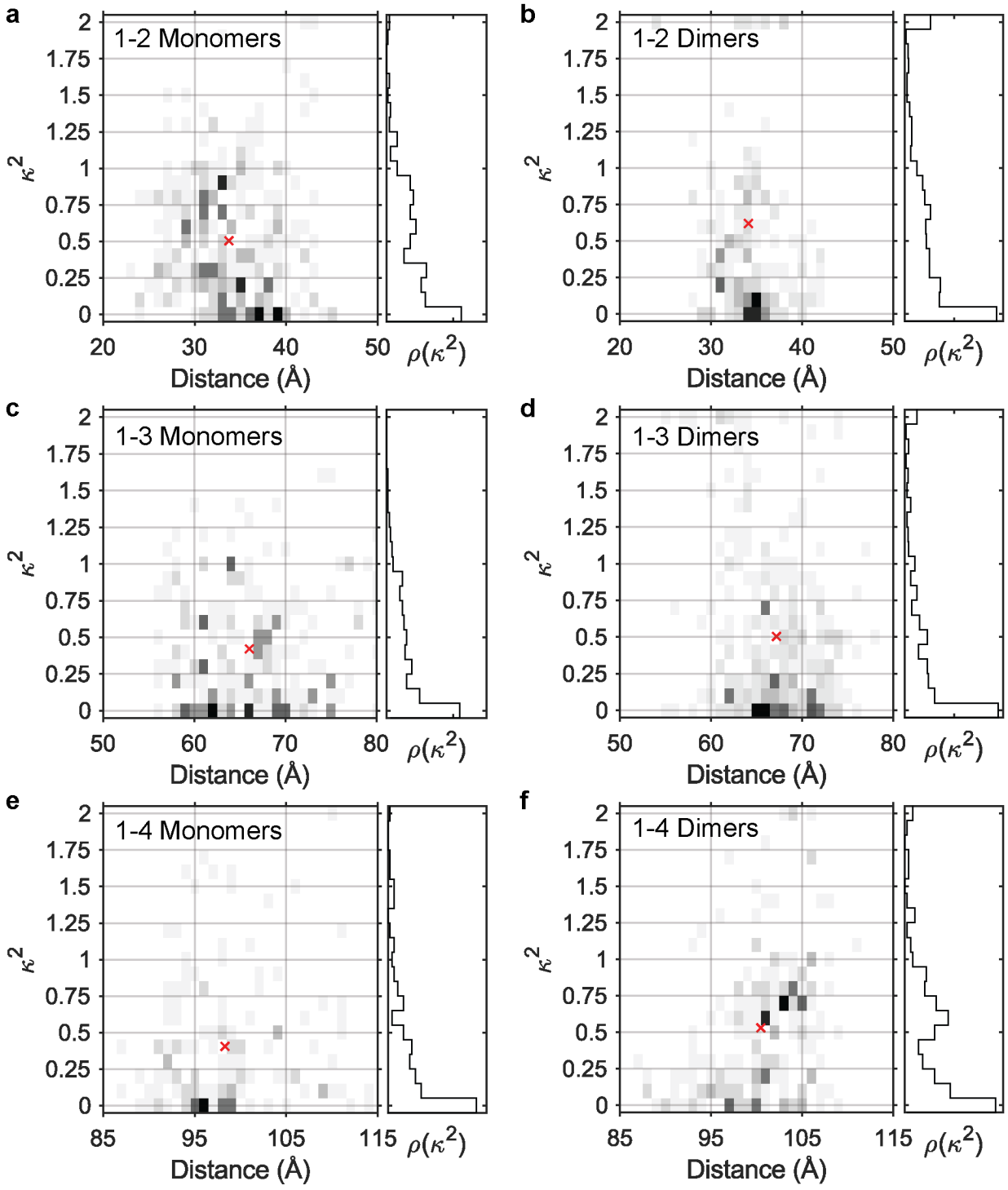


**Figure S43 | Orientational distribution of Cy3 residues in DX tiles.** Transition dipole moment orientations of the Cy3 residues in the **a,c,e** DX tile monomer and **b,d,f** DX tile dimer constructs.

## S5.3 Cy3 monomer optical properties.

Figure S44 shows the theoretical spectra calculated with the methods described in Section S6.6.

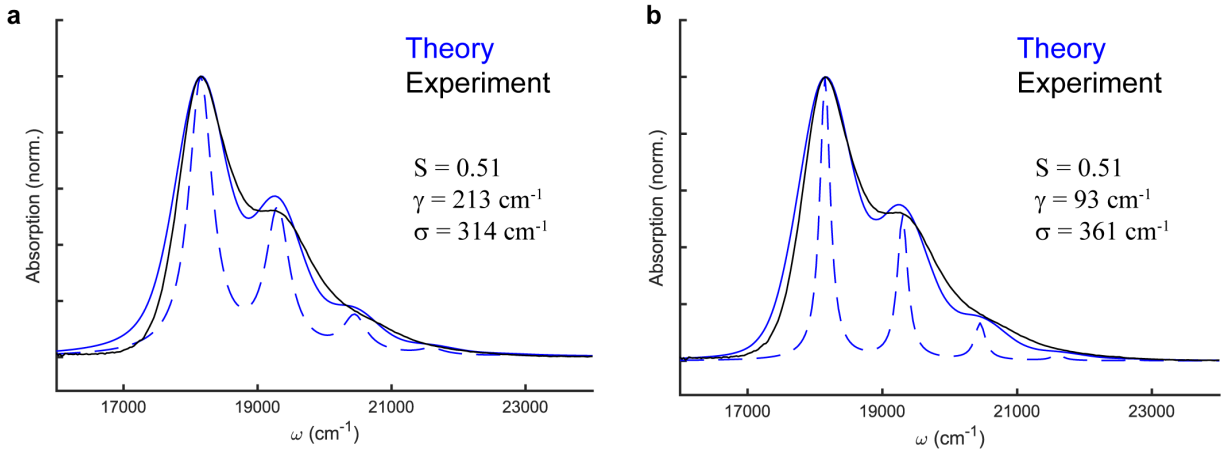


**Figure S44 | Cy3 monomer fit to linear absorption theory.** **(a)** Linear absorption fit using homogeneous broadening parameter ($\gamma$ = 213 cm$^{-1}$) from 2D spectroscopy in this study (Figure SX). **(b)** Linear absorption fit using homogeneous broadening parameter ($\gamma$ = 93 cm$^{-1}$) from Kringle et al.[1]

## S5.4 Multi-state model for multimeric Cy3.

Figures S45 - S52 show the distribution in electronic coupling and resultant absorption spectra for Cy3 dimers and trimers calculated through the methods described in Section S6.7.

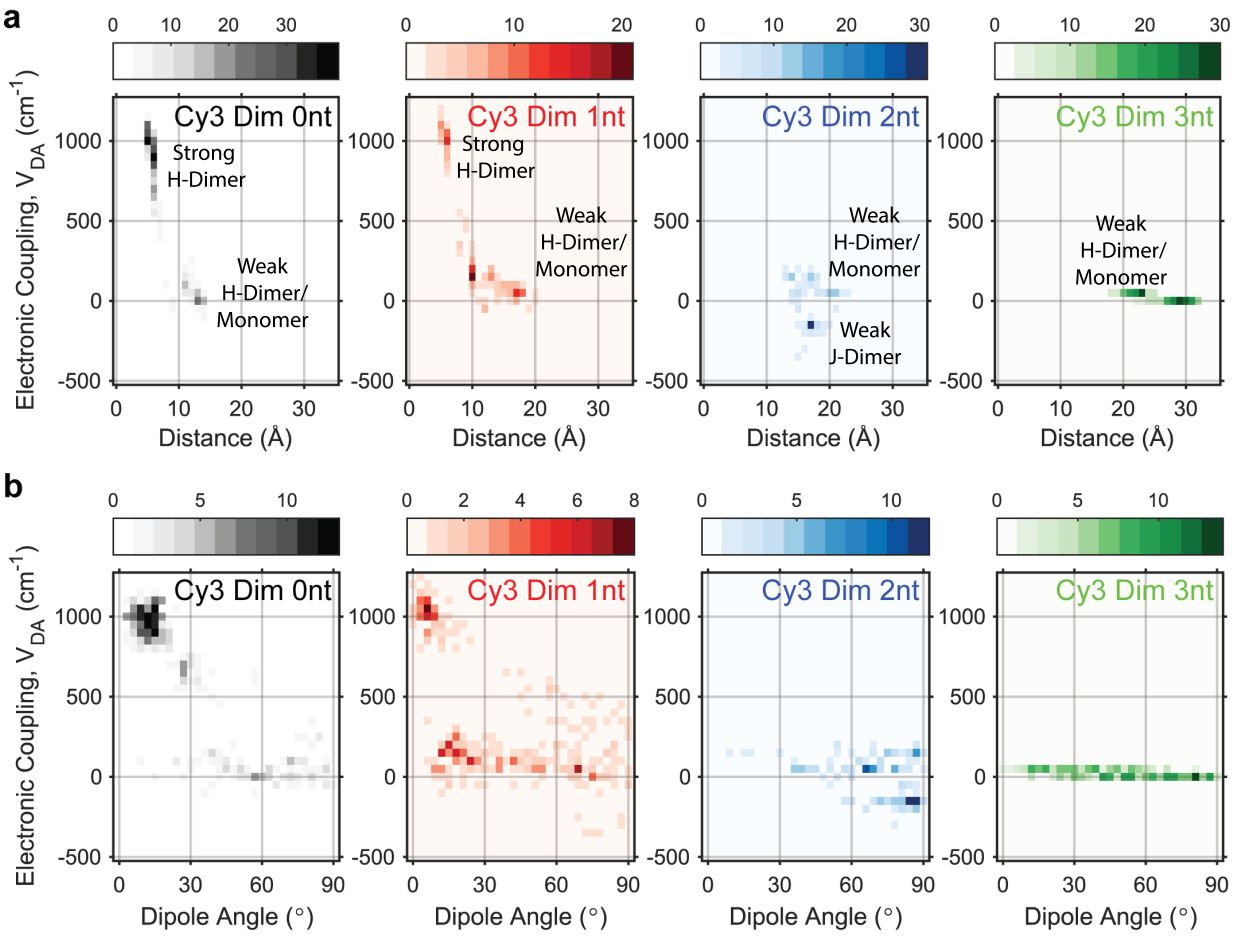


**Figure S45 | Configurations from Cy3 dimer molecular dynamics trajectories.** **(a)** Distance vs. electronic coupling ($V_{DA}$) for Cy3 dimer MD trajectories. From left to right, 0 nt, 1 nt, 2 nt, and 3 nt spacers. TD-DFT calculations performed on MD snapshots taken every 2 ns. **(b)** Dipole angle vs. electronic coupling ($V_{DA}$) for Cy3 dimer MD trajectories. From left to right, 0 nt, 1 nt, 2 nt, and 3 nt spacers.

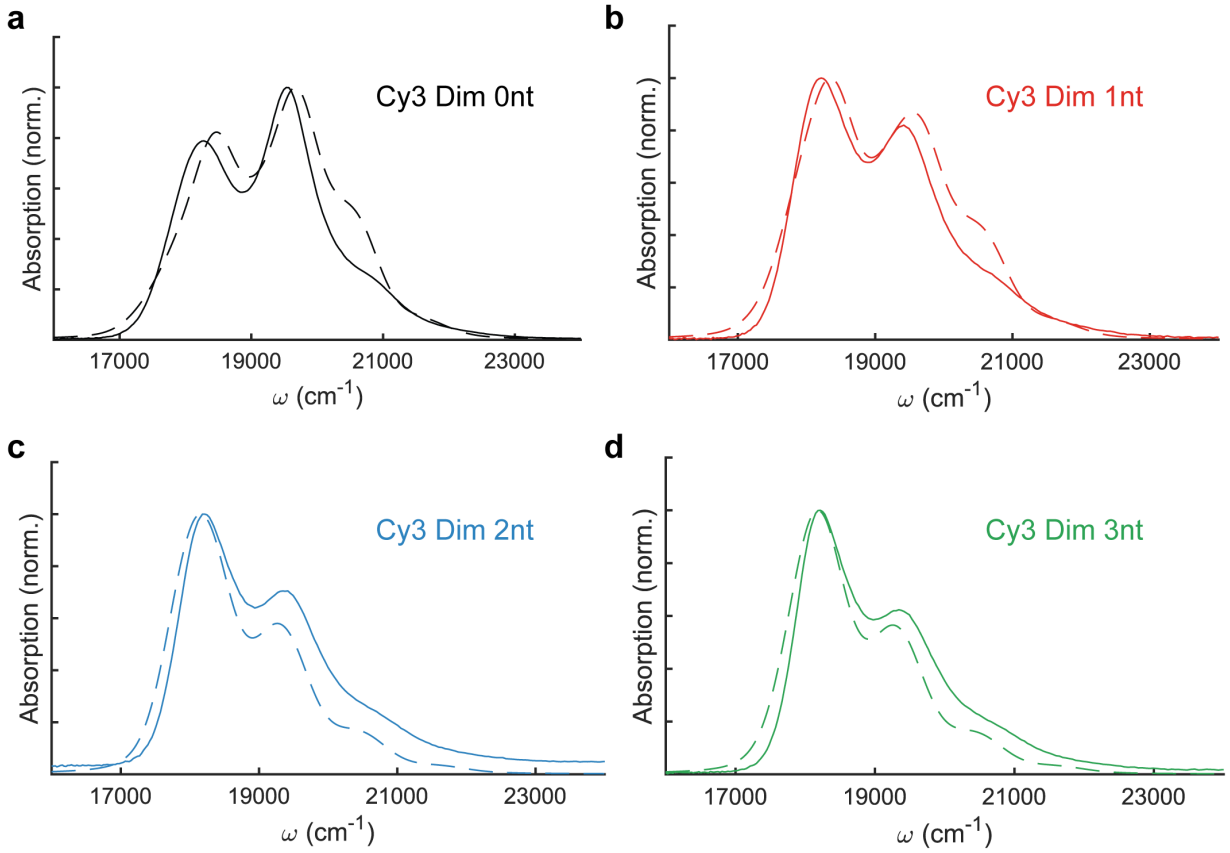


**Figure S46 | Ensemble absorbance spectra from Cy3 dimer molecular dynamics trajectories.** Calculated ensemble absorbance spectra (dashed) compared to experimental absorbance spectra (solid) for the **(a)** 0 nt dimer (black), the **(b)** 1 nt dimer (red), the **(c)** 2 nt dimer (blue), and the **(d)** 3 nt dimer (green). The configurational ensemble for each trimer is composed of MD snapshots taken every 2ns.

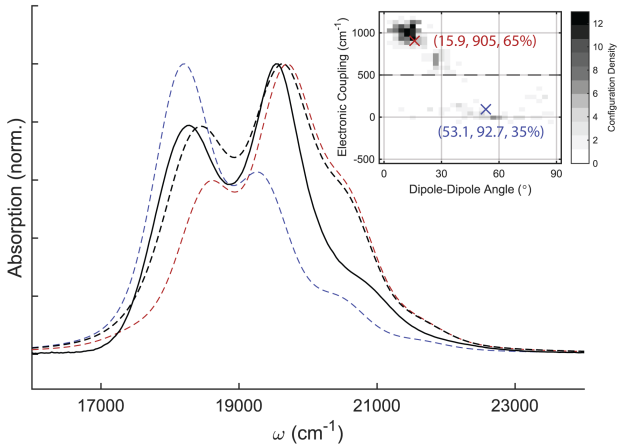


**Figure S47 | Absorbance spectra for Cy3 dimer 0 nt.** Calculated spectrum for strongly coupled sub-population shown in dashed red, weakly coupled sub-population shown in dashed blue, weighted sum shown in dashed black, and experimental spectrum shown in solid black.

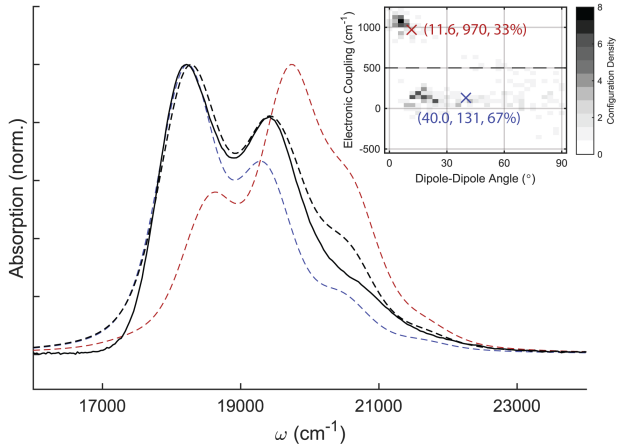


**Figure S48 | Absorbance spectra for Cy3 dimer 1 nt.** Calculated spectrum for strongly coupled sub-population shown in dashed red, weakly coupled sub-population shown in dashed blue, weighted sum shown in dashed black, and experimental spectrum shown in solid black.

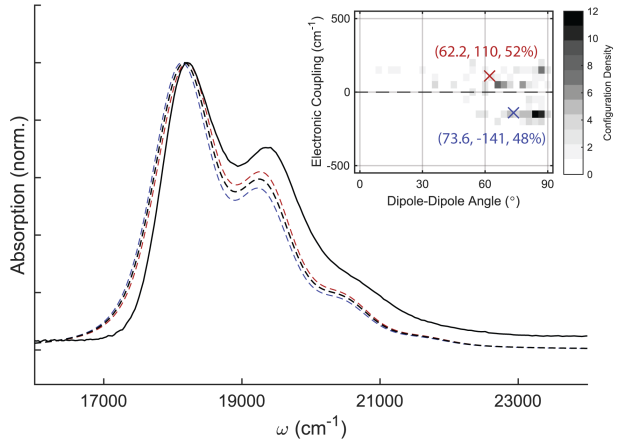


**Figure S49 | Absorbance spectra for Cy3 dimer 2 nt.** Calculated spectrum for H-like aggregate sub-population shown in dashed red, J-like aggregate sub-population shown in dashed blue, weighted sum shown in dashed black, and experimental spectrum shown in solid black.

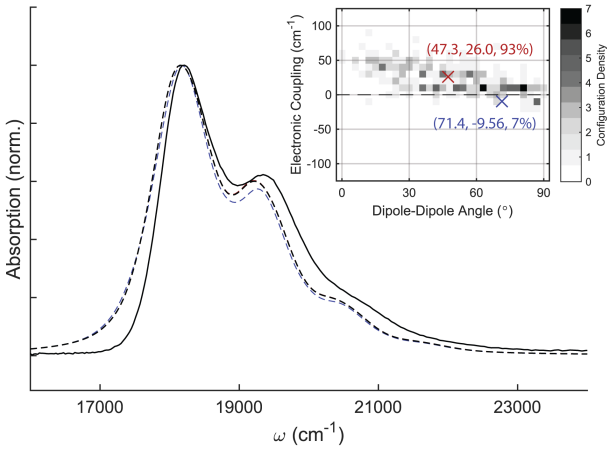


**Figure S50 | Absorbance spectra for Cy3 dimer 3 nt.** Calculated spectrum for H-like aggregate sub-population shown in dashed red, J-like aggregate sub-population shown in dashed blue, weighted sum shown in dashed black, and experimental spectrum shown in solid black.

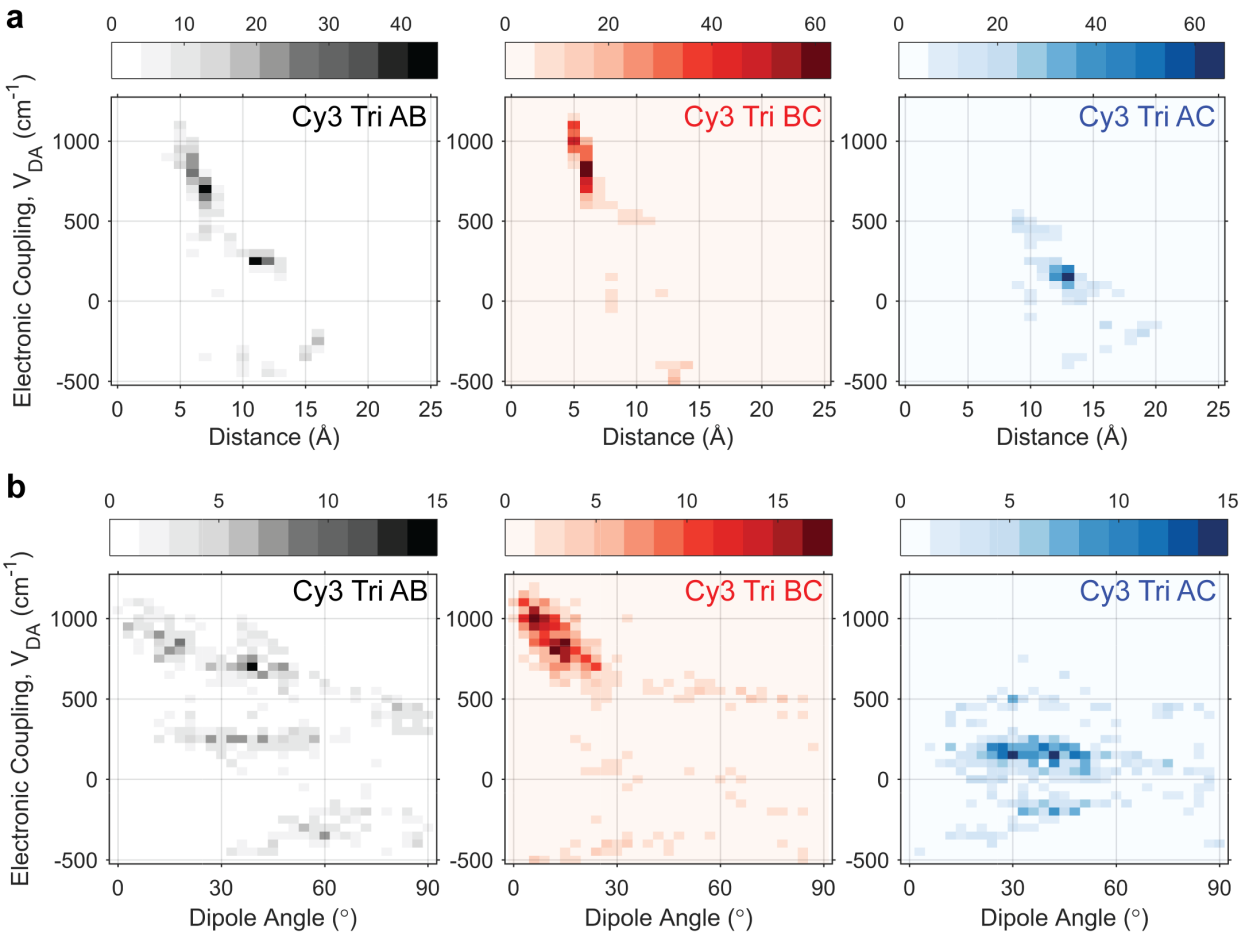


**Figure S51 | Configurations from Cy3 trimer molecular dynamics trajectories.** **(a)** Distance vs. electronic coupling ($V_{DA}$) for Cy3 trimer MD trajectories. From left to right, Cy3 monomer pairs AB, BC, and AC in the trimer configuration. TD-DFT calculations performed on MD snapshots taken every 2 ns. **(b)** Dipole angle vs. electronic coupling ($V_{DA}$) for Cy3 trimer MD trajectories. From left to right, Cy3 monomer pairs AB, BC, and AC in the trimer configuration.

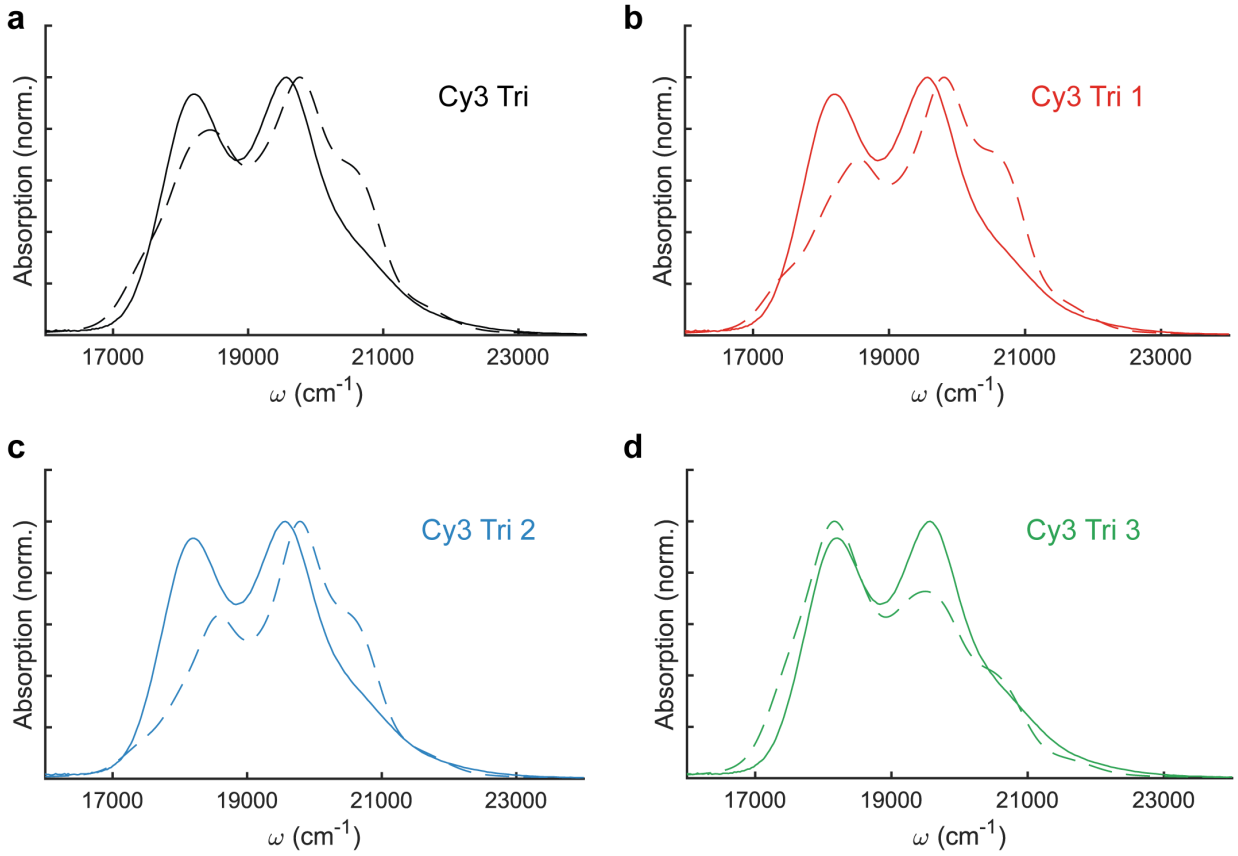


**Figure S52 | Absorbance spectra for Cy3 trimer.** Calculated ensemble absorbance spectra (dashed) compared to experimental absorbance spectra (solid) for the **(a)** average trimer configuration (black), the **(b)** trimer configuration 1 (red), the **(c)** trimer configuration 2 (blue), and the **(d)** trimer configuration 3 (green). The configurational ensemble for each type of dimer composed of MD snapshots taken every 2ns.

# S6 Supplemental Experimental Procedures

## S6.1 Two-dimensional electronic spectroscopy

Pulses for the 2D electronic spectrosocpy and homodyne transient grating experiment were obtained using the output of a Ti:sapphire regenerative amplifier (Coherent Libra, 5 kHz, 1.1 mJ output, 40 fs pulse generated at 800 nm). Broadband white light pulses were generated by focusing the output of the amplifier into an argon gas chamber (20 psi). The pulse was subsequently filtered through an 805-nm cutoff dichroic mirror (Thorlabs) and a Schott®glass filter (Thorlabs FGV9). A pair of chirped mirrors (Ultrafast Innovations GmbH) was used to compress the pulse to a duration of 11 fs for a 0.2 mm cuvette. The pulse was characterized with a transient grating frequency resolved optical gate in methanol (shown in Supplemental Figure S12). Two beamsplitters were used to split the pulse into four identical beams in a half-inch BOXCARS geometry, three of which were used as pump pulses and fourth which was attenuated with an OD 3.0 neutral-density filter for use as a reference pulse (local oscillatory). The delay between pulses one and two (coherence time, $t_1$) was controlled using two nanopositioners with an all-reflective interferometric delay.[14, 15] The population time (the time delay between pulses 2 and 3, $t_2$) was controlled using an Aerotech translation stage. The local oscillator timing was controlled manually and was set to precede pulse 1 by $\sim$500 fs. Heterodyne detected spectra were collected with shot-to-shot scatter removal on a high-speed line CCD (e2v) coupled to two choppers (1.25 kHz, 2.5 kHz) synchronized to the 5 kHz laser output. Pulse powers of 12 nJ were used with a 100 $\mu$m beam waist for samples with an optical density of 0.3. 2D spectra were phased with analogously detected 2D spectra according to the projection slice theorem. The homodyne detected transient grating data were detected using a Toshiba TCD1304AP with a 600 lines mm$^{-1}$ grating.

## S6.2 Cy3 force field generation.

In order to perform all-atom molecular dynamics simulations for DNA-scaffolded Cy3 aggregates, a molecular mechanical force field was generated for the Cy3 monomer. A molecular model of Cy3 with propyl chains was built using DS Visualizer (San Diego: Dassault Systémes, Release 4.1), and the geometry was minimized using GAMESS[16] with the restricted Hartree-Fock (RHF) method and the 6-31(d) Gaussian basis set.[17] Subsequently, atomic point charges were generated by a restrained electrostatic potential (RESP) fit[18] by the R.E.D. IV charge-fitting software.[19] The atomic point charges were averaged between geometrically identical atom types on the Cy3 molecule, and the generalized Amber force field (GAFF)[2] was utilized for all molecular mechanical force field terms (Figure S53a-b). The atomic point charges at the phosphate-Cy3 linkage were chosen to be identical to the DNA phosphate point charges for greater generality.

## S6.3 Construction of DNA-Cy3 all-atom systems.

Initial atomic models of DNA-scaffolded Cy3 monomers, dimers, and trimers were built using DS Visualizer (San Diego: Dassault Systémes, Release 4.1) from initial models of B-form DNA and optimized Cy3 molecules from the force field generation procedure. The B-form DNA[20] was built using the nucleic acid builder (NAB) as implemented in AmberTools17.[13] One initial geometry for the monomer, two initial geometries for the dimer, and two initial geometries for the trimer were built as shown in Figure S53c-d. The two initial dimer geometries correspond to a non-dimerized and a dimerized Cy3 complex, respectively, both with transition dipoles roughly orthogonal to the helical axis of the DNA. The two initial trimer geometries correspond to aggregated complexes, one with transition dipoles roughly orthogonal and the other with transition dipoles roughly parallel to the helical axis of DNA. The DNA-scaffolded Cy3 complexes were immersed in TIP3P water molecules[21], and explicit $Mg^{2+}$ and $Cl^{-}$ ions were added to neutralize the DNA and Cy3 molecules, and to set the simulation cell ion concentrations to 12 mM, which is consistent with experimental conditions.

## S6.4 All-atom molecular dynamics simulations.

The all-atom molecular dynamics simulations were performed using the program Amber16[13] with the OL15 force field[3] for nucleic acids, and the GAFF2 force field[2] for the Cy3 molecules. Periodic boundary conditions were applied in an orthogonal simulation cell, and the dynamics were integrated at a time step of 2 fs. Van der Waals energies were calculated using a 12 Å cutoff. The Particle Mesh Ewald (PME) method was used to calculate full electrostatics with a grid spacing of 1 Å. Full electrostatic forces and non-bonded forces were calculated at each time step (2 fs). These simulations were performed in the $NpT$ ensemble using a Berendsen barostat for pressure control at 1 bar[22], and Langevin dynamics for temperature control at 300 K with a collision frequency of 5 $ps^{-1}$.[23] Hydrogen atom bonds were constrained to their equilibrium lengths using the SHAKE algorithm[24] during the simulations, and system configurations were recorded every 1 ps for downstream analysis. Prior to dynamics, energy minimization was performed on the solvent and ions alone, followed by the full unconstrained system for 10,000 steps each. Next, the solvent and ions were allowed to equilibrate as the system was heated to 300 K while the nucleic acid was harmonically constrained for 20 ps, followed by an unconstrained equilibration for 200 ps. For production dynamics, each system was run for 300 ns in duplicate (600 ns total).

## S6.5 Cy3 excited state calculations.

The position of the Cy3 molecules was sampled at every 2 ns, for 150 total configurations from each production MD simulation. The CPPTRAJ program,[12] as implemented in AmberTools17,[13] was utilized to extract the Cy3 coordinate data from each trajectory. Next, the phosphate groups in the sampled Cy3 molecules were replaced with hydrogen atoms, and density functional theory (DFT) was used to first optimize the hydrogen atom positions followed by a time-dependent DFT calculation[25,26] of the singlet excited states of the Cy3 molecules using the B3LYP functional,[27] the 6-31+G(d) Gaussian basis set,[17] and implicit COSMO water solvation,[28,29] as implemented in the NWChem 6.6 software package.[30]

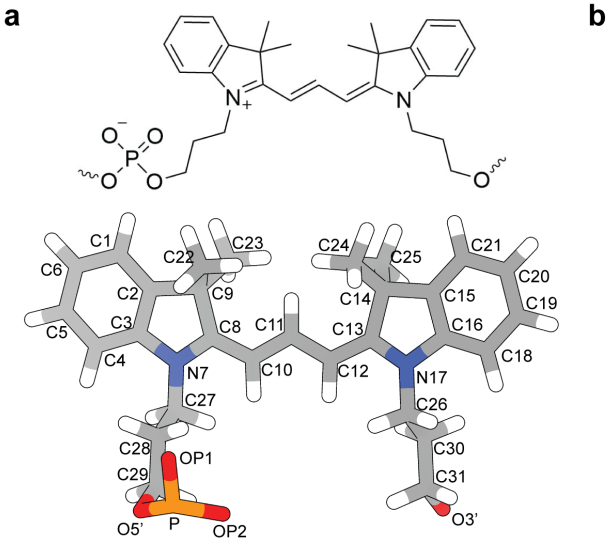


b

| Atom | Type | Charge | Atom | Type | Charge |
|---|---|---|---|---|---|
| C1 | ca | -0.2441 | C23 | c3 | -0.0612 |
| H1 | ha | 0.1912 | 1H23 | hc | 0.0285 |
| C2 | ca | 0.0645 | 2H23 | hc | 0.0285 |
| C3 | ca | 0.0665 | 3H23 | hc | 0.0285 |
| C4 | ca | -0.1960 | C24 | c3 | -0.0612 |
| H4 | ha | 0.1780 | 1H24 | hc | 0.0285 |
| C5 | ca | -0.1424 | 2H24 | hc | 0.0285 |
| H5 | ha | 0.1621 | 3H24 | hc | 0.0285 |
| C6 | ca | -0.1157 | C25 | c3 | -0.0612 |
| H6 | ha | 0.1532 | 1H25 | hc | 0.0285 |
| N7 | na | -0.0316 | 2H25 | hc | 0.0285 |
| C8 | c2 | 0.1097 | 3H25 | hc | 0.0285 |
| C9 | c3 | 0.0743 | C26 | c3 | 0.0351 |
| C10 | ce | -0.3316 | 1H26 | h1 | 0.0440 |
| H10 | ha | 0.1889 | 2H26 | h1 | 0.0440 |
| C11 | ce | -0.0841 | C27 | c3 | 0.0351 |
| H11 | ha | 0.3399 | 1H27 | h1 | 0.0440 |
| C12 | ce | -0.3316 | 2H27 | h1 | 0.0440 |
| H12 | ha | 0.1889 | C28 | c3 | 0.0261 |
| C13 | c2 | 0.1097 | 1H28 | hc | 0.0196 |
| C14 | c3 | 0.0743 | 2H28 | hc | 0.0196 |
| C15 | ca | 0.0645 | C29 | c3 | 0.0711 |
| C16 | ca | 0.0665 | 1H29 | h1 | 0.0698 |
| N17 | na | -0.0316 | 2H29 | h1 | 0.0698 |
| C18 | ca | -0.1960 | C30 | c3 | 0.0261 |
| H18 | ha | 0.1780 | 1H30 | hc | 0.0196 |
| C19 | ca | -0.1424 | 2H30 | hc | 0.0196 |
| H19 | ha | 0.1621 | C31 | c3 | 0.0711 |
| C20 | ca | -0.1157 | 1H31 | h1 | 0.0698 |
| H20 | ha | 0.1532 | 2H31 | h1 | 0.0698 |
| C21 | ca | -0.2441 | O5' | OS | -0.4954 |
| H21 | ha | 0.1912 | O3' | OS | -0.5232 |
| C22 | c3 | -0.0612 | OP1 | O2 | -0.7761 |
| 1H22 | hc | 0.0285 | OP2 | O2 | -0.7761 |
| 2H22 | hc | 0.0285 | P | P | 1.1659 |
| 3H22 | hc | 0.0285 | | | |

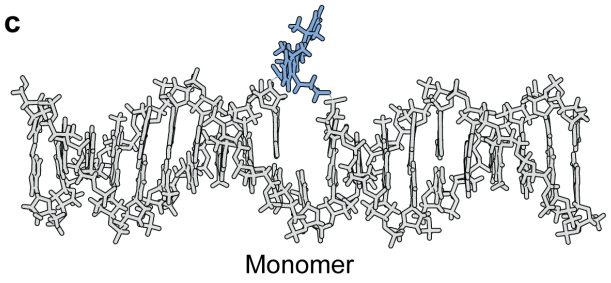


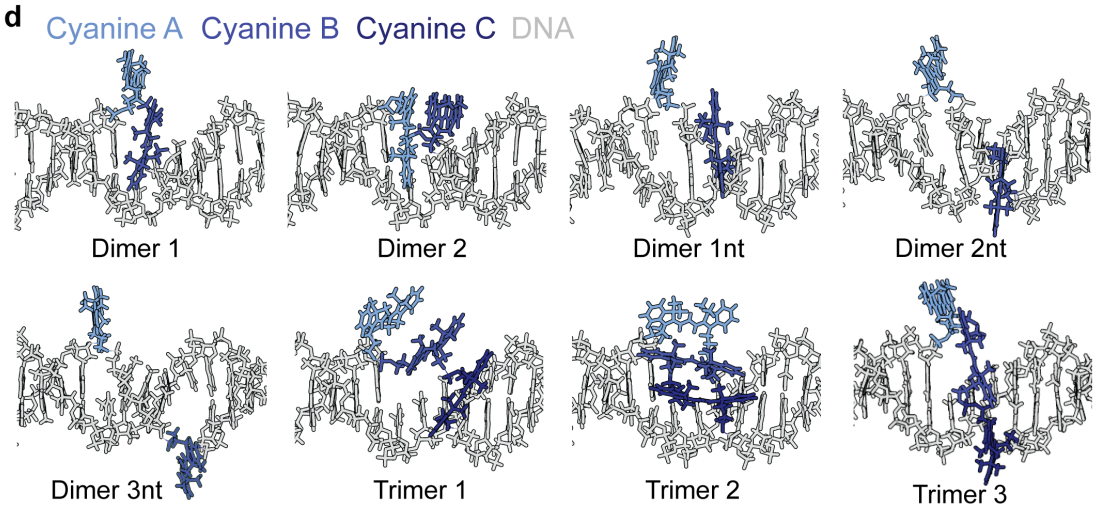


**Figure S53 | Force fields and structures for molecular dynamics simulations.** **(a)** Molecular and atomic coordinates for Cy3 nucleobase substitution, with atom names labeled for heavy atoms. **(b)** Atomic charges and atom types used in the Cy3 modified force field based on Amber GAFF2 and OL15.[2, 3] **(c)** Initial position for the Cy3 monomer coordinates on DNA. **(d)** Initial positions for the Cy3 dimer and trimer coordinates on DNA.

## S6.6 Optical properties of Cy3 monomer.

A least-squares analysis is utilized to determine the electronic-vibrational coupling in monomeric Cy3. The first excited state energy, $\omega_{00}$, for Cy3 is $18150$ cm$^{-1}$, and the energy of vibrational progression, $\omega_{vib}$, is $1150$ cm$^{-1}$, both determined from the experimental absorbance spectra. Additionally, from diagonal analysis of the 2D experimental spectra, we use a FWHM of 740 cm$^{-1}$ of static disorder modeled using a normal distribution, and a HWHM of 213 cm$^{-1}$ of dynamic disorder modeled using a Cauchy distribution. The Franck-Condon overlap integrals for the strength of electronic-vibrational couplings are calculated as [31, 32]

$$|\langle\chi_{e,n}|\chi_{g,0}\rangle|^2 = e^{-S}S^n/n!, \tag{14}$$

where $S$ is the Huang-Rhys parameter[33], $\chi_{e,n}$ are the vibrational wavefunctions of the excited state, and $\chi_{g,0}$ are the vibrational wavefunctions of the ground state. The monomer absorbance spectra, $A_{mon}(\omega)$, is calculated as a sum of individual Cauchy distributions as

$$A_{mon}(\omega) = |\mu_e|^2 \sum_{n=0}^{n_e} |\langle\chi_{e,n}|\chi_{g,0}\rangle|^2 \left(\frac{\gamma^2}{(\omega - \omega_{00} - n\omega_{vib})^2 + \gamma^2}\right), \tag{15}$$

where $n_e$ is the number of excited state vibrational modes, the ground state transitions are assumed to originate from the zeroth-vibrational mode, $\mu_e$ is the transition dipole moment of the excited state, and $\gamma$ is the HWHM for the homogeneous broadening. Inhomogeneous broadening is added into the absorbance spectra by distributing $\omega_{00}$ values centered around a normal distribution, and averaging the spectra results over $100000$ trial functions. The parameters $n_e = 4$ and $S = 0.51$ are chosen from a least squares analysis of the calculated monomeric absorbance spectra compared to the experimental absorbance spectra, shown in Figure S44.

## S6.7 Optical properties of multimeric Cy3.

For multimeric Cy3 trajectories, the transition densities of the $S_0 \rightarrow S_1$ excited state transitions are extracted, and the transition density cube (TDC) method is utilized to accurately calculate the electronic couplings by discretizing the transition densities onto a volumetric grid.[34] This electronic coupling, $V_{DA}$, using the TDC method is calculated as

$$V_{DA} \approx V_{TDC} = \sum_{i,j} \frac{M_D\,(i)\,M_A\,(j)}{4\pi\varepsilon_0 r_{ij}}, \tag{16}$$

where $M_{D,A}$ represents the discretized transition densities calculated from the ground and first excited state wavefunctions of the donor (D) and acceptor (A) chromophore molecules,

$$M_{D,A}\,(x,y,z) = V_\delta \int_z^{z+\delta_z} \int_y^{y+\delta_y} \int_x^{x+\delta_x} |\psi_0\rangle\langle\psi_1| dxdydz, \tag{17}$$

with grid size, $\delta$, and volume element, $V_\delta$. The electronic couplings and transition dipole angles are plotted from MD snapshots of the dimeric and trimeric DNA-scaffolded Cy3 complexes in Figures S45 and S51.

If only the electronic couplings between each Cy3 monomer pair in the DNA-scaffolded systems are included, a site-basis Frenkel Hamiltonian $\hat{H}_{elec}$ can be built for each time-dependent system, which is described as

$$\hat{H}_{elec} = \sum_i^N \nu_i |\psi_i\rangle\langle\psi_i| + \sum_i^N \sum_{j\neq i}^N V_{ij} |\psi_j\rangle\langle\psi_i|, \tag{18}$$

where $\nu_i$ is the site energy of the $S_0 \rightarrow S_1$ electronic transition of the $i^{th}$ Cy3 molecule, $|\psi_i\rangle$ describes the excited state molecular wavefunction for the monomeric site, and $V_{ij}$ is the Coulombic electronic coupling between the $i^{th}$ and $j^{th}$ monomeric sites.[35] An example of the site-basis Frenkel Hamiltonian for three electronic states is shown as

$$\hat{H}_{elec} = \begin{bmatrix} \nu_1 & V_{12} & V_{13} \\ V_{21} & \nu_2 & V_{23} \\ V_{31} & V_{32} & \nu_3 \end{bmatrix}. \tag{19}$$

Additionally, with the inclusion of electronic-vibrational transitions we can build a site-basis Holstein Hamiltonian $\hat{H}_{vib}$, described as

$$\hat{H}_{vib} = \sum_{i}^{N} \nu_i |\psi_i\rangle\langle\psi_i| + \sum_{k=0}^{n_e} k\omega_{vib} + \sum_{i}^{N}\sum_{j\neq i}^{N}\sum_{k,l=0}^{n_e} V_{ij}|\psi_j\rangle\langle\psi_i|\langle\chi_{i,k}|0\rangle\langle\chi_{j,l}|0\rangle, \tag{20}$$

where $\nu_i$ is the site energy of the $S_0 \rightarrow S_1$ electronic transition of the $i^{th}$ Cy3 molecule, $|\psi_i\rangle$ describes the excited state molecular wavefunction for the monomeric site, and $V_{ij}$ is the Coulombic electronic coupling between the $i^{th}$ and $j^{th}$ monomeric sites.[35] An example of the site-basis Holstein Hamiltonian for two electronic states and three vibrational states is shown as

$$\hat{H}_{vib} = \begin{bmatrix} \nu_1 & 0 & 0 & V_{12}\langle 0|0\rangle^2 & V_{12}\langle 0|0\rangle\langle 1|0\rangle & V_{12}\langle 0|0\rangle\langle 2|0\rangle \\ 0 & \nu_1+\omega_{vib} & 0 & V_{12}\langle 1|0\rangle\langle 0|0\rangle & V_{12}\langle 1|0\rangle^2 & V_{12}\langle 1|0\rangle\langle 2|0\rangle \\ 0 & 0 & \nu_1+2\omega_{vib} & V_{12}\langle 2|0\rangle\langle 0|0\rangle & V_{12}\langle 2|0\rangle\langle 1|0\rangle & V_{12}\langle 2|0\rangle^2 \\ V_{21}\langle 0|0\rangle^2 & V_{21}\langle 1|0\rangle\langle 0|0\rangle & V_{21}\langle 2|0\rangle\langle 0|0\rangle & \nu_2 & 0 & 0 \\ V_{21}\langle 0|0\rangle\langle 1|0\rangle & V_{21}\langle 1|0\rangle^2 & V_{21}\langle 2|0\rangle\langle 1|0\rangle & 0 & \nu_2+\omega_{vib} & 0 \\ V_{21}\langle 0|0\rangle\langle 2|0\rangle & V_{21}\langle 1|0\rangle\langle 2|0\rangle & V_{21}\langle 2|0\rangle^2 & 0 & 0 & \nu_2+2\omega_{vib} \end{bmatrix}. \tag{21}$$

The absorbance spectra can be computed by first diagonalizing the site-basis Holstein Hamiltonian to solve the stationary Schrödinger equation in the excitonic basis, $\hat{H}_{vib}|\phi_k\rangle = \varepsilon_k|\phi_k\rangle$, where the excitonic wavefunctions, $|\phi_i\rangle$, are expanded over the set of monomeric wavefunctions, $|\phi_k\rangle = \sum_i U_{ik}|\psi_i\rangle$. From this procedure, the excitonic wavefunction energies, $\varepsilon_i$ and amplitudes, $U_{ik}$, are obtained [36, 35] and can be used to calculate spectral properties of the Cy3 aggregates.

The absorbance stick spectra are calculated using the excitonic site energies and amplitudes from the diagonalized Holstein Hamiltonian, and the transition dipole moments, $\mu$, of the monomeric excited states. The absorbance stick-spectra intensities are calculated using

$$\mu_i^2 = \sum_{j,k=1}^{N} (\vec{\mu}_j \cdot \vec{\mu}_k) U_{ji} U_{ki}, \tag{22}$$

with units of $\mu$ in Debye, $\varepsilon$ in cm$^{-1}$, $\mu^2$ in Debye$^2$, $R$ in nm.[36, 35] Static disorder is included in the spectral calculations by randomizing the diagonal site energies based on a normal distribution. Each individual absorbance spectra includes homogeneous broadening, which is included using a Cauchy distribution as follows

$$A(\omega) = \sum_{i}^{N} \mu_i^2 \left( \frac{\gamma^2}{(\omega - \varepsilon_i) + \gamma^2} \right), \tag{23}$$

and then the calculated individual spectra are averaged from 10000 trial aggregate systems with randomized site energies.

## Supplemental References


[1] Kringle, L., Sawaya, N. P. D., Widom, J., Adams, C., Raymer, M. G., Aspuru-Guzik, A., and Marcus, A. H. (2018). Temperature-dependent conformations of exciton-coupled Cy3 dimers in double-stranded DNA. J. Chem. Phys. *148*, 085101.

[2] Wang, J., Wolf, R. M., Caldwell, J. W., Kollman, P. A., and Case, D. A. (2004). Development and testing of a general Amber force field. J. Comput. Chem. *25*, 1157–1174.

[3] Galindo-Murillo, R., Robertson, J. C., Zgarbová, M., Šponer, J., Otyepka, M., Jurečka, P., and Cheatham, III, T. E. (2016). Assessing the current state of Amber force field modifications for DNA. J. Chem. Theory Comput. *12*, 4114–4127.

[4] Sanda, F., Perlík, V., Lincoln, C. N., and Hauer, J. (2015). Center line slope analysis in two-dimensional electronic spectroscopy. J. Phys. Chem. A *119*, 10893–10909.

[5] Khyasudeen, M. F., Nowakowski, P. J., and Tan, H.-S. (2019). Measuring the ultrafast correlation dynamics between the Qx and Qy bands in chlorophyll molecules. J. Phys. Chem. B *123*, 1359–1364.

[6] Brixner, T., Mančal, T., Stiopkin, I. V., and Fleming, G. R. (2004). Phase-stabilized two-dimensional electronic spectroscopy. J. Chem. Phys. *121*, 4221–4236.

[7] Buckhout-White, S., Spillmann, C. M., Algar, W. R., Khachatrian, A., Melinger, J. S., Goldman, E. R., Ancona, M. G., and Medintz, I. L. (2014). Assembling programmable FRET-based photonic networks using designer DNA scaffolds. Nat. Comm. *5*, 5615.

[8] Weinreis, S. A., Ellis, J. P., and Cavagnero, S. (2010). Dynamic fluorescence depolarization: a powerful tool to explore protein folding on the ribosome. Methods *52*, 57–73.

[9] Watkins, L. P. and Yang, H. (2005). Detection of intensity change points in time-resolved single-molecule measurements. J. Phys. Chem. B *109*, 617–628.

[10] Maus, M., Cotlet, M., Hofkens, J., Gensch, T., De Schryver, F. C., Schaffer, J., and Seidel, C. (2001). An experimental comparison of the maximum likelihood estimation and nonlinear least-squares fluorescence lifetime analysis of single molecules. Anal. Chem. *73*, 2078–2086.

[11] Santra, K., Zhan, J., Song, X., Smith, E. A., Vaswani, N., and Petrich, J. W. (2016). What is the best method to fit time-resolved data? A comparison of the residual minimization and the maximum likelihood techniques as applied to experimental time-correlated, single-photon counting data. J. Phys. Chem. B *120*, 2484–2490.

[12] Roe, D. R. and Cheatham, III, T. E. (2013). PTRAJ and CPPTRAJ: Software for processing and analysis of molecular dynamics trajectory data. J. Chem. Theory Comput. *9*, 3084–3095.

[13] Case, D., Cerutti, D., Cheatham, III, T., Darden, T., Duke, R., Giese, T., Gohlke, H., Goetz, A., Greene, D., Homeyer, N., and et al., AMBER 2017. University of California, San Francisco.

[14] Zheng, H., Caram, J. R., Dahlberg, P. D., Rolczynski, B. S., Viswanathan, S., Dolzhnikov, D. S., Khadivi, A., Talapin, D. V., and Engel, G. S. (2014). Dispersion-free continuum two-dimensional electronic spectrometer. Appl. Optics *53*, 1909–1917.

[15] Son, M., Mosquera-Vázquez, S., and Schlau-Cohen, G. S. (2017). Ultrabroadband 2D electronic spectroscopy with high-speed, shot-to-shot detection. Opt. Express *25*, 18950–18962.

[16] Schmidt, M. W., Baldridge, K. K., Boatz, J. A., Elbert, S. T., Gordon, M. S., Jensen, J. H., Koseki, S., Matsunaga, N., Nguyen, K. A., Su, S., Windus, T. L., Dupuis, M., and Montgomery, Jr., J. A. (1993). General atomic and molecular electronic structure system. J. Comput. Chem. *14*, 1347–1363.

[17] Hehre, W. J., Ditchfield, R., and Pople, J. A. (1972). Self-consistent molecular orbital methods. XII. further extensions of gaussian-type basis sets for use in molecular orbital studies of organic molecules. J. Chem. Phys. *56*, 2257–2261.

[18] Bayly, C. I., Piotr, C., Cornell, W. D., and Kollman, P. A. (1993). A well-behaved electrostatic potential based method using charge restraints for deriving atomic charges: The RESP model. J. Phys. Chem. *97*, 10269–10280.

[19] Vanquelef, E., Simon, S., Marquant, G., Garcia, E., Klimerak, G., Delepine, J. C., Cieplak, P., and Dupradeau, F.-Y. (2011). R.E.D. Server: a web service for deriving RESP and ESP charges and building force field libraries for new molecules and molecular fragments. Nucleic Acids Res. *39*, W511–W517.

[20] Arnott, S., Campbell Smith, P. J., and Chandraseharan, R. (1976) Atomic coordinates and molecular conformations for DNA–DNA, RNA–RNA, and DNA–RNA helices. In Handbook of Biochemistry and Molecular Biology, 3rd Edition, G. Fasman, ed. (CRC Press) pp. 411–422.

[21] Jorgensen, W., Chandrasekhar, J., Madura, J., Impey, R., and Klein, M. (1983). Comparison of simple potential functions for simulating liquid water. J. Chem. Phys. *79*, 926–935.

[22] Berendsen, H., Postma, J., van Gunsteren, W., DiNola, A., and Haak, J. (1984). Molecular dynamics with coupling to an external bath. J. Chem. Phys. *81*, 3684–3890.

[23] Izaguirre, J. A., Catarello, D. P., Wozniak, J. M., and Skeel, R. D. (2000). Langevin stabilization of molecular dynamics. J. Chem. Phys. *114*, 2090–2098.

[24] Ryckaert, J.-P., Ciccotti, G., and Berendsen, H. J. C. (1977). Numerical integration of the Cartesian equations of motion of a system with constraints: Molecular dynamics of n-alkanes. J. Comput. Phys. *23*, 327–341.

[25] Kohn, W. and Sham, L. J. (1965). Self-consistent equations including exchange and correlation effects. Phys. Rev. *140*, A1133–A1138.

[26] Runge, E. and Gross, E. K. U. (1984). Density-functional theory for time-dependent systems. Phys. Rev. Lett. *52*, 997–1000.

[27] Becke, A. D. (1992). Density-functional thermochemistry. III. the role of exact exchange. J. Chem. Phys. *98*, 5648–5652.

[28] Klamt, A. and Schüürmann, G. (1993). COSMO: A new approach to dielectric screening in solvents with explicit expressions for the screening energy and its gradient. J. Chem. Soc. Perk. T. 2 799–805.

[29] York, D. M. and Karplus, M. (1999). A smooth solvation potential based on the conductor-like screening model. J. Phys. Chem. A *103*, 11060–11079.

[30] Valiev, M., Bylaska, E. J., Govind, N., Kowalski, K., Straatsma, T. P., Van Dam, H. J. J., Wang, D., Nieplocha, J., Apra, E., Windus, T. L., and de Jong, W. A. (2010). NWChem: A comprehensive and scalable open-source solution for large scale molecular simulations. Comput. Phys. Commun. *181*, 1477–1489.

[31] de Jong, M., Seijo, L., Meijerink, A., and Robouw, F. T. (2015). Resolving the ambiguity in the relation between stokes shift and Huang-Rhys parameter. Phys. Chem. Chem. Phys. *17*, 16959–16969.

[32] Keil, T. H. (1965). Shapes of impurity absorption bands in solids. Phys. Rev. *140*, A601–A616.

[33] Huang, K. and Rhys, A. (1950). Theory of light absorption and non-radiative transitions in F-centres. P. R. Soc. Lond. A *204*, 406–423.

[34] Krueger, B. P., Scholes, G. D., and Fleming, G. R. (1998). Calculation of couplings and energy-transfer pathways between the pigments of lh2 by the ab initio transition density cube method. J. Phys. Chem. B *102*, 5378–5386.

[35] Prokhorenko, V. I., Steensgaard, D. B., and Holzwarth, A. R. (2003). Exciton theory for supramolecular chlorosomal aggregates: 1. aggregate size dependence of the linear spectra. Biophys. J. *85*, 3173–3186.

[36] Pearlstein, R. M. (1991). Theoretical interpretation of antenna spectra. In Chlorophylls, H. Scheer, ed. (CRC Press) pp. 1047–1078.